# Rare-earth iron garnet thin films: structural and magnetic properties

**Dissertation**

zur Erlangung des akademischen Grades

Dr. rer. nat.

eingereicht an der
Mathematisch-Naturwissenschaftlich-Technischen Fakultät
der Universität Augsburg

von

**Oana-Tereza Ciubotariu**

Augsburg, February 2020

Universität
Augsburg
University

Erstgutachter: Prof. Dr. Manfred Albrecht
Zweitgutachter: Prof. Dr. Hubert J. Krenner
Tag der mündlichen Prüfung: 18.09.2020

# Bibliographic record

Ciubotariu, Oana-Tereza:

*Rare-earth iron garnet thin films: structural and magnetic properties*

Dissertation

Universität Augsburg, Mathematisch-Naturwissenschaftlich-Technische Fakultät (2020)

# Abstract

The present thesis focuses on the characterization of yttrium and thulium iron garnet thin films grown by pulsed laser deposition. The impact of various growth parameters (substrate type, film thickness, post-deposition annealing of amorphous or crystalline structures) on the morphologic, structural and magnetic properties is investigated.

In the first part, the optimization steps carried out for the film growth are described. Chemical analysis reveals a strong dependence of the rare-earth/Fe ratio on the background oxygen pressure. Stoichiometric films are grown at low oxygen pressure, and increasing the chamber pressure during deposition results in rare-earth rich films. On the example of $Tm_3Fe_5O_{12}$ films prepared on $Gd_3Sc_2Ga_3O_{12}$ substrates, it is shown that smooth epitaxial films can be achieved at moderate substrate temperatures (< 700 °C) and deposition rates below 0.04 nm/s. The cooling rate after deposition at elevated temperatures is observed to mainly influence the coercive field.

The following part focuses on the properties of $Y_3Fe_5O_{12}$ (short YIG) thin films. Films grown on lattice-matching $Gd_3Ga_5O_{12}$ substrates have an in-plane magnetic easy axis due to the dominant magnetic shape anisotropy. Substrate features such as terraces or sinusoidal structures are visible on the film surface for thicknesses up to 100 nm. Heat treatments on room temperature-deposited YIG films carried out in ambient atmosphere were observed to lead to epitaxial films. Magnetic characterization indicates the film crystallization after annealing at 600 °C for 30 minutes. Additionally, films annealed at temperatures in the 600 °C – 725 °C range possess similar properties as films grown at elevated temperatures: the garnet crystal structure, smooth surfaces characterized by roughness values of 0.1 nm, and coercive fields below 1 Oe.

In the third part, $Tm_3Fe_5O_{12}$ (TmIG) films are strained-grown on two substrate types: substituted-$Gd_3Ga_5O_{12}$ (sGGG) and $Gd_3Sc_2Ga_3O_{12}$ (GSGG). The effect of film thickness on the structural and magnetic properties is investigated. Structural characterization reveals that the thin films are grown under out-of-plane compressive strain and increasing the film thickness results in the relaxation of the unit cell. The induced-magnetoelastic anisotropy is dominant below a critical film thickness and the films have an out-of-plane magnetic easy axis. The loss in strain with increasing film thickness results in the rotation of the easy axis of magnetization towards the film plane. The bulk TmIG – substrate lattice mismatch influences the relaxation thickness: TmIG(70 nm)/sGGG shows perpendicular magnetic anisotropy, while an in-plane magnetic easy axis is reported for TmIG(37 nm)/GSGG. Additionally, the Gilbert damping

parameter of TmIG(20 – 300 nm)/sGGG is found to be around 0.02. Furthermore, the effect of post-deposition annealing of strained TmIG films is investigated. A heat treatment in ambient atmosphere at 600 °C for 30 minutes has a minor effect on the morphological, structural and magnetic properties of a 14 nm thick TmIG film. The crystallization of amorphous TmIG films via heat treatment carried out in ambient atmosphere is initiated around 670 °C. However, 15 – 20 nm thick films show cracks and isotropic magnetic properties after annealing at this temperature.

The topic of the last part is the growth of YIG films on strained TmIG layers. For this, 5 – 20 nm thick YIG films were deposited at room temperature on 15 nm thick TmIG films, followed by a heat treatment at 600 °C for 30 minutes. Structural characterization carried out before and after the heat treatment confirms the crystallization of the YIG film at 600 °C. After annealing, no thulium is observed in the chemical analysis of the film surface indicating no or very weak intermixing between the YIG and TmIG films. Furthermore, magnetic characterization reveals that 5 – 20 nm YIG films grown on strained TmIG films possess an out-of-plane easy axis of magnetization.

## Table of Contents

# Introduction

The discovery of giant magnetoresistance (GMR) [1,2] and tunneling magnetoresistance (TMR) [3] together with the scientific progress regarding the magnitude of these effects represented key factors for the development of a new technological branch, in which the information is represented by the state of the electron spin. By analogy with electronics, the consideration of the electron spin, and its associated magnetic moment, as an additional degree of freedom to the electron charge gave rise to the field of spintronics. The interest in implementing spintronic effects in several technological areas (memory devices, sensors, read/write heads) experienced a fast increase in the last years. Driven by a continuous wish of further bit size miniaturization, higher memory density, and lower power consumption of memory devices, as well as reduction of read/write times, magnetic multilayered structures, like spin valves and magnetic tunnel junctions, were soon developed [4,5]. In a simplified picture, these devices feature a pinned and a free magnetic layer separated by a non-magnetic conductive or an insulating spacer. Modifying the magnetic coupling of the two layers between parallel and antiparallel by acting on the free ferromagnet changes the device resistance. The information, encoded in the magnetic state of the free ferromagnet, is read via the GMR or TMR effects. While studies on spin valves reported a steady increase of the GMR signal, much higher TMR effects were observed at room temperature in magnetic tunnel junctions [6]. As a result, the implementation of magnetic tunnel junctions in magnetoresistive random-access memory or racetrack memory became feasible. Technologically relevant magnetic materials must possess an anisotropy energy sufficiently strong to maintain the magnetization direction against thermal fluctuations and stray fields, while requiring a moderate switching (writing) energy. In early stages, free layers made of magnetic materials with an in-plane easy axis of magnetization (for example $Co_{40}Fe_{40}B_{20}$) were preferred due to the easier fabrication process. However, storage lifetimes of around 10 years limit the bit size to a few tens of nm for materials with an in-plane magnetic easy axis. The solution for further bit size reduction was offered by materials with a perpendicular magnetic anisotropy [7].

The easiest method to reverse a magnetic state is via magnetic fields. The reduction of the bit size requires higher bit stability, which in turn, leads to stronger switching fields with a small lateral size distribution. Thermal-assisted switching brings the free layer close to its Curie temperature allowing for lower writing fields [8]. Another method to reverse the magnetic state of a ferromagnet is by using spin currents. The switching of the antiparallel coupling to the parallel state between the pinned and the free layer is achieved by passing an electric current through the pinned layer. Electrons with the spin parallel to the pinned layer magnetization scatter less compared to electrons with an antiparallel spin configuration resulting in a spin-polarized current. The spin-polarized current reaching the free layer exerts a torque on its magnetization. Depending on the torque strength, the direction of the magnetic moments can be reversed [9,10]. The switching to the antiparallel coupling is achieved by reversing the direction of the electric current. The electrons of a non-polarized current travelling through the free layer and reaching the pinned layer are selectively reflected at the spacer – pinned layer interface. Electrons with spin antiparallel to the pinned layer magnetization are preferentially reflected forming a spin-polarized current that flows back towards the free layer. Similar to the previous case, the spin-transfer torque exerted on the free layer magnetization reverses the magnetic state. Writing the information via spin-polarized currents allows bit size reduction and simplifies the device geometry [7].

Magnetic skyrmions or spin currents are a few spintronic alternatives to replace data transfer by the flow control of electric currents. In both cases, data transmission over long distances (tens of μm, ref. [11,12]) with high velocities are already reported in literature. A clear advantage of spin waves (a particular category of spin currents) over any electronic technology is that the information is transferred without electron motion which reduces heat dissipation. The growing interest of the scientific community for spin waves resulted in the development of a new technological branch called magnon spintronics or magnonics. Spin wave implementation in logic circuits is currently also considered [13]. As a prospect for integration in data processing, spin wave propagation in straight waveguides [14], waveguides with variable width [15] or around corners [16] is investigated. In addition to the technological progress regarding generation and detection efficiency, a large contribution is brought from the material sciences. A key feature of materials suitable for magnonic applications is the Gilbert damping, the parameter that reflects the lifetime of a spin wave. While several materials show low Gilbert damping parameters ($Ni_{81}Fe_{19}$, $Co_{40}Fe_{40}B_{20}$), yttrium iron garnet stands out with values in the range $10^{-5} – 10^{-4}$ leading to spin wave decay lengths up to 1.2 mm, ref. [17].

As a first step towards spin wave-based devices, this work focused on the growth of two iron garnets: yttrium iron garnet ($Y_3Fe_5O_{12}$, YIG) and thulium iron garnet ($Tm_3Fe_5O_{12}$, TmIG) thin films. These two materials were selected as representatives for the two categories of magnetic easy axis directions. YIG films deposited on lattice-matching substrates (for example $Gd_3Ga_5O_{12}$) show two magnetic anisotropy contributions: a weak magnetocrystalline anisotropy with easy axes along the crystal <111> directions [18], and the dominant magnetic shape anisotropy that orients the magnetization in the film plane. An additional magnetoelastic anisotropy contribution is induced in tensile- or compressive-strained films which can lead to an out-of-plane easy axis of magnetization. The competition between various types of magnetic anisotropy was studied in TmIG films, since TmIG has a relatively large magnetostriction parameter [18], a key component for achieving a large magnetoelastic anisotropy.

The present work can be divided into two main sections: an introductory part followed by the presentation and discussion of the experimental results. The first chapter starts with the description of the rare-earth iron garnets family. It continues with an overview of the research carried out on YIG and TmIG films. Spin waves and the types of magnetic anisotropy are also introduced here. In the second chapter, the growth technique of the thin films, and the investigation methods are described. Nanometer thick films were prepared by pulsed laser deposition. The film properties (morphology, stoichiometry, crystalline structure, magnetic state, etc.) were evaluated by techniques such as atomic force microscopy, energy dispersive X-ray fluorescence, X-ray diffraction, polar magneto-optical Kerr effect, etc.

The presentation and discussion of the experimental results start with the next chapter. The growth of thin films by pulsed laser deposition requires the optimization of various growth parameters. On the example of TmIG films, the third chapter illustrates the steps followed for the identification of the optimal oxygen pressure, deposition rate, substrate temperature and cooling rate at which stoichiometric films with the desired crystal structure and low surface roughness are obtained.

The following two chapters focus on the properties of individual YIG and TmIG films, respectively. In the fourth chapter, the flexibility of growing YIG films on GGG(111) substrates was investigated. Films up to 100 nm were prepared on heat-treated and patterned substrates. Additionally, heat treatments on amorphous YIG films grown at room temperature were carried out in ambient atmosphere in a broad temperature range.

The investigations on TmIG films represent the topic of the next chapter. The evolution of in-plane tensile strain and the induced-magnetoelastic anisotropy with film thickness was evaluated for films prepared on substrates with different levels of lattice mismatch. Heat treatments in ambient atmosphere on amorphous and crystalline films were carried out as a prospect of integrating TmIG films in garnet heterostructures.

In the end, all the investigations carried out above allowed the preparation of YIG/TmIG(15 nm)/GSGG structures. The garnet bilayers were investigated for various YIG film thicknesses with the results presented in the sixth chapter.

The thesis ends with a summary of the results obtained on YIG and TmIG films and with a discussion on future research directions.

# 1 Basics

The focus materials of this work are yttrium iron garnet and thulium iron garnet. The chapter starts with a description of the structural and magnetic properties of the rare-earth iron garnet family. In the following, an overview of the research carried out on the two materials is presented. Spin waves and types of magnetic anisotropy, relevant for the investigated films, are also introduced here.

## 1.1 Structural and magnetic description of rare-earth iron garnets

Rare-earth iron garnets are materials with the chemical formula $R_3Fe_2Fe_3O_{12}$ (short RIG), where $R$ is a rare-earth element. It is generally considered that garnets crystallize in cubic structures belonging to the space group *Ia*-3*d*. However, the <111> directions of yttrium or samarium iron garnet crystals are the easy axes of magnetization [18]. Thus, these garnets cannot have a cubic structure. In reality, both crystals are rhombohedral. Nevertheless, the deviation from the cubic structure is hardly observed in crystallographic studies and the *Ia*-3*d* space group is commonly used for structural refinement or calculations.

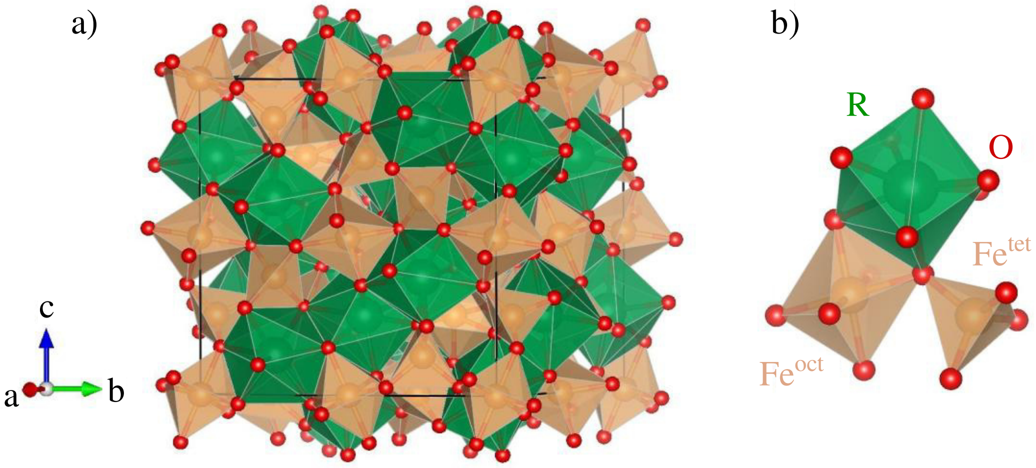

*Figure 1.* *a)* Cubic unit cell of $R_3Fe_5O_{12}$ designed using the VESTA software [19]. *b)* Illustration of $R$, $Fe^{oct}$ and $Fe^{tet}$ ions in the center of the polyhedra formed with the nearest oxygen ions.

Large unit cells accommodate eight formula units with a total of 160 ions. *Figure 1 (a)* illustrates the RIG cubic unit cell designed with the VESTA software [19]. Oxygen ions located at the 96*h* sites (Wyckoff position [20]) surround each cation. The cations experience three different environments (*Figure 1 (b)*). The rare-earth ion, occupying the 24*c* site, is at the center of the dodecahedron formed with the neighboring O ions. The two Fe ions are located on two different lattice sites: one ion occupies the 16*a* site and its coordination number to oxygen is six (octahedron, notation $Fe^{oct}$), while the other ion occupies the 24*d* site at the center of a tetrahedron (notation $Fe^{tet}$). The ratio $Fe^{oct}/Fe^{tet}$ is 2/3.

Crystallographic studies on $R_{3\text{-x}}R'_x\text{Fe}_5\text{O}_{12}$ pellets ($R \equiv$ Y, Gd, Sm, Lu; $R' \equiv$ La, Pr, Nd) reveal a maximum lattice constant of 12.540 Å for the garnet structure [21,22]. For each system, maximum $x$ values ($x_{\text{max}}$) were identified above which traces of perovskite phase are present, for example $x_{\text{max}} = 0.40$ for $\text{Y}_{3\text{-x}}\text{La}_x\text{Fe}_5\text{O}_{12}$. Due to large ionic radii, lanthanide ions from $\text{La}^{3+}$ to $\text{Nd}^{3+}$ can only partially substitute the rare-earth ion at the *c* site.

$\text{Fe}^{3+}$ contributes to the RIG magnetization through the spin of the 3*d* electrons while the orbital angular momentum is zero. Thus, at 0 K, each $\text{Fe}^{3+}$ ion has a magnetic moment of 5 $\mu_B$. Neighboring $\text{Fe}^{3+}$ ions, occupying the octahedral and tetrahedral sites, couple antiparallel via an oxygen ion. Since the $\text{Fe}^{\text{oct}}/\text{Fe}^{\text{tet}}$ ratio is 2/3, the iron contribution to the total magnetization is 5 $\mu_B$/formula unit at 0 K. $\text{Y}^{3+}$ and $\text{Sc}^{3+}$, the two rare-earth ions outside of the lanthanide series, have completely filled orbitals. They possess no magnetic moment since, in both cases, the total spin and orbital quantum numbers are zero.

Among the lanthanide family, the rare-earth ion contributes to the magnetization through the 4*f* electrons. 14 electrons occupy the 4*f* shell of $\text{Lu}^{3+}$ and, similar to $\text{Y}^{3+}$ and $\text{Sc}^{3+}$, $\text{Lu}^{3+}$ possesses no magnetic moment. LuIG, YIG and ScIG show ferrimagnetic order with a total magnetization given by the Fe ions.

The total spin quantum number $S$ of $R$ ions increases with the occupation degree of the 4*f* shell reaching the maximum value for the half-filled case of $\text{Gd}^{3+}$ and further decreases for heavier lanthanides. The total orbital quantum number $L$ varies through the lanthanide series according to the occupation of the 4*f* shell. For lanthanide ions with less than half-filled 4*f* shell (also referred to as light ions), the projection of the spin magnetic moment $\boldsymbol{m}_S$ on the total magnetic moment $\boldsymbol{m}_J$ is antiparallel since $J = |L - S|$. For heavy ions, the projection is parallel considering that $J = L + S$. Furthermore, the spin of $\text{Fe}^{\text{tet}}$ aligns antiparallel with the lanthanide spin through antiferromagnetic spin-spin interactions [23]. Thus, the total magnetic moment $\boldsymbol{m}_J$ of light lanthanide ions couples parallel with the magnetic spin moment of $\text{Fe}^{\text{tet}}$ $\boldsymbol{m}_{\text{Fe-tet}}$, while $\boldsymbol{m}_J$ of heavy lanthanide ions aligns parallel with the magnetic moment of $\text{Fe}^{\text{oct}}$ (*Figure 2*).

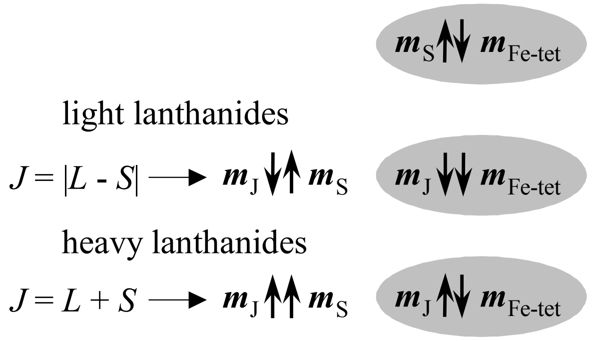

*Figure 2.* Illustration of the coupling between magnetic moment $\boldsymbol{m}_J$ of light and heavy lanthanides with the spin magnetic moment of $\text{Fe}^{\text{tet}}$ $\boldsymbol{m}_{\text{Fe-tet}}$.

Rare-earth iron garnets are ferrimagnets due to the antiparallel coupling of the Fe ions. The Curie temperature is around 565 K for all RIG crystals suggesting a small contribution of the rare-earth ion to the magnetic interaction strength [24]. Light lanthanide iron garnets show no compensation temperature since the rare-earth ion couples parallel to the overall Fe moment. On the contrary, different temperature behaviors of heavy lanthanide and Fe ions lead to a compensation temperature in these systems.

Magnetic data for rare-earth iron garnets reveals lower magnetic moments than the theoretical values that take into account both $L$ and $S$ quantum numbers. Only for lanthanide ions with $L = 0$ ($Gd^{3+}$ and $Lu^{3+}$), the calculated and measured values match. However, neglecting the orbital magnetic moment and considering only the spin magnetic moment does not reflect the measured values for the rest of the rare-earth iron garnets. Neutron diffraction analysis at low temperatures reveals a canting of the rare-earth ion relative to the [111] direction for Tb, Dy, Er, Yb. The presence of a partially quenched or canted angular momentum could explain the reduced magnetic moments of the lanthanide iron garnets [23].

## 1.2 Yttrium iron garnet

Single crystal YIG spheres (lattice constant $a = 12.376$ Å) of high purity and small surface roughness show the lowest ferromagnetic resonance linewidth of < 1 Oe at room temperature [25]. This discovery together with a low magnetization (of 140 emu/cm$^3$ at room temperature) promoted yttrium iron garnets for usage in improvement and development of microwave ferromagnetic devices [26]. The growth of single crystal YIG films by liquid phase epitaxy (LPE) renewed the interest in the material. Micrometer thick films, with bulk-like dynamic properties [27], found soon application in the magnetostatic wave technology [28,29]. The integration of YIG films in modern technology (for example, in high density magnetic storage) requires patterning which is achieved with standard fabrication techniques in the nm thickness range. The poor control of film thickness offered by LPE found solution in other growth techniques. Pulsed laser deposition (PLD) and sputtering became soon the standard deposition techniques of nm thick YIG films.

YIG films grown by PLD exhibit high crystal quality and bulk-like properties when grown on lattice-matching $Gd_3Ga_5O_{12}$ (short GGG, $a = 12.383$ Å) substrates. Reflection high-energy electron diffraction (RHEED) measurements carried out during growth or post-deposition transmission electron microscopy (TEM) images reveal a layer-by-layer growth, sharp substrate/film interface and perfect continuation of the substrate structure up to thicknesses of 100 nm, ref. [30]. Static and dynamic magnetic investigations show bulk-like magnetization, low Gilbert damping parameter of $2 \cdot 10^{-4}$ and narrow ferromagnetic resonance linewidth [31]. The magnetic properties that promote YIG for technological applications are strongly related to its crystal structure. While YIG films show bulk-like properties when grown on GGG substrates, a decreased film quality (resulting in a larger Gilbert damping) is observed for layers deposited on substrates used in nowadays technology. An increase of the Gilbert damping parameter by one order of magnitude was reported for YIG films on Si substrates [32].

The crystallization of garnet films is achieved at elevated temperatures, thus, YIG films are commonly grown at around 650 °C, ref. [33,34]. At a constant deposition rate, the substrate temperature during growth influences strongly the film surface, an important factor for the integration of films in multilayer heterostructures. Optimization steps of the growth conditions leading to high quality films are time consuming. Room temperature depositions followed by a heat treatment allows for a larger range of possible laser pulse energies and rates. Recently, Hauser et al. reported on the annealing of amorphous YIG layers [35]. The films underwent a heat treatment in an oxygen atmosphere after deposition at room temperature. 56 nm thick films were observed to attain the garnet crystal structure and show an ultra low Gilbert damping parameter of $6 \cdot 10^{-5}$.

The extremely low Gilbert damping parameter and the isolating nature make YIG the prototype material for spin transport investigations. The vast majority of research on YIG films is conducted around understanding of physical phenomena. Numerous works focus on the spin-wave (SW) excitation and detection techniques as well as associations of materials with the highest efficiency. The excitation of SWs in YIG films is achieved by microwaves [11,36], thermal (longitudinal spin Seebeck effect [37]), or via spintronic (spin-transfer torque [38]) effects. Static properties are commonly probed by measuring the electric current generated in an adjacent non-magnetic layer via inverse spin Hall effect. For the investigation of spin dynamics, time-resolved scanning transmission X-ray microscopy [39] or Brillouin light scattering spectroscopy [40] are used.

In thin film form, YIG films show an in-plane magnetic easy axis due to the dominant shape anisotropy. Tailoring the magnetic easy axis direction would open applications in new areas of spintronics, for example in spin-orbit torque-assisted switching already investigated in other magnetic insulators with perpendicular magnetic anisotropy (PMA) [41] or motivated by the recent observation of room temperature skyrmions in magnetic insulators with PMA [42].

Since for garnets the [111] direction is the crystallographic easy axis of magnetization, (111)-oriented substrates are commonly chosen. However, the shape anisotropy overcomes the weak magnetocrystalline anisotropy and the magnetic easy axis of YIG films grown on GGG substrates is oriented within the sample plane.

One method for achieving PMA is by induced-strain giving rise to magnetoelastic anisotropy. Iron garnets with a negative (positive) magnetostriction constant $\lambda_{111}$ can have an out-of-plane (oop) easy axis of magnetization when grown under in-plane tensile (compressive) strain. Several approaches have been proposed to achieve for YIG layers an oop easy axis of magnetization, including the variation of oxygen pressure during growth and substrate type [43]. However, in these studies no PMA could be observed for YIG films grown on GGG(111) and substituted-GGG (short sGGG, $a$ = 12.505 Å) (111) substrates. In contrast, Krockenberger et al. observed weak PMA for 100 nm thick YIG films grown on GGG(111) substrates [33]. X-ray diffraction studies revealed a slight elongation of the unit cell along the surface normal. Additionally, Popova et al. reported for 10 nm thick polycrystalline YIG films deposited on quartz substrates by PLD the presence of weak PMA with low remanent magnetization [44,45]. Recently, tensile strain-induced magnetoelastic anisotropy was observed for YIG films grown on $(Gd_{0.63}Y_{2.37})(Sc_2Ga_3)O_{12}$ ($\Delta = 100(a_{\text{sub}} - a_{\text{film}})/a_{\text{sub}} = 1.04$ %) and $Gd_3Sc_2Ga_3O_{12}$ ($\Delta$ = 1.56 %) substrates leading to an oop magnetic easy axis for film thicknesses below 15 nm, ref. [46]. Stress-engineered 20 – 40 nm thick YIG films sandwiched between a buffer and a cover layer revealed a suppressed in-plane strain relaxation, thus, allowing the presence of PMA in the order of 120 kerg/cm$^3$, ref. [47]. Furthermore, adding third elements can induce sufficient in-plane tensile strain to the unit cell resulting in strain-induced PMA as demonstrated for Bi-doped YIG films on sGGG(111) with little impact on the Gilbert damping parameter ($\alpha = 3 \cdot 10^{-4}$) [48].

## 1.3 Thulium iron garnet

In the attempt of improving PMA for larger film thicknesses, the attention turned to other rare-earth-based iron garnets while trying to maintain a low Gilbert damping parameter [49–51]. A promising iron garnet is $Tm_3Fe_5O_{12}$ (short TmIG, $a$ = 12.323 Å). Possible substrate choices for the growth of TmIG films under tensile strain are GGG ($\Delta$ = 0.49 %) and sGGG ($\Delta$ = 1.45 %) substrates. Tang et al. observed for 10 nm thick TmIG films an oop easy axis of magnetization when grown on sGGG(111) substrates while 10 nm thick TmIG layers on GGG(111) substrates showed an ip easy axis of magnetization, suggesting an insufficient tensile strain for the latter case [52]. A similar result was recently found for extremely thin layers (< 2 nm) [53]. However, TmIG films were observed to maintain a constant tensile strain level up to thicknesses of 350 nm, ref. [49]. Films thinner than 30 nm were reported to have similar magnetic properties with a magnetoelastic anisotropy of 175 kerg/cm$^3$, ref. [54,55]. In a recent study, off-axis sputter-deposited TmIG films on GGG(111) in the thickness range of 10 – 30 nm showed PMA and low Gilbert damping of $\alpha = 0.0133$, still being two orders of magnitude higher than for YIG films [56]. Based on these reports, subtle differences regarding growth and strain conditions obviously influence the overall magnetic properties of TmIG films.

## 1.4 Spin waves

Spin currents represent the flow of spin angular momentum. In non-magnetic conductors, the propagation of spin angular momentum takes place via conduction electrons as illustrated in *Figure 3 (a)*. In magnetically ordered materials, collective excitations of the electron spin system, known as a spin wave (SW) [57], carry spin angular momentum without electrical conduction (*Figure 3 (b)*).

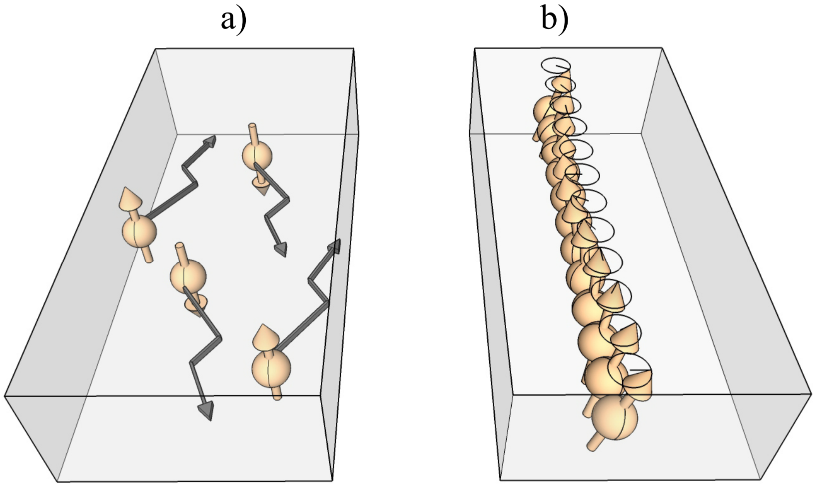

*Figure 3.* Flow of spin angular momentum in *a)* a non-magnetic and *b)* a magnetic material.

External forces (mainly magnetic fields) drive the local precession of the spin system around the equilibrium direction. Exchange and/or dipolar interactions lead to the propagation of the precession through the material as SWs. Dispersion spectra show that SWs exist in a broad wavenumber (wavelengths from micrometers down to nanometers) and frequency range (from GHz up to THz). At large wavenumbers $k$ (or small wavelengths $\lambda$), the exchange term in the dispersion relation becomes dominant and the excitations are referred to as exchange SWs. Waves with low $k$, for which the dipolar fields couple the magnetic moments, are known as magnetostatic or dipolar SWs [58].

SW excitation in thin films or waveguides (1D stripe of a magnetic film) is commonly realized by spin-transfer torque [59], using femtosecond laser pulses [60], via coplanar waveguides or planar stripe antennae [61,62], while for the detection, similar stripe antennae, Brillouin light scattering spectroscopy [63] or magneto-optical Kerr effect [64] are often utilized. The characteristics of SWs (its dispersion relation) generated in waveguides by applied magnetic fields $H_{\text{ext}}$ are given by material properties (saturation magnetization and exchange constant), $H_{\text{ext}}$ as well as the geometry of the waveguide (thickness and width) [65].

In the last years, the idea of using SWs in information transport and processing has emerged and grown significantly. The transfer of information without electrical conduction would lead to lower heat losses. The reported progress regarding modulation and guidance [62,66] of SWs makes wave-based computation a feasible future prospect. However, additional SW properties influence the viability of spin wave devices.

Broad dispersion spectra indicate that SWs in a large range of wavelengths $\lambda$ and frequencies $\omega$ can be excited. All SW properties relevant for computing applications are defined by $\lambda$ (or $k$) and $\omega$. Dipolar SWs (with long $\lambda$) are commonly in the GHz regime, while exchange SWs (short $\lambda$) can extend in the THz frequency range. Computation exploiting the SW phase [67] requires device sizes larger than $\lambda$. However, with $\lambda$ limited by the material lattice constants [65], devices smaller than 10 nm are feasible. Additionally, in the exchange interaction region of the dispersion spectrum, $\omega$ increases with $k^2$. With the clock rate of computing devices limited by the SW frequency, large $\omega$ are of interest for data processing [65]. The SW group velocity $v_g = \partial\omega/\partial k$, influencing the data transport, scales with $k$ in this part of the dispersion spectrum while it is rather small for dipolar and dipolar-exchange SWs. These characteristics point to the benefits of using exchange SWs. The drawback of exchange SWs comes from the fact that the SW relaxation time $\tau$ is inversely proportional to $\omega$, ref. [58]. The relaxation time (diffusion length $l_d$) represents the decay time (length) of the SW amplitude to 1/e of its initial value. $\tau$ can decrease from hundreds of ns to a few ns over the dispersion spectrum [65]. At $v_g$ of a few km/s, these values of $\tau$ lead to $l_d$ of hundreds to a few µm. Additionally, $\tau$ decreases with $\alpha$, a material property known as the Gilbert damping parameter (introduced in chapter 2.6). The choice of magnetic materials with low Gilbert damping parameter is vital for the implementation of exchange SWs in data transport. $Y_3Fe_5O_{12}$ ($\alpha = 2\cdot10^{-4}$, ref. [31]), $Ni_{81}Fe_{19}$ ($\alpha = 7\cdot10^{-3}$, ref. [68]), $Co_{40}Fe_{40}B_{20}$ ($\alpha = 4\cdot10^{-3}$, ref. [69]) or $Co_2Mn_{0.4}Fe_{0.6}Si$ ($\alpha = 3\cdot10^{-3}$, ref. [70]) are materials that in thin film form have the lowest Gilbert damping parameters at room temperature. Despite the strong reduction of $\tau$ and $l_d$ for exchange spin waves, $l_d/\lambda$, that gives the number of wavelengths a SW travels before relaxation, increases with $k$ and can be as large as a few thousands for exchange

SWs [65]. Thus, exchange SWs with long diffusion lengths and large group velocities could find application in data transport and computing applications. Additional to ideal materials (with large saturation magnetization and exchange constant, low Gilbert damping) and optimal geometries, practical aspects as excitation of SWs with a well-defined wavelength, generation efficiency, frequency, spatial and temporal detection resolution as well as compatibility with existing technology will decide the prospect of integrating SWs in future information processing.

## 1.5 Magnetic anisotropy

Anisotropic magnetic materials are characterized by a preferential orientation of the magnetization ***M*** along certain directions (known as easy axes of magnetization) determined by magnetic anisotropy. All the other directions are referred to as magnetic hard axes. Based on the origin, magnetic anisotropy is classified into: magnetocrystalline, shape, growth-, strain- and field-induced, each leading to a characteristic easy axis of magnetization. Magnetic anisotropies are quantified by the anisotropy energy density $K = E \cdot V^{-1}$, where $E$ is the energy required to rotate ***M*** from the easy towards a hard axis direction, and $V$ is the sample volume. Conventionally, for thin films, a negative anisotropy energy density corresponds to an in-plane easy axis of magnetization.

The alignment of ***M*** along a crystallographic direction for a demagnetized crystal is the result of magnetocrystalline anisotropy. The orbital moment of the electrons couples with the crystal electric field and, via spin-orbit coupling, the spin magnetic moments of the electrons orient along a preferred crystallographic direction. For cubic crystals, the anisotropy energy density, in spherical coordinates, up to the second order parameter, is given by

$$\frac{E}{V} = K_1(\alpha^2\beta^2 + \beta^2\gamma^2 + \gamma^2\alpha^2) \; + \; K_2\alpha^2\beta^2\gamma^2$$

where $\alpha = \cos\varphi \cdot \sin\theta$, $\beta = \sin\varphi \cdot \sin\theta$ and $\gamma = \cos\theta$ define the magnetization direction with respect to the <001> cubic axes. The anisotropy parameters $K_1$ and $K_2$ are material and temperature dependent. The values and sign of $K_1$ and $K_2$ indicate the direction of the magnetic easy axis. At room temperature, the magnetocrystalline anisotropy of most iron garnets is often described only by $K_1$, ref. [18]. The negative sign of $K_1$ indicates that the <111> directions are the magnetic easy axes. As a consequence, RIG thin films with an intended out-of-plane magnetic easy axis are often grown on (111)-oriented substrates. At room temperature, rare-earth iron garnets have weak magnetocrystalline anisotropy ($K_1$ is mostly below -10 kerg/cm$^3$, ref. [18]) compared to, for example, magnetite ($K_1$ = -125 kerg/cm$^3$, ref. [71]).

Another source of magnetic anisotropy is the shape of a magnetic object. In thin film form, the dipole-dipole interaction between magnetic moments favors an in-plane magnetic easy axis. The state of magnetic moments oriented in the film plane corresponds to the lowest energy state [72]. The shape anisotropy density $K_s$ is proportional with the square of the saturation magnetization $M_S$

$$K_s = -2\pi M_S^2 \qquad \text{(CGS units)} \qquad (1.1)$$

$$K_\mathrm{s} = -\tfrac{1}{2}\mu_0 M_\mathrm{S}^2 \qquad \text{(SI units)}$$

Here $\mu_0$ is the vacuum permeability. Thin films of materials with weak magnetocrystalline anisotropy are in-plane magnetizated as a result of dominant shape anisotropy, as it is the case for YIG films grown on lattice-matching $Gd_3Ga_5O_{12}$ substrates [31].

Epitaxial films deposited on substrates with slightly different lattice constants show distorted unit cells. For pseudomorphic films, the in-plane lattice constants closely match the substrate unit cell, while the lattice parameter in the growth direction shrinks or expands accordingly. In case of magnetostrictive materials deposited on (111)-oriented substrates, the compressive or tensile strain, built in the [111] direction, represents a new source of uniaxial anisotropy that orients ***M*** perpendicular to the film surface [73,74]. The strain-induced magnetoelastic anisotropy $K_\sigma$ is proportional to the stress $\sigma^\perp$ and the magnetostriction coefficient $\lambda_{111}$

$$K_\sigma = -\frac{3}{2}\sigma^\perp\lambda_{111} \tag{1.2}$$

The stress $\sigma^\perp$ in the [111] direction is given by the change of the interplanar spacing $\Delta d^{444} = d^{444}_\mathrm{bulk} - d^{444}_\mathrm{film}$, Young's modulus $Y$, and Poisson's ratio $\mu$ as

$$\sigma^\perp = \frac{\Delta d^{444}}{d^{444}_\mathrm{bulk}} \cdot \frac{Y}{1+\mu} \tag{1.3}$$

where $d^{444}_\mathrm{bulk}$ and $d^{444}_\mathrm{film}$ are the bulk and film interplanar spacings. Thus, $\sigma^\perp$ is positive for in-plane tensile strain that generates the compression of the unit cell in the growth direction. According to eq. (1.2), thin films of materials with a negative magnetostriction coefficient show an out-of-plane (oop) magnetoelastic contribution $K_\sigma$ under oop compressive strain. Thus, for strained films with weak magnetocrystalline anisotropy, strain-induced and shape anisotropies compete for the direction of the magnetic easy axis. Magnetostriction parameter $\lambda_{111}$ of rare-earth iron garnets and the required ip strain for achieving an out-of-plane magnetoelastic contribution are summarized in *Table 1*.

For single crystals, the arrangement of atoms in the lattice gives rise to an additional type of anisotropy. Growth-induced anisotropy is observed after faulty growth procedures that induce an incorrect stacking of magnetic ions along the growth direction.

A sufficiently strong magnetic field ***H*** applied onto a magnetic material rotates the magnetization in the field direction. Cooling down the sample in the presence of the magnetic field freezes ***M*** in the direction of ***H***. A new magnetic easy axis is obtained when ***M*** maintains this orientation after removing the applied magnetic field.

Most magnetic materials show more than one type of anisotropy and the dominant one dictates the direction of ***M*** in the demagnetized state. Of interest for this work are the magnetocrystalline, shape and stress-induced anisotropy.

*Table 1.* Room temperature magnetostriction parameter $\lambda_{111}$ of $R_3Fe_5O_{12}$, ref. [18].

| $R$ | Magnetostriction parameter $\lambda_{111} \cdot 10^6$ | Required in-plane strain |
|---|---|---|
| Y | -2.73 | tensile |
| Sm | -8.5 | tensile |
| Eu | +1.8 | compressive |
| Gd | -2.9 | tensile |
| Tb | +12 | compressive |
| Dy | -5.9 | tensile |
| Ho | -3.4 | tensile |
| Er | -4.9 | tensile |
| Tm | -5.2 | tensile |
| Yb | -4.5 | tensile |

# 2 Film growth and characterization methods

In this chapter are described the growth and characterization techniques applied to the thin films of this work. First, key processes of the pulsed laser deposition technique are presented. Atomic and magnetic force microscopy were applied for the surface characterization and imaging of magnetic domains, respectively. In the following, the working principle of Rutherford backscattering spectroscopy and energy dispersive X-ray fluorescence are briefly described. The crystal structure was analyzed by X-ray diffraction. In the end, key elements of the superconducting quantum interference device magnetometer, magneto-optical Kerr effect and ferromagnetic resonance are covered.

## 2.1 Pulsed laser deposition

Among the physical vapor deposition techniques, pulsed laser deposition (PLD) stands out as a versatile method for the growth of thin films. Its implementation in the deposition of high temperature superconductors generated a strong interest for the usage of the technique in thin film deposition [75]. Nowadays, PLD is successfully implemented in the growth of films from stressed or stress-free single crystals, quasicrystalline layers [76] to biomaterials with application in fundamental research and also industry. The broad application range results from the peculiar features of the technique: usage of solid, polymer [77] or even liquid [78] targets, flexible adjustment of the growth parameters (for example, deposition rate or laser pulse energy optimized to the target material), stoichiometric transfer of target material onto the substrate, possible addition of oxygen or nitrogen atmosphere required for the growth of oxides or nitrides.

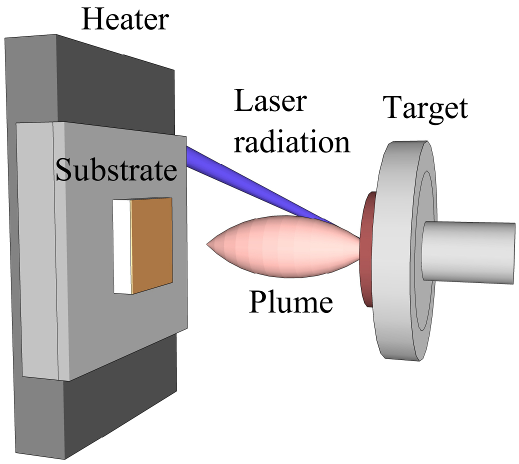

*Figure 4.* Illustration of film growth by pulsed laser deposition.

The growth mechanism of thin films by PLD is illustrated in *Figure 4*. Laser pulses, generated outside of the deposition chamber, are focused onto the target. For laser pulse energies larger than a certain threshold, the irradiated spot is vaporized. The ejected material, forming the ablation plume, is directed mainly forward towards the substrate placed in front of the target.

Often the substrate is mounted on a heater allowing the growth of thin films at elevated temperatures. Material transfer from the target onto the substrate involves several steps: generation of laser pulse, interaction of laser pulse with the target, propagation of ejected material towards the substrate, interaction of ejected particles with the substrate surface. The complexity of the technique mainly originates from the physical and chemical modifications of the target surface after each laser pulse. Thus, at each laser pulse, the radiation interacts with a new surface morphology. In the following, each process is described in more detail.

### 2.1.1 Generation of laser radiation

Atoms and molecules can change the energy state by interacting with electromagnetic radiation or energetic particles via three mechanisms: absorption, spontaneous emission and stimulated emission. Within an atom, an electron occupying the ground energy level (described by the energy $E_1$) can move to a higher unoccupied energy level (of energy $E_2$) by absorbing the energy of an incoming photon (with the energy $hf_{12}$) or of a particle (having the kinetic energy $E_c$). The condition for the transition to take place is $hf_{12} = E_2 - E_1$ or $E_c \geq E_2 - E_1$. The electron in the excited state $E_2$ can relax back to the ground level $E_1$ radiatively by spontaneously emitting a photon with the energy $hf_{21} = E_2 - E_1$ or non-radiatively by interactions with the lattice or other electrons. Photons emitted through spontaneous emission have random orientations, no phase correlation and form a monochromatic radiation. Furthermore, incoming photons having the energy $hf_{12}$ can stimulate the relaxation of an excited electron into the ground state. This process takes place with the emission of a photon having the energy, phase and direction of the incident photons resulting in the amplification of the incident radiation. However, the absorption process works against the stimulated emission. In order to favor the stimulated emission over absorption, more electrons have to be in the excited state than in the ground level, i.e. a population inversion has to be created. A laser is a device emitting coherent radiation by stimulated emission. Various chemical elements and compounds can be utilized as solid or gaseous laser sources producing poli or monochromatic radiation over a broad spectral range from the ultraviolet region (for example, nitrogen lasers) to far infrared (for example, helium neon lasers). For the growth of the thin films investigated in this work a KrF laser was used, therefore, the working principle of this type of lasers is described in more detail.

The laser cavity contains the filling gas, also known as gain medium. For the KrF laser the gain medium is formed by a mixture of krypton atoms and fluorine molecules. Electrons, produced by an electric discharge, transfer part of their energy to the gain medium through collisions with the krypton atoms and fluorine molecules. Ions and atoms in excited state (marked with an asterisk) are produced according to the reactions

$$e^- + Kr \rightarrow Kr^+ + e^- + e^-$$

$$e^- + Kr \rightarrow Kr^* + e^-$$

$$e^- + Kr + Kr \rightarrow Kr_2^+ + e^- + e^-$$

$$e^- + F_2 \rightarrow F^- + F$$

Kr ions and excited atoms are highly reactive. They bound with the F ions and molecules, and form krypton fluoride molecules in the $^2\Sigma^*$ excited state as follows

$$Kr^+ + F^- + X \rightarrow KrF^* + X$$

$$Kr_2^+ + F^- \rightarrow KrF^* + Kr$$

$$Kr^* + F_2 \rightarrow KrF^* + F$$

Here X represents molecules from a buffer gas. The addition of a buffer gas (for example Ne or He) in high concentrations (around 95 %) is necessary to reduce the momentum transfer cross-section of the gas [79]. The $^2\Sigma^*$ state of the krypton fluoride complex is a metastable state and after a mean lifetime of 7 ns (ref. [80]) the molecule spontaneously relaxes into the $^2\Sigma$ ground state emitting a photon randomly oriented with the wavelength $\lambda = 248$ nm. The $^2\Sigma$ ground state is thermally unstable and the molecule dissociates in < 1 ps (ref. [80]) into the two constituents. Therefore, no KrF complex exists in the ground state and the population inversion required for the amplification of laser radiation is always accomplished. The newly formed Kr and F atoms re-enter the cycle and the spontaneously emitted photons contribute to the stimulated emission of additional photons.

At the sides of the laser cavity two mirrors are placed. Photons travelling along the axial direction are reflected by the two mirrors and pass several times through the gain medium. Thus, laser radiation travelling along this direction becomes strongly amplified. Pulses of laser radiation leave the cavity through one of the mirrors that is partially transparent at the used wavelength.

### 2.1.2 Interaction of laser light with matter

Several processes take place at the target upon laser irradiation for the ablation of a small target volume and growth of thin films: absorption of incident laser light, diffusion of gained energy, melting and evaporation of the target surface. The material property that determines whether the photon energy is absorbed or reflected by the target surface is the extinction coefficient $k$.

The angular frequency $\omega$ dependence (or wavelength $\lambda$, $\omega = 2\pi v \lambda^{-1}$, where $v$ is the light velocity in the material) of the extinction coefficient $k(\omega)$ is material specific and shows distinctive features for metals, semiconductors or insulators. At angular frequencies $\omega$ higher than the plasma frequency $\omega_p$, the free electrons of metals and free carriers of semiconductors (for high free carrier densities) oscillate in phase with the incident light. As a result, incident light with $\omega > \omega_p$ (or $\lambda < \lambda_p$) does not penetrate the material and it is completely reflected. Even though the plasma frequency is material specific, $\omega_p$ is in the visible/UV and IR region for metals and semiconductors, respectively. For band gap materials, $k(\omega)$ shows absorption features corresponding to transitions between bands only at photon energies that match the energy gap of the involved bands.

A laser radiation incident on a target interacts only with the electrons of the target atoms since the heavy nuclei cannot react to the high frequency of the commonly used laser radiation. Additionally, the light-matter interaction is mainly due to the electric component of the electromagnetic wave since the magnetic contribution in the Lorentz force acting on the electron can be neglected.

For metallic targets, free electrons mediate the light absorption. In case of semiconducting and insulating materials, the light absorption is achieved via generation of free carriers (electrons and holes) upon irradiation at photon energies equal to the band gap energy. The high energy gap of insulators calls for UV laser light, while visible or IR light is sufficient to generate transitions from the valence band into the conduction band of semiconductors.

At the irradiated spot, the electron system absorbs the photon energy resulting into a steep increase of the electron temperature. In less than 0.1 ps the electron system reaches thermal equilibrium through electron-electron collisions [81]. The electrons dissipate energy to the lattice through electron-phonon interactions. The thermal equilibrium of the phonon system is reached within picoseconds via phonon-phonon interactions [82].

The amount of light absorbed by a material upon irradiation is given by the absorption coefficient. The initial rise in temperature leads to an increase of the free carrier density since band gaps decrease with temperature. As a result, the absorption coefficient, which shows a linear dependence on carrier density, continues to increase further heating up the irradiated spot. A large absorption coefficient, corresponding to a small optical penetration depth, in combination with a low thermal diffusion coefficient generates a concentration of the absorbed energy within a shallow layer on the target surface. Within nanoseconds after irradiation a steep increase in the surface temperature takes place. At surface temperatures above the vaporization point, target material is ejected from the irradiated spot. Therefore, threshold laser intensities, dependent on the target material, have to be surpassed and common values are in the range $10^8 - 10^9$ W/cm$^2$ for ns long laser pulses [81]. The vaporized volume is surrounded by molten material that extends in depth for a few hundreds of nm, a range mainly influenced by the laser pulse duration. The molten volume solidifies in hundreds of ns, ref. [83].

For ultra short pulse durations (~ 100 fs), the removal of target material is not achieved by evaporation since on this timescale the electron system does not transfer energy to the lattice. Laser ablation with fs long pulses is commonly carried out at intensities around $10^{13}$ W/cm$^2$, ref. [81]. Such intense laser pulses exceed the binding energy and, as a result, electrons and ions are generated at the irradiated spot. Electrons produced in the early stage of the laser pulse absorb incident photons until the termination of the laser pulse. The photon absorption occurs through electron-ion collisions (inverse Bremsstrahlung effect), and, as a result, the electron temperature increases. As thermal equilibrium between electrons and ions is reached in picoseconds [81], the ion energy remains unchanged during irradiation. For gained energies larger than the electron work function, electrons are removed from the target. Additionally, ions are pulled from the target via the electric field created by the charge separation [84].

### 2.1.3 Influence of background pressure on plume propagation

Intense laser pulses evaporate the irradiated target spot forming a highly dense plume ($10^{19} - 10^{21}$ particles/cm$^3$, ref. [85]) at the target surface. Optical absorption and emission spectroscopy show that electrons, neutral and electronically excited atoms and ions, molecules (for multi-component targets) and clusters form the plume [86,87]. Additionally, particulates (droplets with the size in the µm range) can be observed embedded in the thin films. An increased target roughness [88] or the plume expanding towards the molten target surface [89] are considered the origin of these droplets. Modifications of the experimental setup [90], increasing the laser fluence in case of metallic targets [91], increasing the target density or using smooth targets were found to completely eliminate or strongly reduce the droplets density.

After evaporation, the ablated material absorbs the incident laser radiation. Mean plume temperatures as high as $10^5$ K have been measured after the irradiation of an amorphous carbon target [92], while the evaporation temperature of carbon is around 2000 K. The radiation absorption is thought to occur via electron-ion interaction in which electrons absorb incident photons and gain kinetic energy (inverse Bremsstrahlung effect). The absorption coefficient of the plume is proportional, among other parameters, with the square of ion density [85]. Such high plume temperatures correspond to a degree of ionization larger then normally contained in the evaporated material. Local hot spots arising from non-uniform laser beams or additional photoionization processes could increase the degree of ionization [93]. The radiation absorption involving neutral particles is less efficient and occurs for high densities of neutral particles.

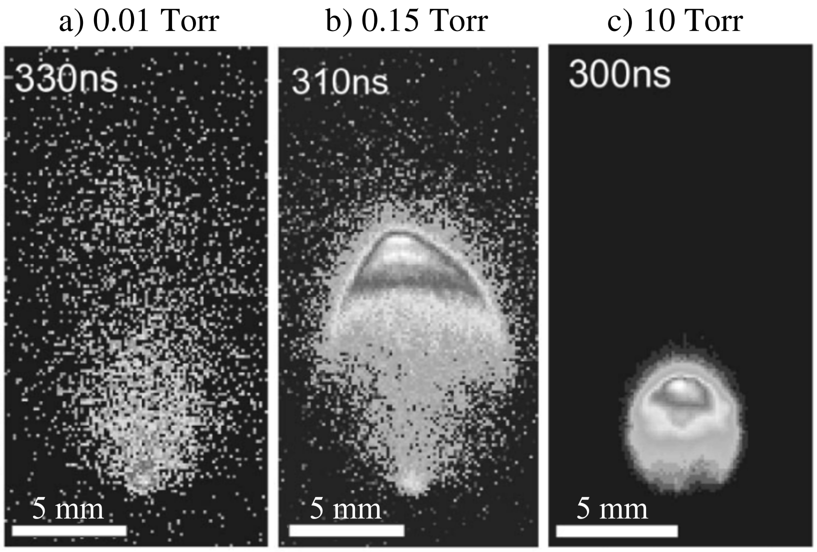

*Figure 5.* Images of light emission from plume species at *a)* 0.01 Torr, *b)* 0.15 Torr and *c)* 10 Torr background air pressure taken at around 300 ns after the plume onset. Each picture is normalized to its maximum intensity. Reproduced from Harilal et al. [94], with permission of AIP Publishing.

Several parameters influence the plume dynamics: irradiation spot size, laser pulse intensity, duration and wavelength, or the gas composition and pressure in the deposition chamber [95]. Intensified charged coupled device (ICCD) images taken at various time delays after the plume onset in a broad background pressure range ($10^{-6}$ – 100 Torr) reveal a pressure dependent propagation mode of the plume [94]. In vacuum and very low background pressure (*Figure 5 (a)* 0.01 Torr = 0.0133 mbar), the plume expands freely due to the absence of interactions between plume and gas particles. An almost uniform particle distribution within the measured window is observed after ~ 300 ns. In the vicinity of the target surface a light emission spot is detected up to 1 µs delay time. This emission region is thought to originate from the collision of the ejected plume with stopped and/or backward species. With increasing the background pressure to 0.15 Torr, a division of the plume into two parts is observed: a fast moving component at the front and a slow moving or stationary component at the target surface (*Figure 5 (b)*). A sharpening of the fast component occurs with time indicating that the fastest particles are emitted from the target along the surface normal. At intermediate pressures, the ejected species decelerate as a result of the interaction with the background gas. Increasing further the gas pressure results in a lateral and forward confinement of the plume (*Figure 5 (c)*). For gas pressures higher than 10 Torr, the front part of the plume slows down very fast and no plume splitting is observed. Within the investigated pressure range, the plume length is observed to decrease with gas pressure. Thus, a reduction of the number and velocity of plume species at the substrate position is achieved with increasing the background pressure. The ICCD images reported by Harilal et al. show the emissions in the optical visible range of excited plume species [94]. Thus, the non-radiative component of the plume and the species emitting out of the optical visible range are not imaged with this technique and the overall expansion behavior of the plume might show additional features.

Depending on the laser pulse energy and duration, plume species have energies of tens (for atoms) up hundreds eV (for ions) [96]. Reaching the film surface with such high energy can result in particle implantation [97] or sputtering of the deposited surface layers [98]. Inserting a gas in the deposition chamber during the film growth allows the reduction of the particles kinetic energy down to a few eV.

Adjusting the ratio of the chemical elements reaching the substrate surface is also accomplished via the background gas. The propagation dynamics of the ejected material is influenced by the chamber pressure and a preferential scattering of lighter elements in case of multi-component targets is observed [99], resulting in modification of the film stoichiometry. Additionally, numerous reports showed that oxide films deposited by PLD at low oxygen pressure show oxygen deficiency [100]. Despite the control of vacancy density offered by PLD with effect on the film magnetic, electronic and transport properties (as an example, the transition of $NdNiO_3$ from insulator to a conductive behavior by decreasing the oxygen vacancies [101]), often no deviation from the ideal film stoichiometry is desired. An increased incorporation of oxygen atoms in the films is achieved in oxygen atmosphere as oxygen molecules collide with electrons, present in the ablated volume, and dissociate into oxygen atoms that react with plume species and the deposited layers [102]. A similar reduction of vacancies can be obtained by post-annealing in air or properly selected atmosphere. Therefore, the usage of a background gas might be necessary for the growth of stoichiometric films from off-stoichiometric targets.

### 2.1.4 Film thickness distribution and stoichiometry

The images displayed in *Figure 5* were taken for normal angles of laser incidence. In such cases, the plume always expands along the target normal. A similar propagation direction is observed for non-normal angles of laser incidence when short laser pulses (no laser-plume interaction takes place) irradiate flat targets. Plume tilting towards or away from the laser incident direction occurs due to pseudo-craters, columnar structures, high laser fluences, asymmetric or non-uniform spot profiles on the target [103].

In vacuum, the plume has a $\cos^n\theta$ angular distribution, where $\theta$ is measured relative to the target normal and $n$ is a positive number. At the substrate position, the plume angular distribution leads to a $\cos^{n+3}\theta$ angular distribution of the deposited material. At close distances to the substrate surface, collisions of the incoming particles with particles reflected by or sputtered from the film surface cause a broadening of the angular distribution. The increase of the laser spot area, while maintaining a constant fluence, causes a narrowing of the deposition profile. No dependence on the laser fluence was observed, while the studies on laser pulse duration and wavelength are inconclusive [103].

The growth of stoichiometric multi-component films by PLD represents an important advantage of the technique. Composition measurements of $YBa_2Cu_3O_{7-x}$ films deposited in vacuum reveal an enrichment of light elements. The addition of oxygen atmosphere leads to a preferential scattering of the light elements [104]. Additional studies revealed for $BaTiO_3$ films the control of cation stoichiometry as a function of the used laser fluence [105]. While the film composition can be adjusted via the background gas or the laser fluence, the observed spatial distribution of the chemical elements across the substrate surface draws attention to one limitation of the PLD technique. Rutherford backscattering spectroscopy (RBS) measurements revealed for $YBa_2Cu_3O_{7-x}$ films deposited in vacuum a uniform chemical distribution on a rather small area (around 0.5 cm). An increase of the area with uniform stoichiometry to ~ 1 cm was measured for films grown in a 200 mTorr oxygen atmosphere [104]. The limitation of the technique for the growth of large size films with uniform thickness and stoichiometry can be overcome by lateral movement of the laser beam across the target surface and/or the substrate.

### 2.1.5 Film growth

Nowadays, all electronic devices are formed by stacking thin films with different properties on top of each other. Such an example is the giant magnetoresistance (GMR) sensor. As a result of the small vertical dimensions of these structures, a fine control of the interface quality is required. PLD, through the possible adjustment of the kinetic energy of the plume species, can promote the growth of atomically sharp interfaces and film surfaces.

The mechanisms a particle undergoes on a surface are depicted in *Figure 6*. Adsorption is the adhesion of a particle to the surface. However, highly energetic particles can be implanted in the substrate. An adsorbed particle remains on the surface as long as the thermal energy is lower than the activation energy of desorption. As temperature increases, the probability for a particle to leave the surface increases. The incoming particle is reflected through a collision with a surface atom. The two contributions to the adatom mobility are the thermal energy provided by heating up the substrate, and the energy gained after the collision with an incident particle promoting lateral diffusion and/or intermixing with the substrate.

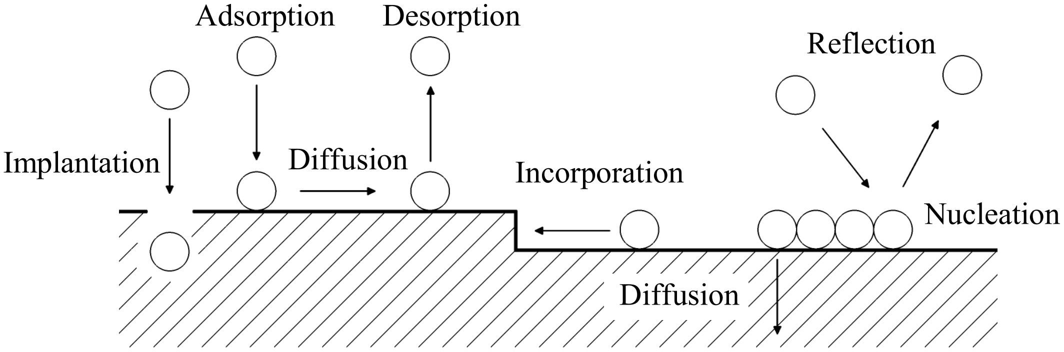

*Figure 6.* Illustration of the processes a particle undergoes on a surface.

At energies in the $1 - 10^3$ eV range that particles typically have in the ablation plume, the growth of thin films by PLD is not in thermodynamic equilibrium. The growth mechanism, that in the end influences the film properties, is influenced by the substrate type and temperature, energy and deposition rate of incoming particles. Films deposited on closely lattice-matching substrates follow the substrate crystal structure resulting in 2D growth modes. Often the single crystal substrates used for the growth of epitaxial films show terraces on the surface separated by steps. After being cut from bulk, single crystal substrates are mechanically polished to the specified roughness. This step destroys the crystalline structure of the surface. For the epitaxial growth of high quality films, the substrate surface has to be recrystallized. The recovery of the crystalline structure is achieved by annealing at elevated temperatures. As a result of a small miscut angle during the cutting process, terraces are visible after the heat treatment.

At high vapor saturation in the substrate vicinity, particles condensate on the surface at a high nucleation rate and surface kinetics influences the film growth. The most important parameter is the diffusion coefficient which depends on the deposition temperature $T$ as $e^{-1/T}$. The diffusion of atoms across and to another terrace dictates the growth mode. For surface diffusion lengths of the adatoms larger than the average terrace width, the particles move across the terraces and no nucleation center is initiated. If adatom diffusion to a lower terrace takes place and the terrace edges act as sinks, a step flow growth is observed. On the contrary, small diffusion lengths lead to nucleation centers. At high nuclei density, existing nuclei continue to grow as the probability for an adatom to initiate a new nucleus center decreases. The diffusion of particles across edges influences the emerging growth mode. If incoming particle diffuse over the island edge to a lower level and no nucleation starts before the completion of a layer, the film grows layer-by-layer. For low diffusion across island edges, the islands continue to grow [81]. Experimentally, the identification of the balance between energy and rate of incoming particles, and substrate temperature is crucial for the growth of high quality films.

## 2.2 Imaging techniques

The surface morphology of the films prepared in this work was studied by atomic force microscopy (AFM). Replacing the standard AFM tip with a magnetic one, leading to the so-called magnetic force microscopy (MFM), allows imaging of magnetic domains. In the following, the working principle of AFM and MFM is described.

### 2.2.1 Atomic force microscopy

Atomic force microscopy is an imaging technique implemented in surface analysis, 3D imaging and atom manipulation [106]. The characteristics by which AFM outperforms optical and electronic microscopy include: nm lateral and sub-nm vertical resolution; no sample preparation is required and, therefore, the sample suffers low or no damage; measurements on metals, semiconductors or insulators can be carried out in air, liquid or vacuum conditions; the acquisition of surface images requires a moderate skill level while the data interpretation is straightforward.

The high spatial resolution achieved in AFM is the consequence of using a sharp tip and a scanner. AFM probes consist of a tip (at apex it is < 10 nm in diameter) located at the free end of a cantilever (a few hundreds of μm long) fixed on a substrate. The vertical (*z* direction) and lateral (*xy* plane) positioning of the AFM probe over the sample surface are adjusted by the scanner. The scanner, having a cylindrical shape divided into segments, is made out of piezoelectric ceramics that change geometry under an applied voltage. Therefore, various combinations of applied voltages allow each segment to be individually actuated resulting in the high spatial precision in lateral movement.

In an AFM measurement, the interaction between the tip and the sample is monitored while the probe scans the sample surface. The tip is brought in close vicinity to the sample surface by the piezoelectric actuators. During the approach, the forces between the tip and the surface vary with tip-surface spacing. At large distances, weakly attractive van der Waals and electrostatic forces act between the tip and sample atoms. As the tip approaches the sample surface, the attractive forces increase until the electron clouds and ions of the tip and sample surface start to repel each other. As the tip-sample distance continues to decrease (< 1 nm), the total force decreases until the repulsive forces compensate the attractive forces. Only repulsive forces act between the tip and the sample for lower separation distances [107].

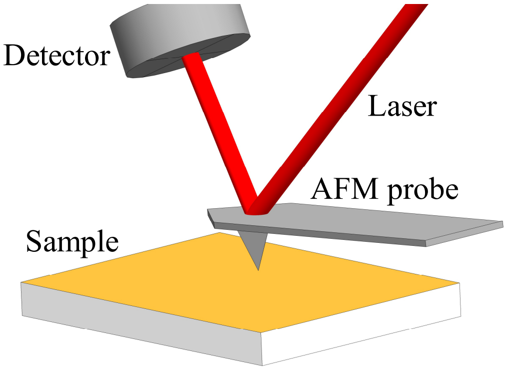

*Figure 7.* Simplified sketch of the atomic force microscope.

In an AFM measurement the deflection of the cantilever is optically monitored. A laser beam shines on the backside of the cantilever and it reflects to a photodetector. As the tip scans the sample surface, changes of the force between the tip and the sample bend the cantilever resulting in the displacement of the laser spot on the photodetector (*Figure 7*).

AFM mainly operates in two modes [107]: contact mode and tapping mode. In both cases, a feedback loop is used in order to keep constant the parameter of interest. In contact mode, the tip is brought in contact with the investigated surface. During the measurement, the bending angle of the cantilever is kept constant. Any change of topography encountered by the tip during surface scanning influences the bending of the cantilever and the laser spot moves over the detector. Based on the detected signal, the control feedback loop adjusts the $z$ position of the tip in order to restore the initial orientation of the cantilever. In tapping mode, the tip oscillates vertically touching alternatively the sample surface. Thus, the detector measures a sinusoidal signal. In this case, the oscillation amplitude is kept constant. As the tip scans the sample surface, changes of topography increase or decrease the oscillation amplitude and the detector signal is distorted. A feedback loop changes the $z$ position of the tip in order to maintain constant the oscillation amplitude. In both measuring modes, the displacement of the laser spot on the photodetector reflects the surface topography and the measured signal is converted into a 2D picture.

Additional to surface imaging, various physical properties are investigated by monitoring other parameters. For example, short and long range interactions between the tip and the sample affect the cantilever oscillation phase. The changes in phase are caused by variations in composition, friction or viscoelasticity (short range) and electric or magnetic fields (long range).

### 2.2.2 Magnetic force microscopy

The magnetic domain structure of a magnetic sample can be also imaged by AFM. For this, the tip is coated with a magnetic layer and the technique is known as magnetic force microscopy (MFM). The $z$ component of the force $\vec{F}$ acting on the tip causing the phase variation depends on the tip magnetization $\boldsymbol{M}_{\text{tip}}$ and the stray field $\boldsymbol{H}_{\text{sample}}$ created by the sample [107]

$$F_z = -\mu_0 \int \boldsymbol{M}_{\text{tip}} \cdot \frac{\partial}{\partial \text{z}} \boldsymbol{H}_{\text{sample}} \, \text{d}V$$

where $\mu_0$ is the magnetic permeability of free space and the integration is carried out for the volume $V$. When using an in-plane magnetized tip, contrast is created along the domain walls for an in-plane magnetized sample and across the magnetic domain for an out-of-plane magnetized sample as shown in *Figure 8*.

During the MFM measurement, the magnetic domain structure is imaged together with the topography. First, the tip scans laterally the sample and one line of the surface topography is measured. At the end of the scan line, the cantilever is lifted at a height selected by the user. The lift height is influenced by parameters like magnetic moment of the tip, stray field created by the sample. At the new $z$ position, the phase change is monitored as the tip follows the topography registered during the first step. Thus, both surface morphology and domain structure can be imaged during an MFM measurement.

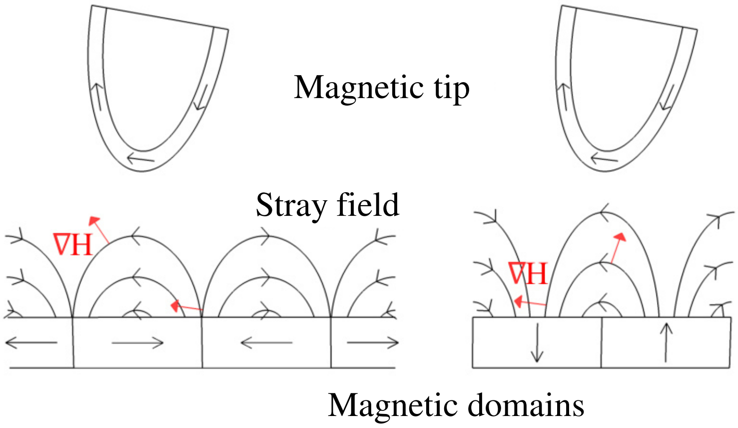

*Figure 8.* Schematics of stray field lines for (left) an in-plane and (right) out-of-plane domain structure. In both cases an in-plane MFM probe is displayed. The field gradient is market at various positions with red arrows.

## 2.3 Chemical analysis

Pulsed laser deposition, through the usage of a background gas, allows a fine adjustment of the ratio of chemical elements reaching the substrate. The stoichiometry analysis of the films investigated in this work was carried out by Rutherford backscattering spectroscopy and energy dispersive X-ray fluorescence.

### 2.3.1 Rutherford backscattering spectroscopy

A powerful technique for elemental analysis of layered or bulk samples is Rutherford backscattering spectroscopy (RBS). It has been proven valuable for the concentration evaluation and identification of chemical elements as well as their depth distribution while relying on a simple physical mechanism.

A beam of particles (commonly $He^+$ or alpha particles) impinges on the investigated sample, also referred to as target. In the target material, a fraction of the alpha particles undergo inelastic collisions with the target nuclei. After the collisions, the alpha particles lose part of the initial energy and are randomly scattered. Only a small amount of the initial particles escape the target and reach the detector placed at a fixed angle (in the Cornell geometry, the detector is positioned at 170° relative to the incoming direction). Information regarding the nature, concentration and depth distribution of chemical elements is obtained by counting the number and measuring the energy of the detected particles [108].

*Figure 9* displays the sketch of a typical experimental geometry together with the corresponding ideal RBS spectrum for the case of a two-component thin film on a substrate with a lower atomic mass. An RBS spectrum shows the number of detected particles for a certain channel number or energy. Experimentally, deviations from the ideal squared peak shape are observed as consequences of the finite energy resolution of the detector, the energy straggling of the alpha particles at a certain depth and the finite diameter of the beam and detector [109].

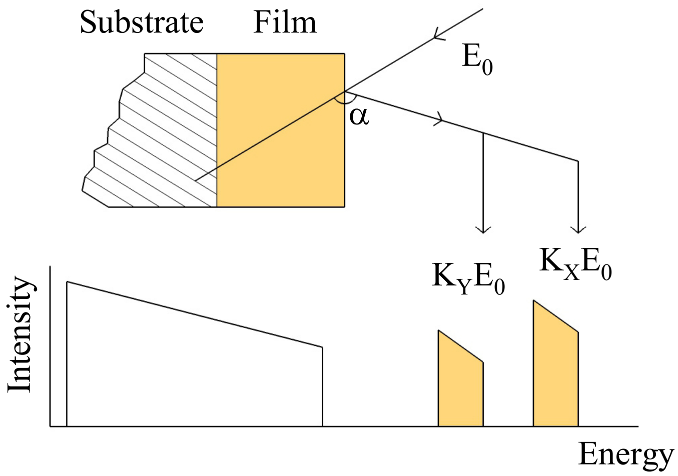

*Figure 9.* Sketch of an RBS experiment (top) and the corresponding ideal spectrum (bottom).

In *Figure 9* the film consists of two elements $X$ and $Y$ of mass $M_X$ and $M_Y$, respectively with $M_X > M_Y$. After the collision with a target atom $i$ (where $i = X$ or $Y$), the energy of the alpha particle $E_i$ is proportional with the initial energy $E_0$ via the kinematic factor $K_i$. The kinematic factor $K_i$ depends on the backscattering angle $\alpha$ and the masses of the alpha particle $M_a$ and target atom $M_i$ as

$$K_i = \left[\frac{(M_i^2 - M_a^2 \sin^2 \alpha)^{\frac{1}{2}} + M_a \cos \alpha}{M_a + M_i}\right]^2$$

$K$ has values between 0 and 1 and it increases with the mass of the target atoms while $\alpha$ and $M_a$ are fixed. After a collision with atom $X$ the alpha particle has a higher energy than after a scattering process with atom $Y$. As a consequence, heavy elements give rise to peaks on the high energy side of the spectrum and light elements on the low energy side (*Figure 9*). Thus, the energy scale can be converted in a mass scale and the atom identification is based on the peak position.

Only a small fraction of the incoming beam undergoes collisions with the surface atoms. The rest of the particle beam travels through the film. As a particle travels through the film it loses energy and the amount of lost energy is related to the film thickness, atomic density and stopping cross-section factor [110]. In an RBS spectrum, the alpha particles that give rise to the high energy side of a peak are scattered from the film surface while particles scattered from the backside of the film contribute to the low energy side of the peak. Thus, the energy scale can be seen as a depth scale and the film thickness is correlated to the peak width.

For a thin film $X_mY_n$ the atomic ratio can be calculated using

$$\frac{n}{m} = \frac{C_Y}{C_X} \cdot \frac{\sigma_X}{\sigma_Y} \tag{3.1}$$

where $C_i$ and $\sigma_i$ are the integrated peak counts and the cross-section of element $i$ with $i = X$ or $Y$. Furthermore, the cross-section depends on the atomic number $Z_a$, energy $E$ and mass $M_a$ of the alpha particle, atomic number $Z_i$ and mass $M_i$ of element $i$, and scattering angle $\alpha$ through the relation

$$\sigma_i = \left(\frac{Z_a Z_i e^2}{4E}\right)^2 \cdot \frac{4\left[(M_i^2 - M_a^2 \sin^2\alpha)^{1/2} + M_i \cos\alpha\right]^2}{M_i \sin^4\alpha\,(M_i^2 - M_a^2 \sin^2\alpha)^{1/2}} \tag{3.2}$$

Here $e^2 \approx 1.44 \cdot 10^{-13}$ MeV·cm. Thus, the stoichiometry of a layer can be calculated using the measurement and eq. (3.1) and (3.2) considering known the scattering angle and the type of atoms. Furthermore, the scattering cross-section scales with the squared of the target atomic number, thus, RBS is more sensitive to heavy elements than to light elements.

### 2.3.2 Energy dispersive X-ray fluorescence

Another non-destructive technique for composition analysis is energy dispersive X-ray fluorescence (EDXRF). The elemental composition of solid (bulk and thin films) or liquid samples is identified with a table-top instrument allowing measurements in air or under vacuum conditions.

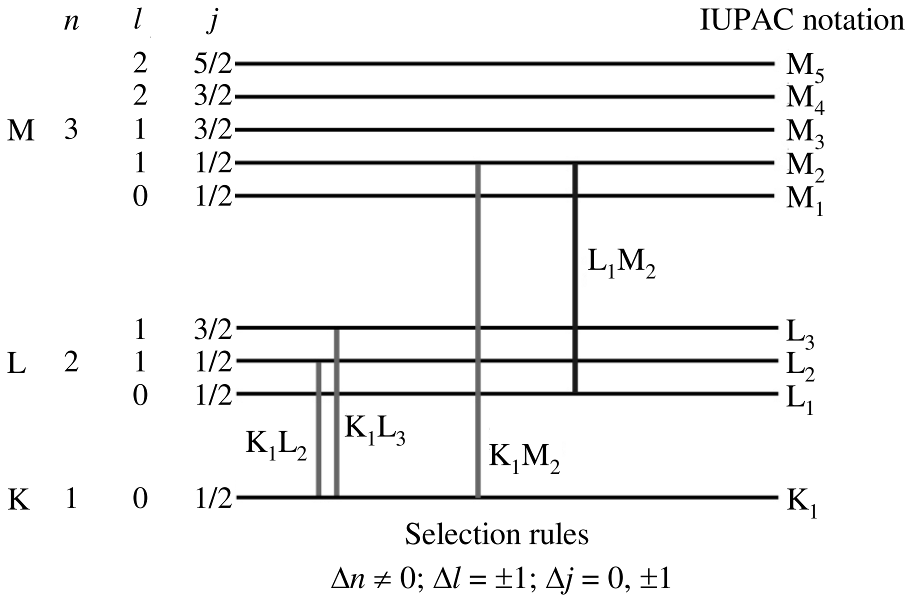

*Figure 10.* Energy level diagram illustrating various allowed electron transitions. The quantum numbers and the IUPAC notation of the orbitals are indicated.

The technique relies on the X-ray fluorescence process [111]. X-ray radiation, generated inside the X-ray tube, irradiates the investigated material. Incident photons with sufficient energy ionize the sample atoms by expelling electrons from the inner atomic orbitals. Outer shell electrons fill the inner shell holes by emitting element specific X-ray photons with energy given by the energy difference of the orbitals involved in the transition. Electron shells, denoted with K (principal quantum number $n = 1$), L ($n = 2$), M ($n = 3$), and further, consist of electron orbitals defined by the quantum number $l = 0, 1, .., n\text{-}1$; and the total angular momentum quantum number $|l - s| \leq j \leq l + s$ where $s = ½$ is the spin quantum number, as shown in *Figure 10*. Allowed transitions are denoted according to the shells and orbitals involved in the transition. The first part is given by the orbital into which the electron drops, while the second part denotes the orbital from which the electron originates. According to the IUPAC notation, the radiation emitted by an electron dropping from $3P_{1/2}$ ($M_2$) to $2S_{1/2}$ ($L_1$) is denoted $L_1M_2$. The energy of the emitted photons is detected by a solid-state detector. EDXRF spectra contain distinct peaks corresponding to the allowed transitions of the investigated material and X-ray source. While peak positions indicate the type of sample atoms (qualitative analysis), the quantitative analysis is performed using the peak area.

## 2.4 X-ray diffraction

On account of being a simple to implement and non-invasive method, X-ray diffraction (XRD) is a versatile technique primarily used for the study of crystalline structure and phase identification of single and polycrystalline specimens in bulk, powder or thin film form.

The technique relies on the wave nature of X-rays and its working principle is depicted in *Figure 11*, ref. [112]. For simplicity, the sample is represented here by a set of parallel planes formed by one type of atoms and separated by the interplanar distance $d$. A linear wave front of X-rays of wavelength $\lambda$ reaches the atoms under the incident angle $\theta$. The electron cloud surrounding each atom scatters the incident radiation as spherical waves. In *Figure 11* only a few of the outgoing directions are marked. Waves elastically scattered by successive planes undergo destructive (indicated by dashed outgoing lines) or constructive (solid outgoing lines) interference in specific directions. For the observation of constructive interference, the path difference between rays scattered by successive planes must be an integer number $n$ of wavelengths. According to *Figure 11*, the path difference between rays scattered by the top and second atomic planes is $2d\sin\frac{2\theta}{2}$. Thus, the interference condition is satisfied for

$$2d\sin\frac{1}{2}2\theta = n\lambda \qquad \text{(Bragg's law)}$$

where $2\theta$ is the angle made by the outgoing and incoming beams, also known as the diffraction angle. When the atomic planes are parallel to the sample surface, the diffraction angle is twice the angle at which the incident X-ray beam reaches the atomic plane, as shown in *Figure 11*. Experimentally, the crystal plane is not necessarily parallel to the sample surface. The angle at which the incident beam meets the sample surface is often denoted $\omega$. All samples investigated in this work are single crystals and prior to each measurement an aligning procedure is carried out so that $\omega = \theta$.

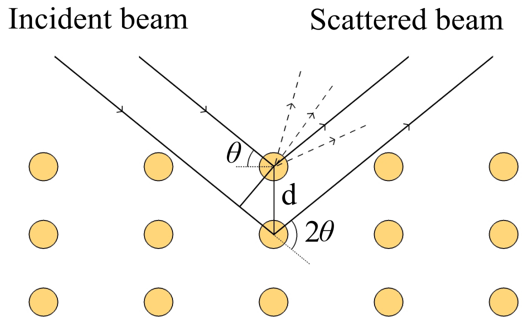

*Figure 11.* Illustration of the interaction of an X-ray beam incident under the angle $\theta$ with periodic planes of atoms separated by the interplanar distance $d$. Linear waves are scattered by the atoms as spherical waves. Dashed lines mark a few wave directions. $2\theta$ is the angle between incoming and outgoing beams for which constructive interference is observed.

Commonly, X-ray diffraction patterns are measured by symmetric $\theta - 2\theta$ scans in which, while rotating the sample (or the X-ray source) by $\theta$ and the detector by $2\theta$, the intensity of the scattered beam is measured. At the $2\theta$ angles that fulfill Bragg's law, the interference process is detected as an increased measured intensity known as diffraction maxima or peaks. According to Bragg's law, diffraction maxima should appear sharp at precise $2\theta$ angles, however, experimentally they are observed as broad peaks. The broadening of diffraction peaks is caused by instrumental resolution, microstructural defects, sample size; all of which can be identified through specific scans [112].

All the crystallographic information about the investigated material is included in the value of the interplanar distance $d$. Each plane of atoms in a unit cell is uniquely described by the Miller indices ($h$ $k$ $l$) and the interplanar distance is often denoted $d_{\mathrm{hkl}}$, ref. [112]. The interplanar distance is related to the unit cell edges ($a$, $b$, $c$) and angles between them ($\alpha$, $\beta$, $\gamma$) through the Miller indices, as shown below for a triclinic lattice

$$\frac{1}{d_{hkl}^2} = \frac{1}{V^2}\left(S_{11}h^2 + S_{22}k^2 + S_{33}l^2 + 2S_{12}hk + 2S_{23}kl + 2S_{13}hl\right)$$

$V$ = volume of the unit cell

$$S_{11} = b^2c^2\sin\alpha \qquad S_{12} = abc^2(\cos\alpha\cos\beta - \cos\gamma)$$
$$S_{22} = a^2c^2\sin\beta \qquad S_{23} = a^2bc(\cos\beta\cos\gamma - \cos\alpha)$$
$$S_{33} = a^2b^2\sin\gamma \qquad S_{13} = ab^2c(\cos\gamma\cos\alpha - \cos\beta)$$

For a cubic unit cell the formula rewrites as

$$\frac{1}{d_{hkl}^2} = \frac{h^2 + k^2 + l^2}{a^2}$$

In this case, a family of planes {*h k l*} is characterized by equal interplanar distances. Each plane of the family gives rise to diffraction maxima at the same diffraction angle. Therefore, distortions of a cubic unit cell can be investigated from the diffraction peak positions measured for various planes of a {*h k l*} family.

## 2.5 Magnetic probe techniques

In the following, the techniques used to investigate the magnetic properties of the thin films are described. While superconducting quantum interference device-vibrating sample magnetometry offers a complete characterization of magnetic films (hysteresis curves, magnetic moment, coercive field, Curie temperature), the magnetic easy axis is identified faster by using the magneto-optical Kerr effect.

### 2.5.1 Superconducting quantum interference device-vibrating sample magnetometry

A very sensitive instrument for measuring magnetic properties of thin films, bulk or powder samples is the superconducting quantum interference device-vibrating sample magnetometer (SQUID-VSM) [113]. Its advantage lies in the two detection components: the VSM measuring technique and the sensitive SQUID convertor coupled as illustrated in *Figure 12*.

#### 2.5.1.1 Vibrating sample magnetometer

In a typical experiment, the magnetic sample is placed inside the superconducting detection coil designed as a second order gradiometer as shown in *Figure 12*. During the measurement, the sample vibrates with a selected amplitude and frequency in the applied magnetic field. A superconducting coil surrounding the gradiometer generates the magnetic field. A first order gradiometer surpasses a pick-up coil by canceling magnetic fields uniform in space due to the connection of identical parallel loops in series and with opposite directions [114]. Thus, the applied magnetic field is not detected by a first order gradiometer. Additional linear gradients in space of the applied magnetic field are detected by a first order gradiometer but canceled by the four turns of a second order gradiometer. A second order gradiometer behaves as two first order gradiometers placed in close proximity and contrariwise coupled. Linear gradients of a magnetic field are measured as equal quantities by each first order gradiometer and canceled due to the opposite coupling. However, local changes of the magnetic field created by the oscillating sample are measured by the center part of the second order gradiometer. According to Faraday’s law of induction, a time varying magnetic field creates an electric field through a coil. Therefore, vibrating the investigated sample at a selected frequency creates a time varying magnetic field. By limiting the vibration amplitude to the central region of the detection coil, the magnetic field generated by the sample is not canceled by the geometry of the second order gradiometer. The signal picked up by the detection coil is coupled inductively to the SQUID device.

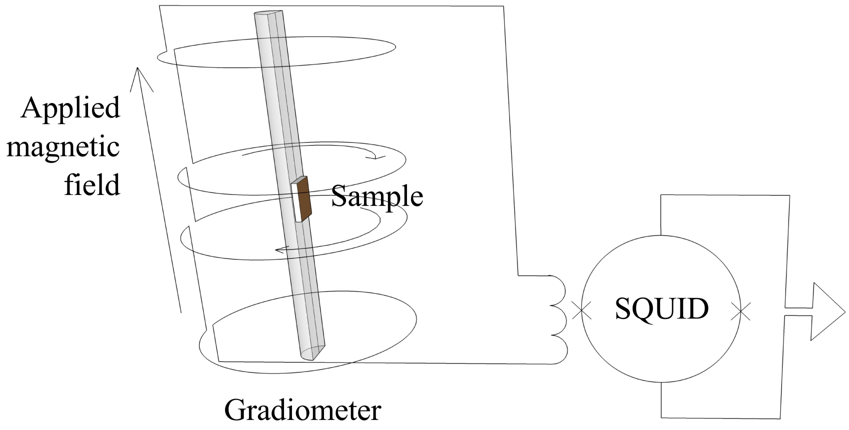

*Figure 12.* Sketch of a SQUID-VSM magnetometer. The sample, mounted in the in-plane configuration, vibrates in the applied magnetic field at the center of a second order gradiometer.

### 2.5.1.2 The Josephson junction

The proficiency of a SQUID device lies in the working principle of its main component, the Josephson junction, and the principle of flux quantization in a superconducting ring [113]. Two superconductors separated by a thin barrier (for example, an insulating layer, metal, semiconductor) allow a current flow across the barrier without a measured voltage (dc Josephson effect). For narrow barriers, the wave functions of Cooper pairs from the two superconductors overlap in the barrier region. By applying a current through the junction, Cooper pairs are accelerated and moved across the barrier. Due to the superconducting state of the two electrodes, no voltage drop is measured across the barrier.

A Josephson junction is composed of two superconductors separated by a thin barrier. For applied currents lower than a critical current $I_c$, that is junction dependent, Cooper pairs move from one electrode to the other one and no voltage is measured across the junction. However, for currents larger than $I_c$, the energy provided by the external source breaks up the Cooper pairs and normal electrons are produced. Their movement across the barrier gives rise to a resistive current. Thus, the junction becomes conductive and a voltage is measured. *Figure 13 (a)* shows the $I - V$ curve of a Josephson junction. The sensitivity of a SQUID device results from its operation on the $I - V$ curve around the $I_c$ region where small changes of the applied current produce large variations of the measured voltage.

### 2.5.1.3 Superconducting quantum interference device

A SQUID device is a superconducting ring interrupted by one or two Josephson junctions [113]. The higher sensitivity of the dc SQUID makes it widespread, thus, the discussion below focuses on this version. *Figure 13 (b)* shows the schematics of a SQUID with the two Josephson junctions marked with ‘1’ and ‘2’. A current $I$ is applied through the system and the voltage $V$ is measured as indicated. The two Josephson junctions are identical, so, the applied current splits in half through each junction. The applied current is fixed at a value slightly higher than $2I_c$, where $I_c$ is the critical current of one Josephson junction. Thus, the operating regime of a SQUID device lies on the steepest part of the $I-V$ curve shown in *Figure 13 (a)*. The magnetic field generated by a magnetic sample and detected by the gradiometer, similar to a SQUID-VSM measurement, is marked with $H_S$ in *Figure 13 (b)*.

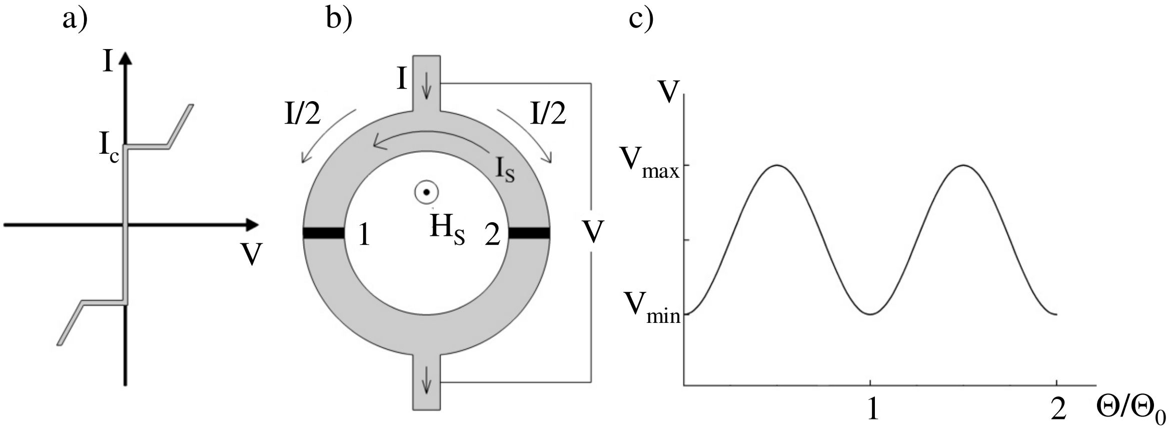

*Figure 13.* *a)* Ideal $I-V$ curve of a Josephson junction. *b)* Schematics of a dc SQUID. The nomenclature can be found in the text. *c)* Dependence of voltage drop $V$ across SQUID on the magnetic flux.

According to the flux quantization criterion in a superconductor, the magnetic flux $\Phi$ threading a superconducting ring is a multiple of flux quanta $\Phi_0$ as

$$\Phi = \frac{h}{2e} m = m\Phi_0$$

where $h$ is Planck's constant, $2e$ is the charge of a Cooper pair and $m$ is an integer number. Thus, if the magnetic flux $\Phi$ generated by the magnetic field $H_S$ is an integer multiple of flux quanta, no screening current is induced in the SQUID device and the measured voltage is $V_{min}$ (*Figure 13 (c)*). For a magnetic flux in the range $0 < \Phi < \frac{1}{2}\Phi_0$, a screening current $I_S$ is induced on the ring surface in order to fulfill the flux quantization criterion [115]. $I_S$ adds up to the current through one Josephson junction and, according to *Figure 13 (a)*, the measured voltage increases. The highest voltage $V_{max}$ is measured for $\Phi = \frac{1}{2}\Phi_0$. At this point, the largest $I_S$ is induced on the ring surface. For $\frac{1}{2}\Phi_0 < \Phi < \Phi_0$, $I_S$ changes direction and decreases in magnitude in order to further meet the quantization criterion. As a consequence, the measured voltage decreases. As the sample magnetization increases, a periodic variation of the voltage is measured, as showed in *Figure 13 (c)*. The value of the magnetic field (and magnetic moment) generated by the investigated sample is quantified by adding up the number of periods.

### *Experimental considerations*

#### *Correction of the magnetic field values*

In a SQUID-VSM device, the magnetic field $H_{\mathrm{appl}}$ applied at the sample position (*Figure 12*) is generated by passing a current through a type II superconductor designed as a cylinder enclosing the gradiometer and the sample. The value of the magnetic field reported by the device is not measured at the sample position, but it is given by the value of the current generating it. The device manufacturer draws attention to the presence of a magnet remanence after operating the superconductor in the high field regime leading to a discrepancy between the reported magnetic field and the real value at the sample position. Magnetic fields higher than $10^4$ Oe are larger than the first critical field of the superconducting material; therefore, magnetic field lines enter the superconductor. The magnetic field penetrating the superconductor generates at the sample position a magnetic field with an opposite orientation compared to $H_{\mathrm{appl}}$. Thus, the magnetic field experienced by the sample is lower than the reported value. The difference between the real and reported magnetic field depends on the magnet history. For example, for an applied magnetic field of $10^4$ Oe, a field difference of around -30 Oe is measured. Thus, reported magnetic fields of 30 Oe correspond to 0 Oe at the sample position. Accounting for this effect becomes relevant for soft magnetic materials. In this case a broad and reversed (negative coercivity) hysteresis loop is measured.

The correction of the magnetic field values is easily carried out. For this procedure a paramagnetic probe is measured with the same sequence as the one designed for the investigated sample. For a paramagnetic sample in small magnetic fields, the $M-H$ curve is a straight line passing through zero. Instead, as a result of the trapped magnetic field in the superconducting material, a hysteresis loop is observed for the reference sample. The corrected values of the magnetic field are given by the ratio between the measured magnetic moment and the slope fitting the hysteresis curve fixed to pass through zero.

During a SQUID-VSM measurement both film and substrate magnetic signals are detected. The steps involved in the separation of the film magnetic properties from the total signal are depicted in *Figure 14* for a 70 nm thick TmIG film grown on a sGGG(111) substrate. The substrate shows a strong paramagnetic behavior and it is the main component observed in the as-measured hysteresis loop (*Figure 14 (a)*). The substrate contribution is easily dismissed by fitting the high field region of the hysteresis curve with a linear function and subtract it from the measured data. *Figure 14 (b)* shows the magnetic properties of the 70 nm thick TmIG film. Nevertheless, the curve does not reflect a typical ferromagnetic behavior. The origin of the openings in the high field region is the remanent magnetic field of approximately -30 Oe within the device coils described above. With the corrected values for the magnetic field, the 70 nm thick layer exhibits the expected ferromagnetic behavior (*Figure 14 (c)*).

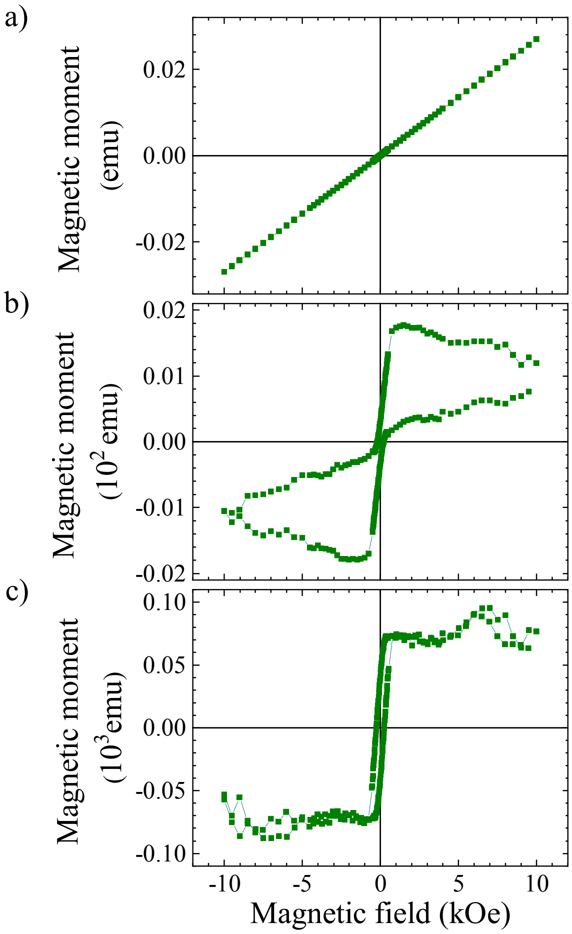

*Figure 14.* Illustration of the correction steps necessary for obtaining the film hysteresis loop: *a)* hysteresis loop of TmIG(70 nm)/sGGG, *b)* hysteresis loop after subtracting the substrate contribution, and *c)* hysteresis loop with corrected values of the magnetic field.

The effect of the device magnetic field history on the values of the corrected magnetic field is illustrated in *Figure 15*. YIG is known to show an extremely low coercive field (< 1 Oe) when grown on lattice-matching GGG substrates. Such low values require a proper correction of the magnetic field. *Figure 15* shows the in-plane hysteresis loops of a 33 nm thick YIG film after subtracting the substrate contribution. The correction field values used in the two cases were measured at different times. The arrows mark the sweeping field direction. While both loops indicate a ferromagnetic behavior with a low coercive field, the sweeping field direction points to the real curve. With reducing (increasing) the magnetic field from the maximum positive (negative) value, the magnetization in curve #1 switches direction at positive (negative) magnetic fields indicating a reversed hysteresis loop. Curve #2 shows the expected switching behavior. Additionally, the proper magnetic field values close the hysteresis loop for case #2. For very soft magnetic materials, a deviation of the magnetic field of around 2 Oe can lead to a wrong evaluation of the magnetic properties (for example: coercive field) as observed in *Figure 15*. The magnetic field trapped in the superconductor depends on the device history (highest applied magnetic field, quenching of the superconductor). Adjustments of the magnetic field values are necessary after such device operations.

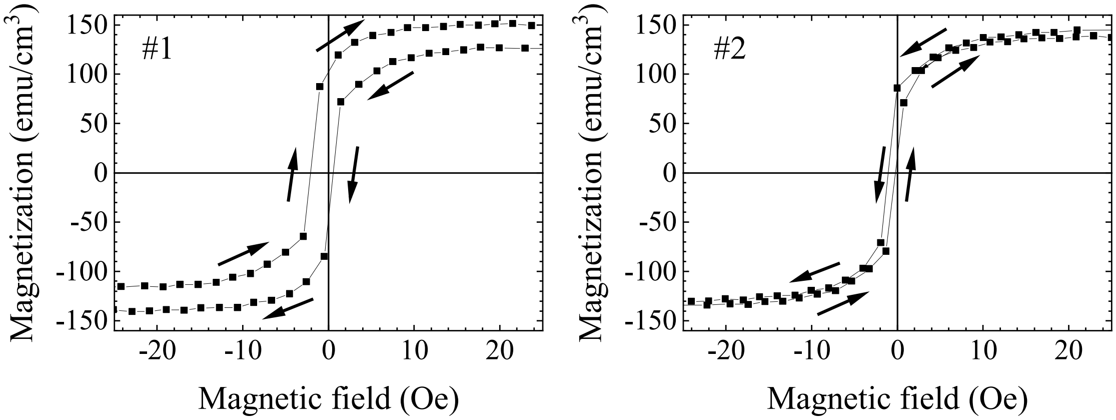

*Figure 15.* Impact of the device magnetic field history on the in-plane hysteresis loop of YIG(33 nm)/GGG. The arrows indicate the sweeping field direction.

*Films with weak magnetic signal*

The garnet substrates used in this work show a strong paramagnetic signal. In the example of *Figure 14* the substrate magnetic moment is three order of magnitude larger than the magnetic moment of the film. The strong substrate signal brings the SQUID-VSM device in a high measuring range corresponding to a low device sensitivity. Hence, in case of a weak film signal and large substrate contribution, the hysteresis loops become noisy after subtracting the substrate contribution (see *Figure 14 (c)* at fields higher than 5 kOe). This effect becomes more apparent when investigating thin or small iron garnet films, in which case, the extraction of the saturation magnetization can be hindered.

In a SQUID-VSM measurement the sample is mounted in various holders depending on the investigated magnetic properties: brass troughs or straws for the out-of-plane geometry, and quartz paddles for in-plane properties. Despite being magnetic (quartz is diamagnetic), in a SQUID-VSM measurement, the signal of the sample holder is not detected. Uniform holders are longer than the second order gradiometer. The magnetic signal generated by the vibrating holder during a measurement is detected but canceled by the four turns of the gradiometer. Thus, any magnetic signal extending over the gradiometer length is not measured. In fact, the centering procedure of the sample, carried out before a SQUID-VSM measurement, shows the extension of the signal generated by the vibrating sample up to 2 cm on both sides of the magnetic sample. However, experimentally it was observed that placing substrates (identical as type and size with the one used for the film growth) 6 cm on both sides of the investigated probe cancels the substrate signal. This procedure is easily carried out for in-plane holders and its effect is illustrated in *Figure 16* on the example of a 19 nm thick YIG film. A continuous area of substrates reduces the overall detected signal and the device measuring range (correlated with the device sensitivity) leading to smoother curves.

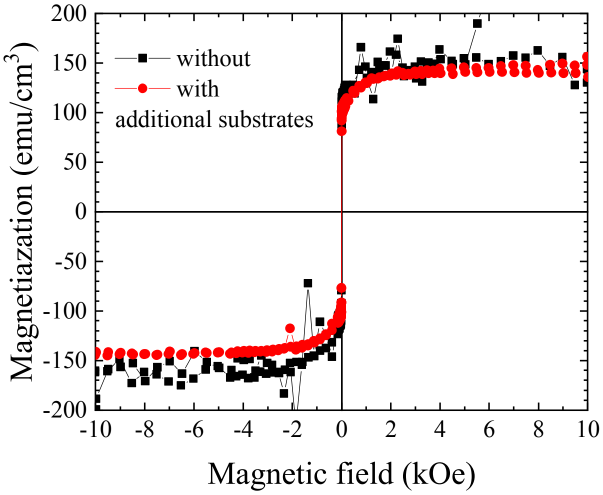

*Figure 16.* In-plane hysteresis loops of YIG(19 nm)/GGG measured with (red curve) and without (black curve) additional GGG substrates placed on both sides of the investigated sample on the quartz holder.

### 2.5.2 Magneto-optical Kerr effect

The magnetic state of a material influences the polarization of a propagating light wave. Varying the magnetic state, by means of an applied magnetic field, and monitoring the polarization state of the transmitted or reflected light is a fast and non-invasive method for the investigation of magnetic properties of thin films, for example easy axis of magnetization or coercivity. The magneto-optical effect measured in transmission geometry is known as Faraday effect, while in reflection, the effect is referred to as Kerr effect [116].

Three configurations of the magneto-optical Kerr effect (MOKE) are differentiated based on the relative orientation of the sample magnetization ***M*** and the plane of incidence of the light wave. In polar MOKE geometry, ***M*** is aligned out of the film plane. ***M*** parallel to the film surface and in the plane of incidence is known as the longitudinal configuration, while ***M*** perpendicular to the plane of incidence leads to the transverse Kerr effect. In this work, MOKE measurements in polar geometry were carried out.

In the following, the terminology of light polarization is introduced. The mathematical description of the effect using incoming light with a complex polarization state under oblique incidence is rather complicated; therefore, linearly polarized light at normal incidence is experimentally preferred. The interaction of light with matter, that gives rise to the Kerr effect, is described for the geometry of interest in this work.

The polarization state of a propagating light wave (described by the electric field ***E*** and magnetic induction ***B***) is given by the behavior of ***E*** with respect to the coordinate system and the propagation direction *z*. ***E*** vibrating in one direction defines the linearly polarized light. For circularly polarized light, ***E*** describes a circle when viewed in the propagation direction. Two cases are differentiated according to the rotation direction of ***E*** when viewed from the origin of the coordination system. Light waves with ***E*** rotating clockwise (counterclockwise) are right circularly polarized – short RCP (left circularly polarized – LCP). A linearly polarized light can be decomposed into two in-phase RCP and LCP light waves with equal amplitudes travelling with the same velocity. The most general case is the elliptically polarized light for which ***E*** describes an ellipse.

In the polar MOKE measurements carried out in this work, linearly polarized light shines on the investigated sample at normal incidence. The direction of ***E*** is adjusted by the polarizer placed in the optical path in front of the sample (*Figure 17*). After interacting with the sample, the light is reflected towards the detector made out of two photodiodes. A Wollastone prism placed in front of the detector separates the $x$ and $y$ intensity components of the reflected light. Light incident on a demagnetized sample does not change its polarization state. Light reflected by a demagnetized sample and reaching the Wollastone prism, rotated by 45 ° relative to the polarizer direction, is decomposed in $x$ and $y$ components with equal amplitudes. As a result, the two photodiodes detect similar signals. An applied magnetic field induces a magnetization in the sample. Light travelling through a magnetic medium changes its polarization state, and, thus, the amplitude of the $x$ and $y$ components. Different signals are detected by the two diodes when varying the sample magnetization. In this geometry, the ellipse properties, rotation and ellipticity (introduced below), are measured together and they are indistinguishable.

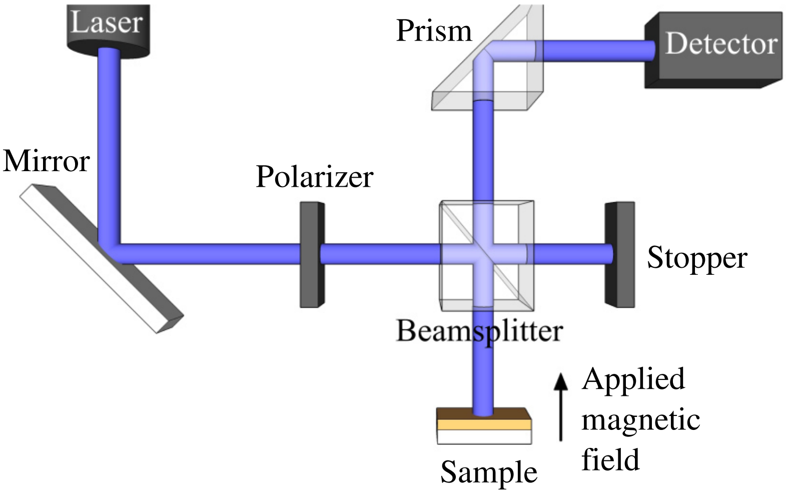

*Figure 17.* Schematics of the polar MOKE setup used in this work.

*Interaction of light with matter*

Light travelling through optically different media changes properties at the interface, for example wavelength, velocity or amplitude, due to refraction, absorption and reflection. The propagation of light across and away from the interface is described by the complex refractive index $N = n - \mathrm{i}k$ of the media. Light with wavelength $\lambda_0$ travelling in vacuum with velocity $c$ slows down and decreases in intensity when entering a material. The light velocity $s$ and wavelength $\lambda$ in the material are given by the refractive index $n$ as $s = c{\cdot}n^{-1}$ and $\lambda = \lambda_0{\cdot}n^{-1}$. Light entering a non-transparent medium is absorbed. The extinction coefficient $k = \frac{\lambda}{4\pi d}$ represents the reciprocal distance $d$ in which light intensity decrease to 1/e of its initial value.

The propagation of light (in the optical frequency range) through an anisotropic material is described by the dielectric tensor $\hat{\varepsilon}$. In polar geometry ($\boldsymbol{M} \parallel z$), $\hat{\varepsilon}$ has the form [117]

$$\hat{\varepsilon} = \begin{pmatrix} \varepsilon_0 & +i\varepsilon_1 & 0 \\ -i\varepsilon_1 & \varepsilon_0 & 0 \\ 0 & 0 & \varepsilon_0 \end{pmatrix} \tag{5.1}$$

The tensor elements are complex functions $\varepsilon_\mathrm{j} = \varepsilon_\mathrm{j}' + i\varepsilon_\mathrm{j}''$, with $j = 0$ or 1. The diagonal element $\varepsilon_0$ is related to $N$ as $\varepsilon_0 = N^2$. The off-diagonal element $\varepsilon_1$ shows a linear and/or a quadratic dependence on the sample magnetization $\boldsymbol{M}$, and it is this dependence that gives rise to the magneto-optical effects [118]. Considering an incident linearly polarized light, that can be decomposed into a right and left circular component, and following the report of Freiser [116], the complex refractive indices for RCP ($N_+$) and LCP ($N_-$) light are given by

$$N_\pm^2 = \varepsilon_0 \pm \varepsilon_1 \tag{5.2}$$

Thus, magnetic materials show different complex refractive indices for light waves with different circulations. RCP and LCP light waves entering a magnetic material acquire different wavelengths and velocities. The phase difference ($\phi = \phi_+ - \phi_-$) introduced between RCP (with phase $\phi_+$) and LCP (with phase $\phi_-$) lights transforms an initially linearly polarized light into an elliptically polarized wave after crossing a magnetic material. The ellipse is described by the rotation $\theta$, that is half of the phase difference $\phi$, and by the ellipticity $\eta$ introduced below.

Light travelling in air and reaching a thin film/substrate system undergoes optical reflection (forming the primary beam) and refraction at the air-film interface. Assuming a weak absorbing material, the refracted light propagates through the thin film and, at the film-substrate interface, similar optical phenomena take place. Light reflected at the film-substrate interface forms the secondary beam. The secondary beam propagates through the film and it escapes the system by refraction at the film-air interface. The primary beam, reflected at the air-film interface, and the secondary beam undergo optical interference. The amplitude of the outgoing light is proportional to the amplitude of the incident light. The proportionality factor, known as the amplitude reflection coefficient $r$, is a function of the complex refractive index of the material and the reflection and refraction angles at the two interfaces. According to eq. (5.2), different complex refractive indices for the two circular components of a linearly polarized light lead to different amplitude reflection coefficients ($r_+$ and $r_-$ for RCP and LCP light, respectively). An elliptically polarized light reflected by the thin film/substrate system is characterized by the ellipticity $\eta$ defined as [116]

$$\eta = -\frac{|r_+| - |r_-|}{|r_+| + |r_-|}$$

*Figure 18* shows the Kerr rotation spectrum of YIG(30 nm)/GGG in the energy range 1.5 – 5.0 eV measured in an in-plane magnetic field of 1.7 T. The spectrum was acquired in collaboration with M. Monecke (TU Chemnitz, Germany). The spectral features of YIG in this energy range originate from transitions between energy levels of $Fe_{oct}$ and $Fe_{tet}$, and excitations involving the Fe – O and $Fe_{oct} - Fe_{tet}$ sublattices [119–123]. Two laser sources ($\lambda = 405$ nm or 636 nm) are available for the home-built MOKE system sketched in *Figure 17*. Due to a larger optical activity at 3.06 eV, the MOKE hysteresis curves, discussed in the experimental part, were measured with the blue laser.

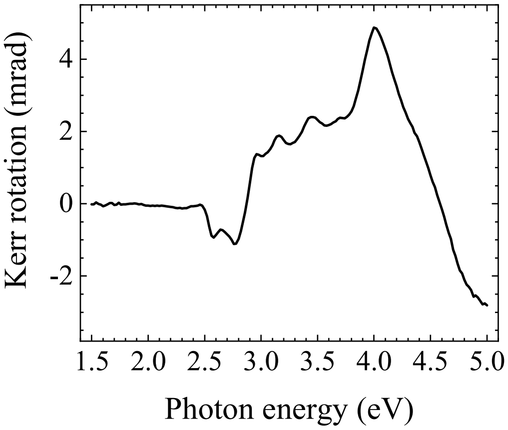

*Figure 18.* Kerr rotation spectrum of YIG(30 nm)/GGG measured in polar configuration. The film was saturated by applying an in-plane magnetic field of 1.7 T.

## 2.6 Ferromagnetic resonance

Another approach to extract the magnetic anisotropy of a magnetic sample is by ferromagnetic resonance (FMR) [124]. The Gilbert damping and ferromagnetic resonance linewidth are also identified from FMR measurements. First, the motion of magnetization in an applied magnetic field is presented, followed by the description of the experimental setup and conditions for the extraction of the aforementioned material properties.

*Motion of magnetization in an applied magnetic field*

A strong enough magnetic field $\boldsymbol{H}$ aligns the magnetization $\boldsymbol{M}$ along its direction. A change of the direction of $\boldsymbol{H}$ results in the change of the orientation of $\boldsymbol{M}$ that aligns along the new direction after the relaxation time $\tau$. The motion of $\boldsymbol{M}$, assuming a constant magnetization $M = |\boldsymbol{M}|$, is described by the equations

$$\frac{d\boldsymbol{M}}{dt} = \gamma(\boldsymbol{M} \times \boldsymbol{H}) - \frac{\lambda}{\gamma M^2}\boldsymbol{M} \times (\boldsymbol{M} \times \boldsymbol{H}) \qquad \text{Landau–Lifshitz} \qquad (6.1)$$

$$\frac{d\boldsymbol{M}}{dt} = \gamma(\boldsymbol{M} \times \boldsymbol{H}) - \frac{\alpha}{M}\boldsymbol{M} \times \frac{d\boldsymbol{M}}{dt} \qquad \text{Landau–Lifshitz–Gilbert} \qquad (6.1')$$

The magnetic field $\boldsymbol{H}$ exerts a torque, the first term of eq. (6.1), on the magnetization leading to the precession of $\boldsymbol{M}$ around the equilibrium direction. The second term describes a damping torque that after the time $\tau$ aligns $\boldsymbol{M}$ along $\boldsymbol{H}$. These two torques result in a damped precession of $\boldsymbol{M}$. $\gamma$ is the gyromagnetic ratio. For a particle of mass $m$ $\gamma = ge/2m$, where $e$ is the elementary charge and $g$ is the Landé factor. The Gilbert damping $\alpha$ describes the rate of magnetization relaxation and $1/\alpha$ gives approximately the number of rotations described by $\boldsymbol{M}$ before relaxation [65]. $\alpha$ is related to $\tau$ as $\tau = 1/(\alpha\omega)$, where $\omega$ is the precession frequency.

$\boldsymbol{H}$ is the total magnetic field experienced by $\boldsymbol{M}$. The internal magnetic field $\boldsymbol{H}_\mathrm{i}$ of a magnetic sample placed in the applied magnetic field $\boldsymbol{H}_\mathrm{ext}$ is $\boldsymbol{H}_\mathrm{i} = \boldsymbol{H}_\mathrm{ext} + \boldsymbol{H}_\mathrm{d} + \boldsymbol{H}_\mathrm{a}$, where $\boldsymbol{H}_\mathrm{d}$ and $\boldsymbol{H}_\mathrm{a}$ are the demagnetizing and the anisotropy fields, respectively. In this case, $\boldsymbol{H}$ in eq. (6.1) is replaced by $\boldsymbol{H}_\mathrm{i}$ and for known $\boldsymbol{H}_\mathrm{ext}$ and $\boldsymbol{H}_\mathrm{d}$ (given by the saturation magnetization) $\boldsymbol{H}_\mathrm{a}$ can be calculated as described below.

*Ferromagnetic resonance*

A common way to investigate magnetodynamic properties of ferromagnetic samples is the vector network analyzer (VNA)-based FMR technique [125]. In a VNA-based FMR experiment, the sample is positioned on a coplanar waveguide (CPW) structure. The CPW structure provides a radiofrequency (rf) excitation while two coils surrounding the sample produce a static magnetic field. The sample response to the external excitation is monitored via the VNA.

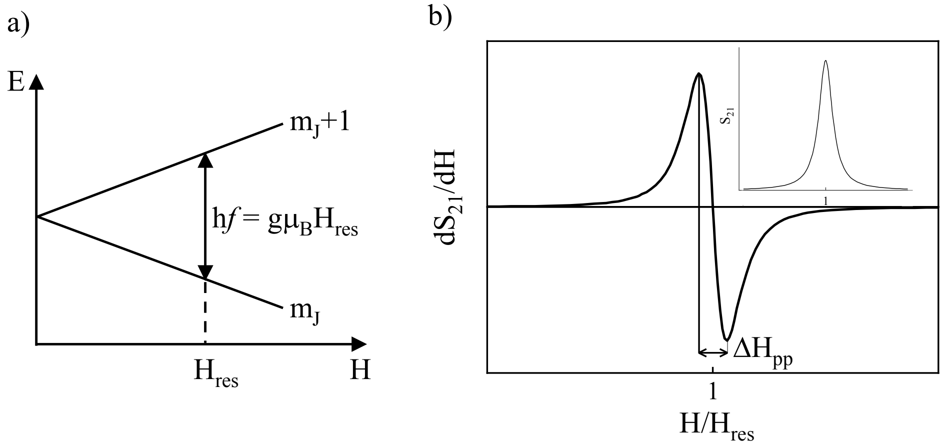

*Figure 19.* *a)* Splitting of energy levels $m_\mathrm{J}$ and $m_\mathrm{J}+1$ in the applied magnetic field $H$. $H_\mathrm{res}$ is the field at which a photon with frequency $f$ promotes the transition from $m_\mathrm{J}$ to $m_\mathrm{J}+1$. *b)* Derivative of sample absorption $S_{21}$ around $H_\mathrm{res}$.

The static magnetic field $\boldsymbol{H}$ saturates the sample magnetization $\boldsymbol{M}$. Its energy levels split due to the Zeeman effect, with the splitting between energy levels proportional to $H = |\boldsymbol{H}|$ (*Figure 19 (a)*). The application of an rf magnetic field $\boldsymbol{h}$ perpendicular to $\boldsymbol{H}$ drives the precession of $\boldsymbol{M}$ around $\boldsymbol{H}$ with the frequency $\omega = \gamma h$, $h = |\boldsymbol{h}|$. At a constant $\omega$, sweeping the static magnetic field results in a change of the splitting of the sample energy levels. At the resonant magnetic field $H_\mathrm{res}$, the energy of the rf radiation matches the energy difference between two energy levels, the transition is excited and the sample absorbs the rf radiation.

Thus, a detector monitoring the rf radiation reflected by the investigated sample, measures a drop in intensity when $H = H_{\mathrm{res}}$. FMR plots, representing the sample absorption $S_{21}$ (the inverse of the detected signal) as a function of applied magnetic field, show a maximum at $H_{\mathrm{res}}$ with a characteristic full width at half maximum $\Delta H_{\mathrm{pp}}$ (*Figure 19 (b)*). The resonance peak-to-peak linewidth $\Delta H_{\mathrm{pp}}$ shows a linear frequency dependence. Measuring $\Delta H_{\mathrm{pp}}$ at various $\omega$ and by fitting the dependence with

$$\Delta H_{\mathrm{pp}} = \Delta H_{\mathrm{inhom}} + \frac{2}{\sqrt{3}}\frac{\alpha}{\gamma}\omega \tag{6.2}$$

the Gilbert damping $\alpha$ and the inhomogeneity broadening $\Delta H_{\mathrm{inhom}}$ of magnetic properties are extracted.

As mentioned above, $\alpha$ and $\omega$ define the magnetization relaxation time $\tau$. Consequently, the Gilbert damping influences the propagation length or lifetime of spin waves, the smaller $\alpha$ is, the longer a spin wave propagates before attenuation. Intrinsic Gilbert damping originates from spin-orbit coupling [126]. For YIG, only the $\mathrm{Fe}^{3+}$ 3*d* electrons contribute to the magnetization and they couple weakly to the crystal lattice resulting in small $\alpha$.

The magnetic anisotropy is extracted from angular dependencies of the resonance field $H_{\mathrm{res}}$ measured at various frequencies. For this, polar (with respect to the sample normal and given by the angle $\theta$ with $\theta = 0°$ corresponding to the out-of-plane magnetic field direction) and azimuthal in-plane (denoted with $\varphi$) measurements are carried out. At $\theta = 0°$ and $\theta = 90°$, $H_{\mathrm{res}}$ $(w)$ can be fitted with the Kittel formulae:

$$\frac{\omega}{\gamma} = \mu_0 H_{res,\perp} - \left(\mu_0 M_{\mathrm{S}} - \frac{2K_{\mathrm{u}}}{M_{\mathrm{S}}}\right),\ \theta_H = 0^{\circ} \tag{6.3}$$

$$(\frac{\omega}{\gamma})^2 = \mu_0 H_{res,\parallel} \times \left(\mu_0 H_{res,\parallel} + \mu_0 M_{\mathrm{S}} - \frac{2K_{\mathrm{u}}}{M_{\mathrm{S}}}\right),\ \theta_H = 90^{\circ} \tag{6.4}$$

The formulae describe the correlation between rf frequency, resonance field in the two geometries, saturation magnetization $M_{\mathrm{S}} = |\boldsymbol{M}|$, and uniaxial anisotropy $K_{\mathrm{u}}$. Thus, FMR is a direct method to calculate $K_{\mathrm{u}}$ using $M_{\mathrm{S}}$ evaluated from other techniques, for example from SQUID-VSM measurements [127].

# 3 Optimization of the growth conditions

The growth of single crystal films by PLD at elevated temperatures requires the identification of the balance between the energy of the plume particles incident on the substrate (given by laser pulse energy and rate, and background pressure) and the substrate temperature. Additionally, the chamber pressure during deposition influences the amount of chemical elements reaching the substrate surface and, thus, the film stoichiometry. Therefore, ahead of any investigation, the optimization of growth conditions is carried out. The growth rate (amount of material deposited per second), substrate temperature, and gas pressure resulting in stoichiometric films with smooth surface and the sought crystal structure are first identified.

In this work two key garnet materials were investigated. $Tm_3Fe_5O_{12}$ (TmIG) and $Y_3Fe_5O_{12}$ (YIG) thin films were grown by PLD using a Lambda LPX 300 laser (pulse duration: 20 ns, wavelength: 248 nm) or a Coherent COMPex 205 F laser (pulse duration: 25 ns, wavelength: 248 nm). TmIG films were prepared from a commercially available polycrystalline TmIG target (G-Materials, purity 99.99 %). YIG films were deposited from self-prepared polycrystalline targets. The YIG targets were prepared from $Fe_2O_3$ and $Y_2O_3$ powders (Chempur, purity 99.9 %). Due to a higher scattering probability of Fe ions during deposition, compared to Y ions, a higher content of $Fe_2O_3$ powder was added to the mixture leading to a Y/Fe ratio of (2.6 – 2.85)/(5.15 – 5.4). The powders were mixed in a marble mortar for 40 minutes. Isopropanol was repeatedly added to facilitate the mixing process. The 1 cm diameter pressed target was sintered in ambient atmosphere at 1200 °C for 15 hours. Prior to the depositions, the targets were cleaned under vacuum ($10^{-6}$ mbar) with $>10^4$ laser pulses. In the PLD chamber, the substrate is mounted approximately 4 cm in front of the target and the substrate temperature is monitored via a thermocouple placed in the sample holder.

## 3.1 Stoichiometry

For a fixed target composition, the growth parameter with the highest impact on the film stoichiometry is the chamber pressure during deposition. Studies on oxygen incorporation in $Bi_2Sr_2Ca_1Cu_2O_8$ films prepared by PLD showed that almost half of the oxygen is incorporated from the ambient gas [128]. Thus, the films investigated in this work were grown in an oxygen atmosphere.

In order to identify the oxygen pressure at which films with uniform thickness show the stoichiometric rare-earth/Fe ratio, TmIG and YIG films were prepared on $1.5 \times 1.5$ cm$^2$ silicon substrates at 650 – 670 °C while the oxygen pressure was varied between $5 \cdot 10^{-4}$ and 0.4 mbar. After deposition, each sample was cut using a diamond pen and only the area of uniform thickness was used for further analysis.

The film stoichiometry was evaluated by Rutherford backscattering spectroscopy (RBS) or from energy dispersive X-ray fluorescence (EDXRF) measurements carried out in ambient atmosphere. For these studies, silicon substrates instead of substrates with lattice-matching structure, for example garnet substrates, were chosen in order to extract reliable values for the composition. In case of gadolinium and gallium based substrates, the chemical elements of the film and substrate generate overlapping peaks in the RBS spectra due to the small atomic mass difference between Fe and Ga, and Tm or Y and Gd. Additionally, Fe, Tm, and Gd have X-ray emission lines in close proximity (between 6.0 and 8.5 keV) and the strong substrate signal could cover the film emission lines in an EDXRF spectrum.

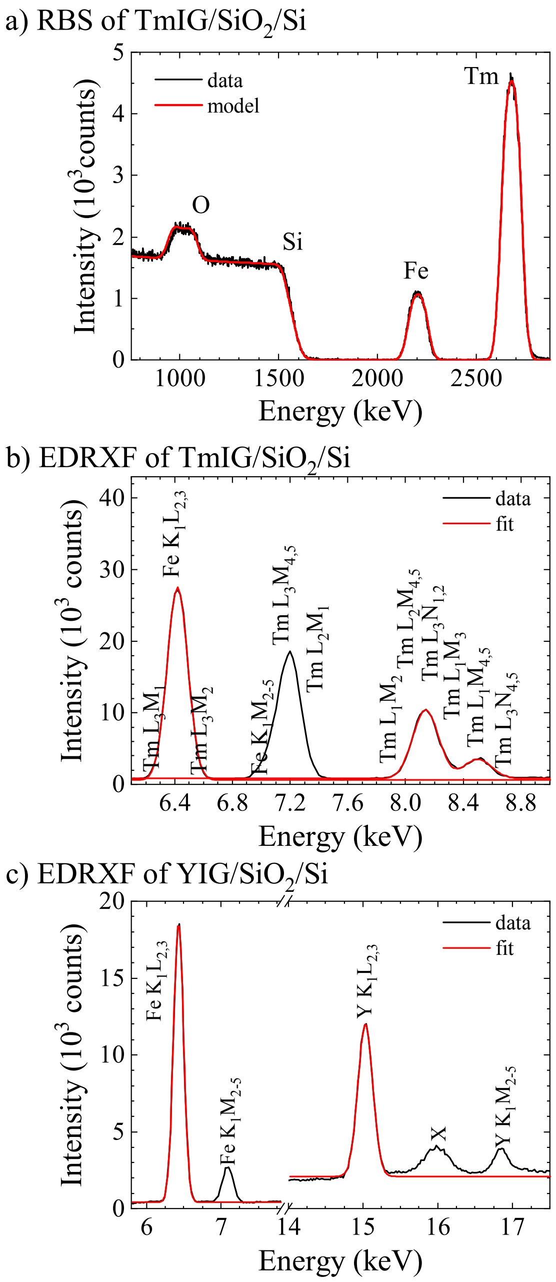

*Figure 20.* *a)* RBS spectrum of TmIG/SiO$_2$/Si. EDXRF spectra of *b)* TmIG/SiO$_2$/Si and *c)* YIG/SiO$_2$/Si. In each measurement the chemical elements giving rise to the visible peaks are indicated.

As an example, *Figure 20* shows the RBS spectrum of TmIG/$SiO_2$/Si and the EDXRF measurements of TmIG/$SiO_2$/Si and YIG/$SiO_2$/Si. In each spectrum, the visible peaks are labeled. The origin of the peak marked with X in *Figure 20 (c)* is discussed at the end of this chapter.

In the RBS measurement of *Figure 20 (a)*, the black and red curves represent the experimental data and fitting model, respectively. The Tm and Fe peaks are well separated and no diffusion is observed between the film and the substrate. The atomic concentration and film thickness were obtained by fitting the experimental data with a model using the SIMNRA program [129]. The fitting model consists of three layers: the top layer is represented by the TmIG film of unknown thickness and composition, the second layer is the 100 nm thick $SiO_2$ layer, and silicon is the bottom layer. For all samples the fitting sequence was carried out until the simulated spectra have the quality ($\chi^2 = 5.1$) shown in *Figure 20 (a)*. Please note that according to Ref. [129] $\chi^2$ values below 5 reflect an acceptable agreement between measurement and fit.

*Figure 20 (b)* and (*c*) show the EDXRF spectra of TmIG and YIG films with a focus on the Fe and Tm, and Fe and Y emission lines, respectively. All emission lines in this energy range are labeled according to the IUPAC notation (see chapter 2.3.2). In the following, the Tm peak centered around 8.12 keV is referred to as $L_2M_4$ according to the strongest emission line, however, all displayed contributions are contained. For the stoichiometry evaluation of TmIG films, the areas $A$ of the Fe $K_1L_{2,3}$ and Tm $L_2M_4$ peaks were used since they show little (for Fe) or no (for Tm) overlap with the emission lines of other chemical elements present in the sample. For the YIG films, the Fe $K_1L_{2,3}$ and Y $K_1L_{2,3}$ peaks were selected. The Gauss fits of the Fe, Tm, and Y peaks carried out to evaluate $A$ are also included in *Figure 20 (b)* and (*c*). The contribution of Tm $L_3N_{4,5}$ was taken into account for a proper evaluation of the Tm $L_2M_4$ peak. Six films of known stoichiometry (extracted from RBS measurements) were used to identify the average conversion factor $x$ between the ratio of areas $A$(rare-earth)/$A$(Fe) and the ratio of rare-earth/Fe. The Tm/Fe and Y/Fe ratios were obtained by multiplying $A$(rare-earth)/$A$(Fe) with the conversion factor $x$.

*Figure 21* displays the dependence of the film stoichiometry on the oxygen pressure, evaluated from EDXRF measurements, for the example of TmIG/$SiO_2$(100 nm)/Si grown at 660 – 670 °C using the Coherent COMPex 205 F laser. The horizontal line marks the stoichiometric value of 0.6. The error bar is mainly given by the uncertainty of the conversion factor $x$. Within the considered range, the oxygen pressure ($pO_2$) influences strongly the Tm/Fe ratio. The film deposited at the lowest $pO_2$ of $5 \cdot 10^{-4}$ mbar shows an almost stoichiometric Tm/Fe ratio of $0.61 \pm 0.02$. Stoichiometric TmIG films were grown at 0.04 mbar oxygen pressure using the Lambda LPX 300 laser. Increasing $pO_2$ leads to Tm-rich films as Fe ions are scattered more by the background gas compared to Tm ions. A similar dependence was observed for the YIG films. Depending on the target stoichiometry and the laser type, the stoichiometric Y/Fe ratio was obtained for films grown at 0.03 mbar and $5 \cdot 10^{-3}$ mbar oxygen pressure. The background pressure leading to stoichiometric films depends on the target composition. As a result, typical oxygen pressure values varying in a broad range (0.02 – 1.06 mbar [30,47,49,54,55]) are reported in literature for the growth of TmIG and YIG films.

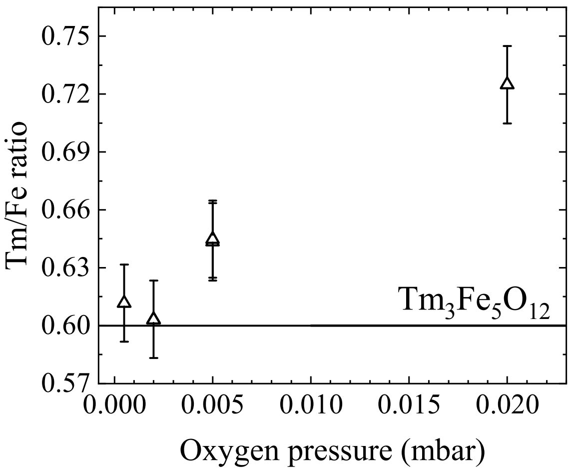

*Figure 21.* Dependence of the Tm/Fe ratio on the oxygen pressure during deposition at 660 – 670 °C substrate temperature.

From the RBS analysis, the film thickness and deposition rate were extracted simultaneously with the chemical composition. For the films investigated by EDXRF, spectroscopic ellipsometry measurements were carried out to identify the film thickness. In this case, a YIG and a TmIG film of known thickness (extracted from RBS measurements) were used to build models in the V.A.S.E. program by J.A. Woollam Co.. Ellipsometry spectra of films with unknown thickness measured at three incident angles were fitted with these models. Iron garnet films are commonly grown at deposition rates of 0.01 – 0.5 nm/s [130–132] , but values as low as 0.004 nm/s are also reported [30]. For both targets, the laser pulse energy and rate were adjusted to correspond to deposition rates below 0.03 nm/s.

The peak centered at 15.95 keV in *Figure 20 (c)* (labeled X from now on) corresponds to no standard emission line of the chemical elements from Li to Pu in the database of the PCEDX program. In order to identify its origin, EDXRF spectra of YIG/$SiO_2$/Si, a silicon, and an $Al_2O_3$ single crystal substrate were measured with and without an aluminum filter placed between the X-ray source and the sample.

For no filter in the X-ray path, the spectrum of YIG/$SiO_2$/Si contains emission lines from all chemical elements present in the sample: Si from the substrate, Y and Fe from the film, Rh from the source, and Ag from the paste used to fix the substrate on the sample holder (*Figure 22*). The high energy range displaying the Ag emission lines was cut to favor visibility. The presence of the X emission line for both YIG film on a silicon substrate and for a bare substrate without silver paste on the back side indicates that the X emission line originates from the substrate or the X-ray source. The placement of the Al filter in the beam path, with an active energy range from 2 to 5 keV, leads to the expected strong reduction of the Si peak with no intensity change of the X peak. Thus, the X peak is not a sum or an escape peak generated by the Si emission line. The spectrum of a sapphire substrate shows one peak at 16.8 keV, additionally to the Al emission line. The peak matches the position of Y $K_1M_{2\text{-}5}$, however, the more intense Y $K_1L_{2,3}$ is missing. Spectra of both silicon and sapphire substrates contain non-standard emission lines at different energies. Therefore, these emission lines originate from the substrates and not from the Rh source. All substrates investigated here are single crystal substrates. The possibility that the configuration of the source and the detector satisfies the Bragg's law should be verified on polycrystalline and amorphous samples.

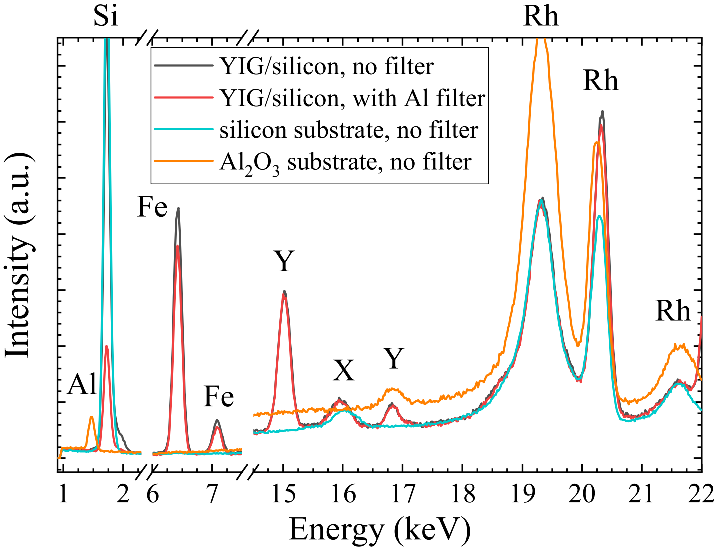

*Figure 22*. EDXRF spectra of YIG/$SiO_2$/Si, a silicon, and a sapphire single crystal substrates measured with or without an Al filter. The chemical elements giving rise to the observed emission lines are indicated.

## 3.2 Growth temperature

The energies involved in the growth process (energy of the plume species and substrate temperature) and the rate at which particles reach the substrate influence the film crystallinity and morphology. The parameters that define the energy of the plume species reaching the substrate surface are laser pulse energy, chamber pressure, and target to substrate distance. Considering fixed the target to substrate distance and the optimal background pressure, the balance between the laser pulse energy, the rate at which particles reach the substrate, and the growth temperature needs to be identified. In the following, the optimization of the growth conditions is exemplified for TmIG films deposited on GSGG(111) substrates, however, similar steps were carried out for YIG films.

12 – 16 nm thick TmIG films were deposited on GSGG(111) substrates at the optimum oxygen pressure. The additional growth conditions are summarized in *Table 2*. The laser pulse energy hitting the target depends on the cleanliness of the optical path. This drawback was compensated by monitoring the amount of material deposited per second (referred here as deposition rate) and adjusting the laser pulse energy to achieve the desired deposition rate. Throughout this work, values of the deposition rate are given instead of laser pulse energy and rate. The growth temperature was monitored via a thermocouple fixed in the sample holder. For a good thermal contact with the sample holder during deposition, the back side and the edges of the substrates

were covered with silver paste. After deposition, each sample was cooled down in the same atmosphere with -5 °C/min. The growth conditions were optimized according to the film morphological, structural and magnetic properties.

*Table 2*. Growth conditions of various TmIG films on GSGG(111) substrates. The surface roughness values were extracted from 2 × 2 μm$^2$ AFM images.

| Sample name | Growth temperature (°C) | Deposition rate (nm/s) | | Surface roughness (nm) | |
|---|---|---|---|---|---|
| #1 | 675 | 0.01 | ± 0.005 | 2.6 | ± 0.3 |
| #2 | 650 | 0.01 | | 0.4 | ± 0.1 |
| #3 | 625 | 0.005 | | 0.3 | |
| #4 | 600 | 0.01 | | 0.8 | |

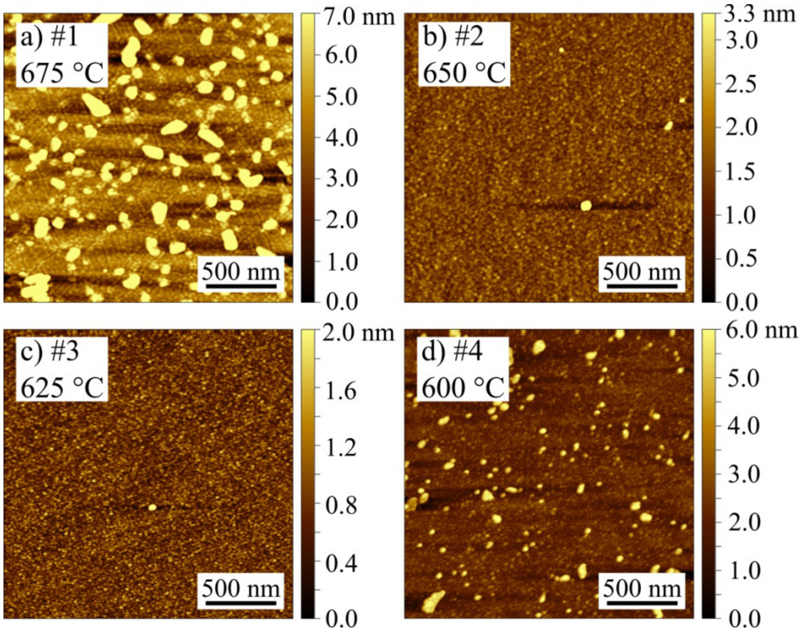

*Figure 23*. Topography images of TmIG films #1 – #4 prepared at the conditions summarized in *Table 2*. Different scales are used for a better visibility of specific features.

First, the impact of the growth conditions on the surface morphology was investigated by AFM. *Figure 23* shows the topography images of samples #1 – #4 while the values of the root mean square (rms) surface roughness, extracted from the scanned window, are included in *Table 2*. Film #1, grown at the highest temperature of 675 °C, shows cracks across the entire measured window. An enlarged image of film #1 is displayed in *Figure 24*. Quindeau et al. [55] reported for epitaxial TmIG films on GGG a thermal expansion coefficient $\alpha_L$ in the growth direction of $15.57 \cdot 10^{-6}$ K$^{-1}$ which is larger than $\alpha_L$ of GSGG of $7.32 \cdot 10^{-6}$ K$^{-1}$, ref. [133]. Therefore, upon cooling, the film develops biaxial in-plane tensile strain in the range of $5.5 \cdot 10^{-3}$. The cracks have a 3-fold in-plane symmetry which might correspond to the [1-10], [0-11] and [-101] crystal directions. The small lateral size of the grooves limits the microscope depth resolution.

According to *Figure 23 (a)*, the grooves are 0.5 nm deep, however, they might extend through the entire film thickness. The large value of the rms roughness originates from droplets (10 nm high and 800 nm wide) distributed on the film surface. Reducing the growth temperature to 625 °C results in a strong decrease of the surface roughness down to 0.3 ± 0.1 nm. Film #4 prepared at 600 °C shows droplets on the surface similar to film #1. In both cases, they might originate from a temporally increased roughness of the target. Areas of film #4 not covered with droplets are characterized by an rms roughness of 0.3 ± 0.1 nm.

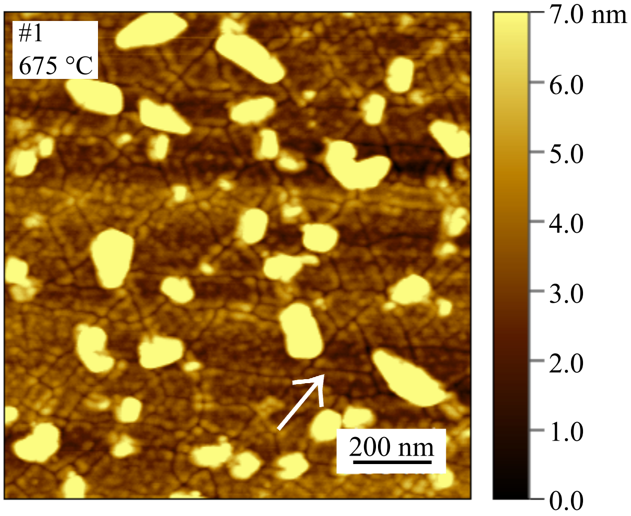

*Figure 24.* Enlarged topography image of the TmIG grown at 675 °C substrate temperature.

Next, the structural properties were investigated since the growth temperature, the parameter that promotes the film crystallization, must be above the crystallization temperature. *Figure 25 (a)* shows the XRD $\theta - 2\theta$ scans of all samples measured around the substrate GSGG (444) reflection peak. Before each measurement, the substrate [444] direction was aligned with the goniometer axis. The diffraction pattern of a bare substrate is displayed for comparison and the position of the diffraction angle corresponding to bulk TmIG (444) plane is marked with a vertical line. The substrate shows the splitting of the main (444) reflection due to contributions from Cu K$\alpha_1$, K$\alpha_2$, and K$\alpha_{3,4}$ radiations [134,135], which are sometimes misinterpreted in literature [136].

Samples prepared at temperatures between 600 °C and 650 °C display a diffraction peak corresponding to the TmIG (444) plane, thus, all growth temperatures ensure the film crystallization. No differences of the crystal structure are apparent for films grown at these temperatures. Films #2 – #4 have the (444) diffraction peak at $2\theta$ angles larger than for bulk TmIG, which indicates a compressed lattice in the growth direction. This compression should result in an expanded lattice in the film plane inducing tensile strain, the required condition for obtaining an out-of-plane magnetoelastic anisotropy contribution. In this geometry, the film peak of sample #1 can hardly be identified. The crystalline nature of sample #1 and #3 was investigated in a broad angle range (20 – 80°) without carrying an alignment to any substrate peak. For a better visibility, the diffractograms in the 44 – 54° range are shown in *Figure 25 (b)*. The scans contain the substrate (444) reflection peak corresponding to various wavelengths of the incident beam. For both samples, the film (444) diffraction peak is centered at around $2\theta = 51.55$ °. The absence of additional peaks in this angle range indicates a textured growth. The diffraction peak of a film epitaxial to the substrate decreases in intensity in a misaligned geometrical configuration similar to the substrate reflection. The geometrical misalignment of sample #3 results in a $10^4$ times reduction of the substrate peak intensity while only a 20 times decrease is observed for the film peak. The lower reduction of the film peak intensity is a signature of film mosaicity. For sample #1, a rather intense film peak is observed in the misaligned configuration indicating a larger film mosaicity probably induced by the cracks visible on the film surface.

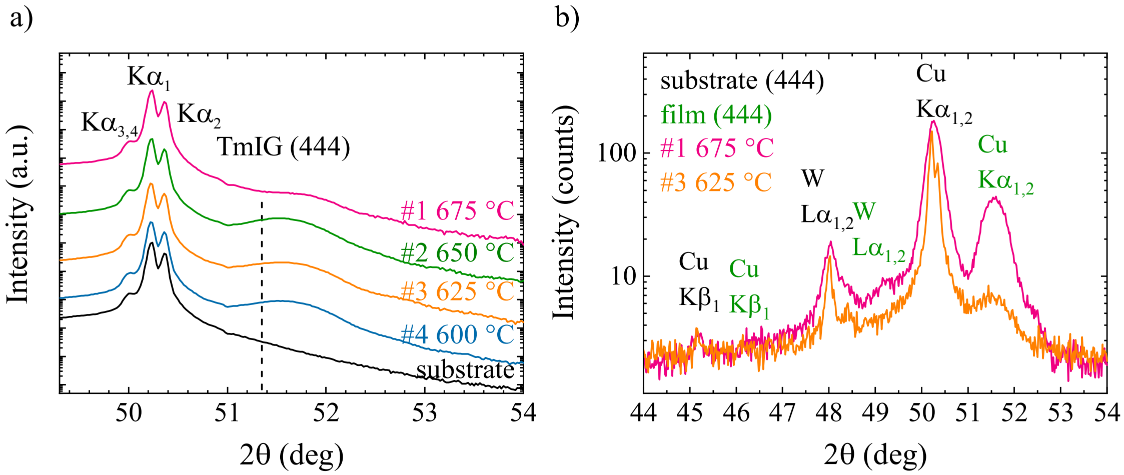

*Figure 25.* *a)* Diffraction patterns of TmIG films #1 – #4 measured after the alignment to the substrate (444) reflection. The scan of a bare substrate is displayed for comparison. The diffractograms are shifted on the *y* axis for a better visibility. The dashed line marks the position of bulk TmIG (444) reflection. *b)* Diffractograms of sample #1 and #3 acquired without carrying out any system alignment.

The magnetic easy axis was identified from MOKE hysteresis curves that require no sample preparation. The saturation magnetization $M_S$ and coercive field $H_c$ were extracted from SQUID-VSM measurements. Before the SQUID-VSM measurements, the samples were cut using a diamond saw and the back side was polished with sand paper in order to remove the silver paste used for fixing the substrate on the sample holder. All magnetic investigations were carried out at room temperature.

MOKE hysteresis loops measured in polar geometry (the external field is applied out of the sample plane) are displayed in *Figure 26 (a)*. The reverse direction of the hysteresis loops (negative $M_S$ at maximum positive external field) originates from the negative Kerr rotation at the used laser wavelength (see *Figure 18*). All films are magnetic and the squared shape of the curves indicates that the easy axis of magnetization points out of the sample plane. The contributing magnetic anisotropies and their role in influencing the magnetic easy axis direction are discussed thoroughly in chapter 5.1.2. Shortly, the magnetoelastic anisotropy induced by in-plane tensile strain, that orients the magnetization $\boldsymbol{M}$ normal to the sample plane, competes with and overcomes the shape anisotropy orienting $\boldsymbol{M}$ in the sample plane (see chapter 1.5 for a discussion on various sources of magnetic anisotropy). The crystallographic analysis reveals similar properties for films #2 – #4. The presence of the film (444) diffraction peak at the same $2\theta$ angle indicates a constant level of in-plane tensile strain for these films. However, film #4 shows the highest magnetic remanence. Considering a similar tensile strain, a tilt of the magnetic easy axis away from the normal direction for films #2 and #3 could correspond to a slightly larger saturation magnetization $M_S$, and thus, a stronger shape anisotropy $K_s$ ($K_s = -2\pi M_S^2$).

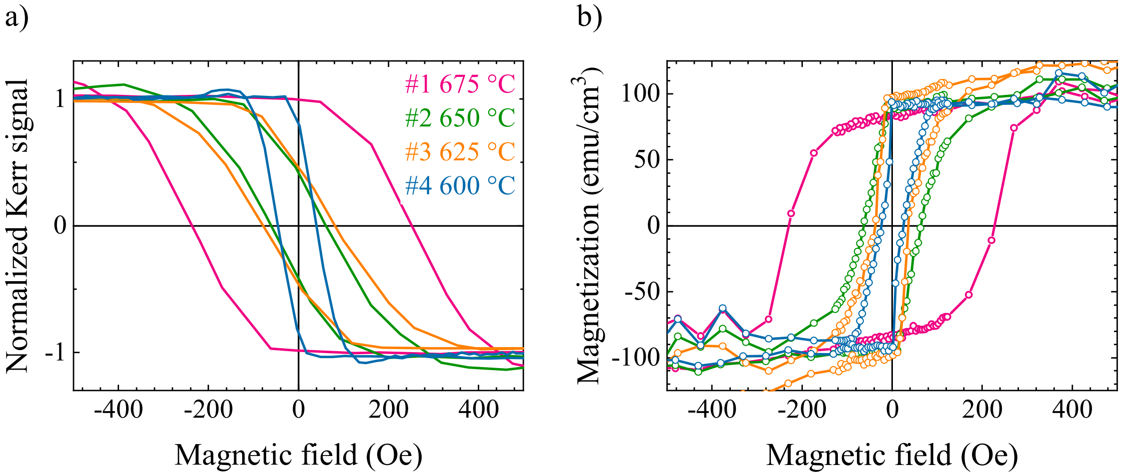

*Figure 26.* Magnetic characterization of TmIG films #1 – #4. *a)* Normalized polar MOKE hysteresis curves. *b)* Out-of-plane SQUID-VSM measurements after subtracting the substrate signal.

*Figure 26 (b)* displays the out-of-plane (oop) SQUID-VSM hysteresis loops of the films after subtracting the substrate paramagnetic signal and correcting the values of the magnetic field. The measurements confirm the direction of the magnetic easy axis, and show the strong effect of the growth conditions on the coercive field $H_c$ (the magnetic field at which $M = 0$ emu/cm$^3$). The film deposited at the highest substrate temperature shows the highest coercivity of 230 ± 20 Oe. A strong reduction of $H_c$ is visible with decreasing the growth temperature and deposition rate. The lowest value of 24 ± 4 Oe is measured for the film prepared at 600 °C. The droplets observed on the surface of film #4 seem not to affect its magnetic properties. The flipping of magnetization when cycling the applied magnetic field takes place via nucleation and propagation of magnetic domains. Defects act as pinning centers for the propagation of magnetic domains. Therefore, a decrease of defect density leads to the observed reduction of $H_c$. Based on the level of compression in the growth direction for films #2 – #4, a similar magnetic behavior is expected for these samples. Indeed, no difference in the direction of the magnetic easy axis for films #2 – #4 is apparent from *Figure 26 (b)*.

At positive saturation, the magnetization $\boldsymbol{M}$ of the film aligns to the applied magnetic field $\boldsymbol{H}_{ext}$ direction (referred here as positive direction). With decreasing $H_{ext}$, film #4 (grown at 600 °C) maintains the direction of $\boldsymbol{M}$ indicated by an almost 100% remanence at $H_{ext} = 0$ Oe. Negative magnetic fields nucleate magnetic domains with an opposite ***M*** direction (***M*** in the negative direction). The sharp decrease of the magnetization towards maximum negative value corresponds to fast propagating domains with ***M*** in the negative direction. On the contrary, for film #1 (grown at 675 °C), a slow decreasing magnetization is observed at negative magnetic fields when coming from positive saturation. The cracks visible on the film surface (*Figure 24*) limit the propagation of magnetic domains with ***M*** in the negative direction. In this case, the rotation of ***M*** is achieved via the nucleation of a large number of magnetic domains.

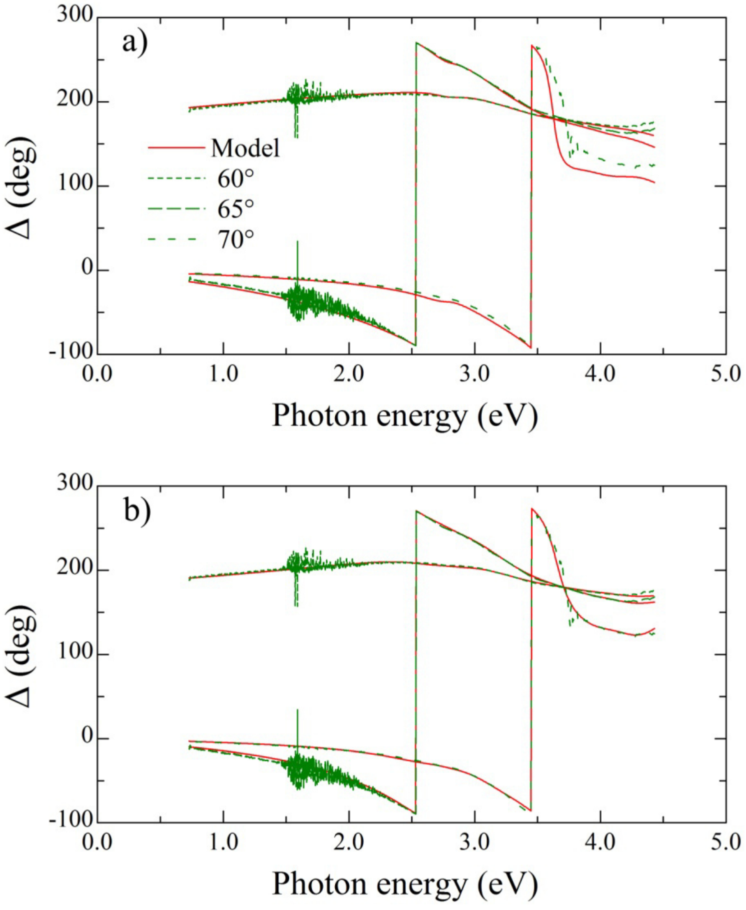

*Figure 27.* Ellipsometry spectra of the TmIG film deposited at 625 °C measured at three angles of incidence and modeled with *a)* the YIG dielectric function and *b)* a modified dielectric function.

All films show a saturation magnetization $M_S$ of 100 ± 25 emu/cm$^3$, close to the bulk value of 110 emu/cm$^3$. The large error bar originates from the uncertainty of the film thickness. The thickness of TmIG films was evaluated by spectroscopic ellipsometry. The dielectric functions of TmIG and GSGG, necessary for building the fitting model, are not reported in literature. Instead, the dielectric functions of YIG and GGG reported by Jakubisova-Liskova et al. [137,138] were used. *Figure 27 (a)* shows the ellipsometry spectra of film #3 measured at three angles of incidence. Using the YIG dielectric function, a film thickness of 12 ± 3 nm and a fit that matches well the measurement in the low energy range (below 3.5 eV) are obtained. In this case, the oscillators used to build the model were fixed during fitting and only the film thickness was set free. The addition of one spectral feature and setting free the amplitude, position and broadness of all oscillators during fitting result in the modified dielectric function displayed in *Figure 28*. Compared to the dielectric function of YIG, the imaginary part of the dielectric function obtained from the modified model is larger in the 2.3 – 3.1 eV and 3.5 – 4.3 eV photon energy ranges. Using the modified model, a film thickness of 11 ± 3 nm is obtained. The oscillators building the fitting model represent allowed optical transitions within a material. Therefore, their parameters (position, amplitude, broadness) are identified from energy level diagrams. However, such a diagram is not reported in literature for $Tm_3Fe_5O_{12}$. Nevertheless, chemical and structural differences between the TmIG films and a YIG crystal could lead to the changes observed in *Figure 28*. Considering the small differences between the imaginary parts of the two dielectric functions displayed in *Figure 28*, and the uncertainty regarding the accuracy of the modified model, further evaluations of thickness of TmIG films were carried out using the YIG dielectric function. Nevertheless, an error bar of 3 nm should be considered for the calculation of $M_S$.

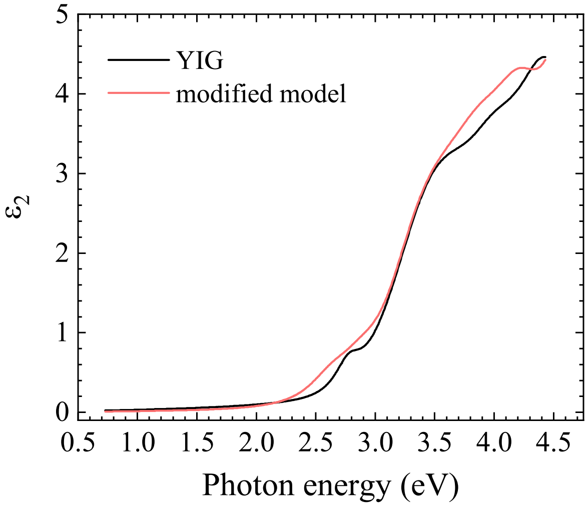

*Figure 28*. Imaginary part $\varepsilon_2$ of the dielectric function of YIG and of a modified model.

Based on the analysis of surface quality, stoichiometry, and structural and magnetic properties, the optimal growth conditions of TmIG films on GSGG(111) substrates were identified to be $5 \cdot 10^{-4}$ mbar oxygen pressure, 0.01 nm/s deposition rate, and 600 °C growth temperature.

## 3.3 Cooling rate

Few works on iron garnet films deposited at elevated temperatures report the cooling rates with typical values between -2 °C/min and -10 °C/min [45,55]. The influence of the cooling rate on the structural and magnetic properties of TmIG films was investigated. For this, three 70 nm thick films were prepared at optimal growth conditions (0.04 mbar oxygen pressure, 615 °C substrate temperature, 0.03 nm/s deposition rate) on sGGG(111) substrates. After deposition the samples were cooled in the same atmosphere with -13 °C/min, -5 °C/min, and -2 °C/min down to 200 °C. At 200 °C, the power supply of the heater was turned off.

*Figure 29 (a)* shows the XRD $\theta - 2\theta$ patterns of the three samples and a bare substrate measured around the sGGG (444) reflection peak. The diffraction angle corresponding to bulk TmIG (444) plane is marked with a vertical line. All films show the TmIG (444) reflection peak at a $2\theta$ angle larger than for bulk TmIG indicating a compressed unit cell in the growth direction. Within the range considered here, the cooling rate shows only a small impact on the crystal structure. By reducing the cooling rate from -13 °C/min to -5 °C/min the film (444) reflection shifts towards smaller diffraction angles by 0.07 °. No additional structural changes are observed by lowering further the cooling rate to -2 °C/min. Therefore, the impact of the cooling speed on the crystal structure is of minor importance.

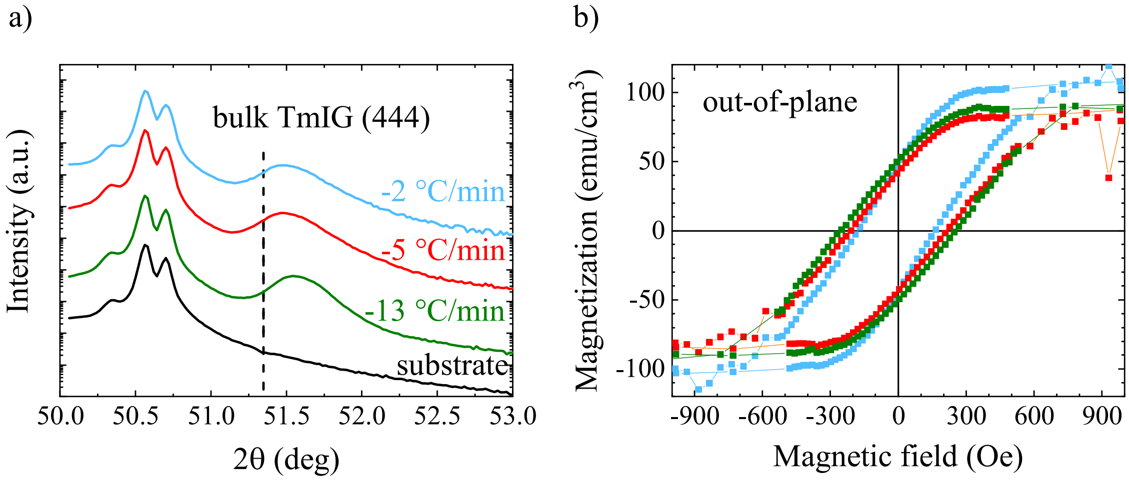

*Figure 29.* Impact of the cooling rate after deposition on the *a)* structural and *b)* magnetic properties of TmIG(70 nm)/sGGG. The diffractograms are shifted on the *y* axis for a better visibility.

The level of in-plane tensile strain influences the magnetic easy axis direction through induced magnetoelastic anisotropy. Thus, any variation of the strain level influences the line shape of the hysteresis loop. The structural characterization shows almost no strain variation with cooling rate. Thus, no influence of the cooling rate on the direction of the magnetic easy axis is expected. Hysteresis curves measured in oop geometry at room temperature are displayed in *Figure 29 (b)* after subtracting the substrate paramagnetic contribution and correcting the magnetic field values. All films show a similar line shape with no difference in remanent magnetization. A reduction of the coercive field by 70 Oe is measured when decreasing the cooling rate from -13 °C/min to -2 °C/min indicating a small reduction of the defect density.

# 4 Yttrium iron garnet thin films

This chapter focuses on the properties of $Y_3Fe_5O_{12}$ films grown by PLD in various conditions. First, investigations on films deposited on patterned substrates are carried out. The effect of annealing on the morphology and the structural and magnetic properties of amorphous films is also studied here.

## 4.1 Films on patterned substrates

In literature, nm thick YIG films grown at elevated temperatures on $Gd_3Ga_5O_{12}$ (short GGG) substrates are reported to possess exceptional structural, and static and dynamic magnetic properties. Following the steps described in the previous chapter, optimal growth conditions of YIG films on GGG(111) substrates were identified to be: 0.03 mbar oxygen pressure, 650 °C substrate temperature and 0.01 nm/s deposition rate.

*Figure 30* summarizes the morphologic and magnetic properties of an 18 nm thick film grown at optimal conditions. GGG(111) substrates show smooth surface characterized by an rms roughness value of $0.2 \pm 0.1$ nm. A heat treatment carried out at elevated temperatures (for 10 hours at 1100 °C in ambient atmosphere) leads to terrace-like structures due to a misalignment of the cut direction relative to the crystallographic directions. After deposition, the film shows a high quality surface characterized by an rms roughness of $0.1 \pm 0.1$ nm, and the terrace-like surface of the substrate as can be observed in *Figure 30 (a)*.

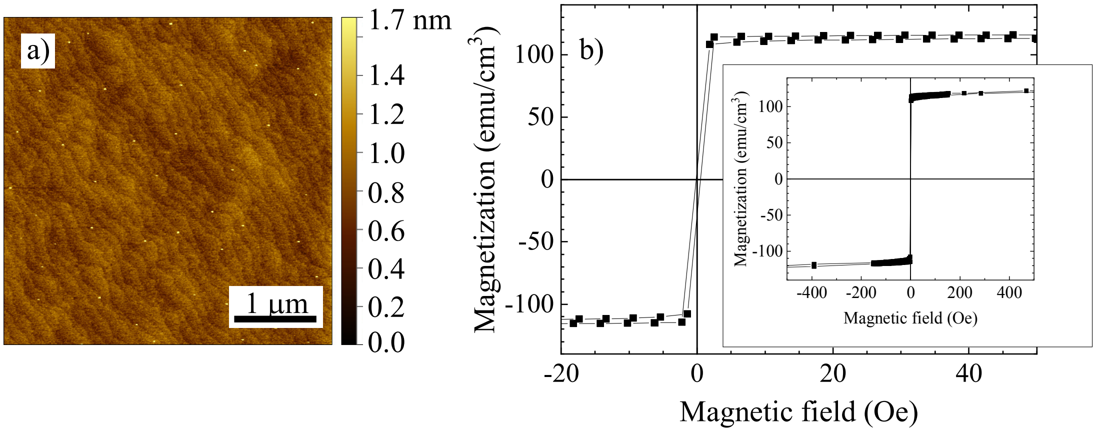

*Figure 30.* *a)* Surface morphology and *b)* in-plane hysteresis loop of an 18 nm thick YIG film grown on GGG(111) substrate.

Two magnetic anisotropies compete for the direction of the magnetic easy axis of YIG films grown on lattice-matching GGG substrates: the shape anisotropy that orients ***M*** in the sample plane, and the magnetocrystalline anisotropy with an easy axis of magnetization along the [111] crystal direction (see chapter 1.5). For a saturation magnetization of 140 emu/cm$^3$ for bulk YIG, the shape anisotropy ($K_s = -1.23 \cdot 10^2$ kerg/cm$^3$) overcomes the weak magnetocrystalline anisotropy ($K_1$ = -6.1 kerg/cm$^3$, ref. [18]), and YIG films grown on GGG(111) substrates show an in-plane (ip) easy axis of magnetization.

*Figure 30 (b)* displays the ip hysteresis loop of an 18 nm thick YIG film after subtracting the substrate paramagnetic signal and correcting the magnetic field values. The magnetic behavior towards larger magnetic fields is displayed in the inset of *Figure 30 (b)*. The sharp switching of the magnetization for the ip geometry indicates that the magnetic easy axis lies in the film plane. A saturation magnetization of around 130 ± 17 emu/cm$^3$ was measured which is slightly smaller compared to the bulk value of 140 emu/cm$^3$. The low coercive field of < 1 ± 2 Oe (affected by the sampling field step) indicates a good crystal structure with a low defect density. Due to a rather large field step size, no information regarding the remanent magnetization could be extracted.

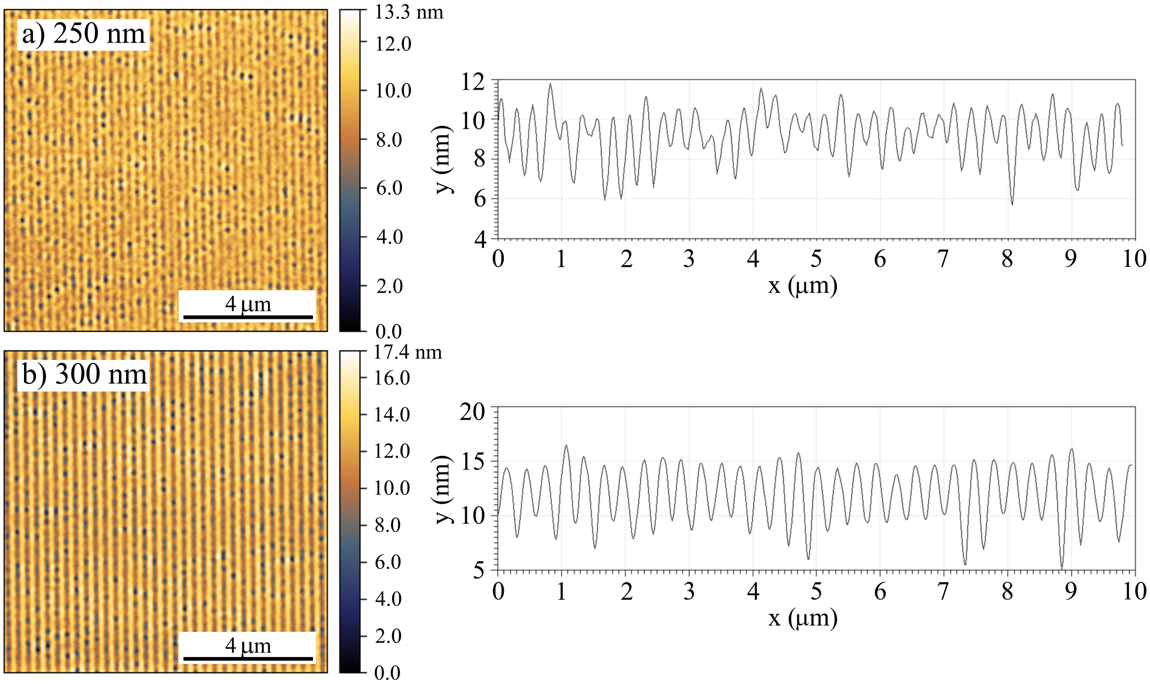

*Figure 31.* Topography images and line profiles after annealing GGG substrates with *a)* 250 nm and *b)* 300 nm line periodicity.

In the attempt of studying the spin wave propagation in structured YIG films, GGG(111) substrates were patterned in collaboration with I. Turcan from CEITEC, Brno (Czech Republic). Sinusoidal structures with an amplitude of 8 nm and a periodicity of 200 nm, 250 nm, and 300 nm were patterned by focused ion beam milling. Afterwards, the substrates were annealed for 10 hours at 1100 °C in ambient atmosphere in order to promote the surface recrystallization. The impact of the heat treatment on the patterned structures depends on the line periodicity. After annealing, the amplitude of the 200 nm and 250 nm structures becomes rather irregular with an averaged decrease of 2 nm, while it remains rather unchanged for the 300 nm periodicity, as can be seen from the topography images of the 250 nm and 300 nm structures in

*Figure 31*. 20 – 100 nm thick YIG films were grown at 600 °C substrate temperature, 0.04 mbar oxygen pressure, and 0.03 nm/s deposition rate. Topography images and profile lines of the 20 nm and 100 nm thick films grown on structures with a 200 nm periodicity are displayed in *Figure 32*. At the optimal growth conditions, films up to 100 nm thickness show a smooth surface and the pattern of the substrate surface. A slight decrease of the amplitude of the modulation to around 4 nm is measured after the deposition of a 20 nm thick film. Increasing the film thickness to 100 nm does not deteriorate the sinusoidal pattern. An increase of the modulation amplitude with increasing film thickness is apparent from *Figure 32 (c)*. The slightly increased amplitude of YIG(100 nm)/GGG to around 5 nm originates from the pits visible on the film surface (*Figure 32 (b)*). These defects form on the substrate surface after the heat treatment in ambient conditions.

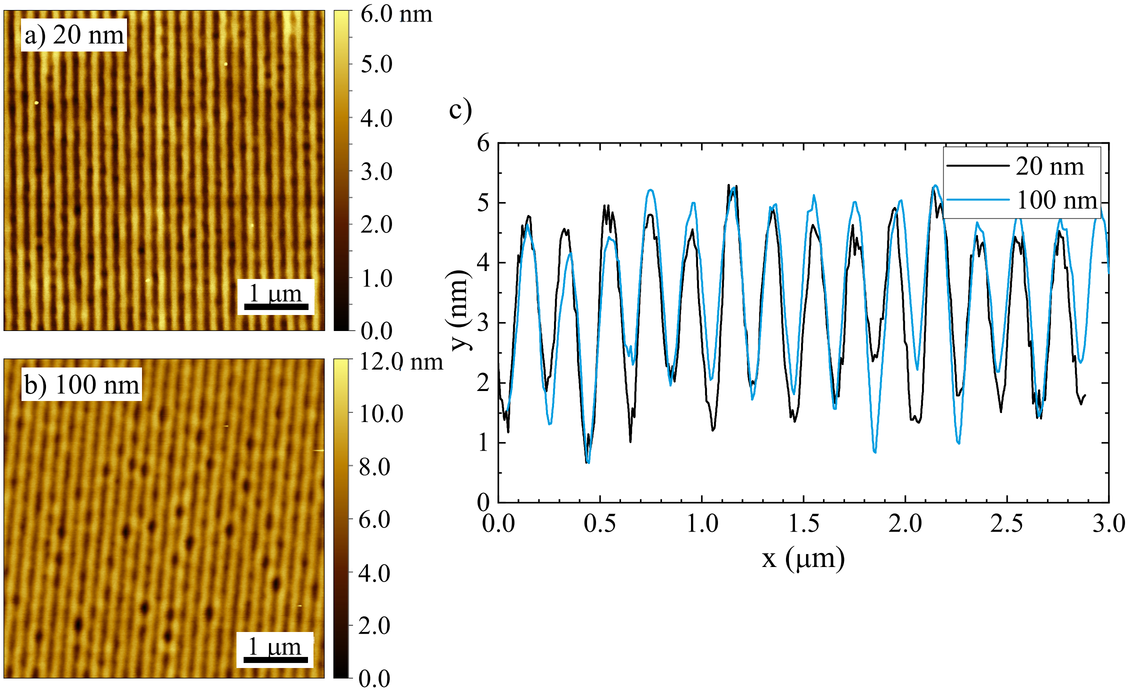

*Figure 32*. Topography images of *a)* 20 nm and *b)* 100 nm thick YIG films grown on sinusoidal structures with a 200 nm periodicity. *c)* Line profiles extracted from the topography images.

## 4.2 Annealing of amorphous films

Yttrium iron garnet films are commonly grown at elevated temperatures. Nevertheless, films grown at room temperature and annealed in oxygen [35] or argon [139] atmosphere crystallize in the garnet structure and show a sharp film-substrate interface. Very low Gilbert damping parameters $\alpha$ were reported in both cases, with $\alpha$ as low as $6 \cdot 10^{-5}$ for the film annealed in a pure oxygen atmosphere [35]. In the following, heat treatments of amorphous YIG films in ambient atmosphere were carried out.

30 nm thick YIG films were deposited at room temperature on GGG(111) substrates with a 0.01 nm/s deposition rate in $5 \cdot 10^{-3}$ mbar oxygen atmosphere. Post-deposition heat treatments were carried out in a furnace in ambient conditions. The amorphous films were heated with a 2 °C/min rate up to the annealing temperature ($T_A$) in the 550 – 775 °C range. The films were annealed for 30 minutes and allowed to cool down to room temperature. The surface morphology and magnetic properties were investigated by AFM and SQUID-VSM, respectively. The crystalline structure was evaluated by XRD in collaboration with O. Caha (Masaryk University, Brno, Czech Republic).

The topography images of the films after the heat treatments are displayed in *Figure 33* together with the surface morphology of an amorphous as-deposited film. After deposition, the films show a smooth surface with an rms roughness of 0.2 ± 0.1 nm. No significant morphological changes are observed after annealing at 550 °C. Small grains are apparent on the film surface without an impact on the surface roughness. With increasing $T_A$ to 600 °C, the surface grains slightly increase in size and density resulting in an increase of surface roughness to 0.6 ± 0.1 nm. Films annealed in the temperature range 650 – 725 °C show a high surface quality and a roughness of 0.3 ± 0.1 nm. Further increase of $T_A$ leads to large grains (300 µm wide and 8 nm high) distributed on the film surface (not shown here). Thus, YIG films annealed in air in a very broad temperature range show good surface morphology.

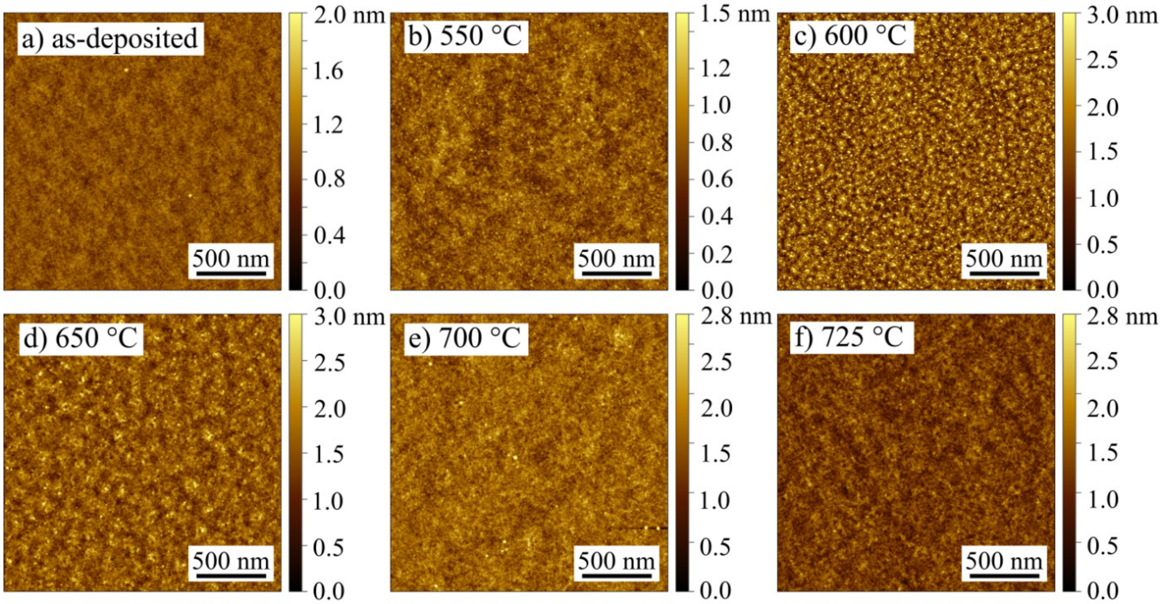

*Figure 33.* Surface morphology of YIG films *a)* after deposition at room temperature and *b)–f)* after annealing at temperatures between 550 °C – 725 °C for 30 minutes in ambient atmosphere. Different scales are used for a better visibility of specific features.

One method to probe that the annealing temperature ensures the film crystallization is by investigating the magnetic properties. High quality crystalline YIG films are characterized by an in-plane (ip) easy axis of magnetization, very small coercivity (<1 Oe) and a saturation magnetization $M_S$ of about 140 emu/cm$^3$. Next, the impact of the heat treatment on the magnetic properties was investigated by SQUID-VSM. Polar MOKE measurements of the films after deposition revealed no magnetic signal, an indication of the amorphous state of the as-grown films.

*Figure 34 (a)* shows the ip hysteresis loops of the films measured at room temperature after subtracting the substrate contribution and correcting the magnetic field values. For a better visibility, the loops of the films annealed at 650 °C, 700 °C, and 725 °C were shifted on the field axis by 2 Oe, 4 Oe, and 6 Oe, respectively. The film annealed at the lowest temperature of 550 °C shows a small $M_S$ of 38 ± 20 emu/cm$^3$ indicating that a heat treatment at this temperature for 30 minutes does not ensure complete crystallization. Films annealed at $T_A$ above 600 °C have an ip magnetic easy axis, very low coercivity (<1 ± 1 Oe), $M_S$ of around 125 ± 20 emu/cm$^3$, and high remanence. The coercivity is influenced by the sampling field step of 2 Oe. *Figure 34 (b)* displays the hysteresis curve of the film annealed at 600 °C measured in oop geometry. The magnetization slowly increases with the applied magnetic field and reaches saturation at around 2 kOe confirming that the normal direction is a magnetic hard axis.

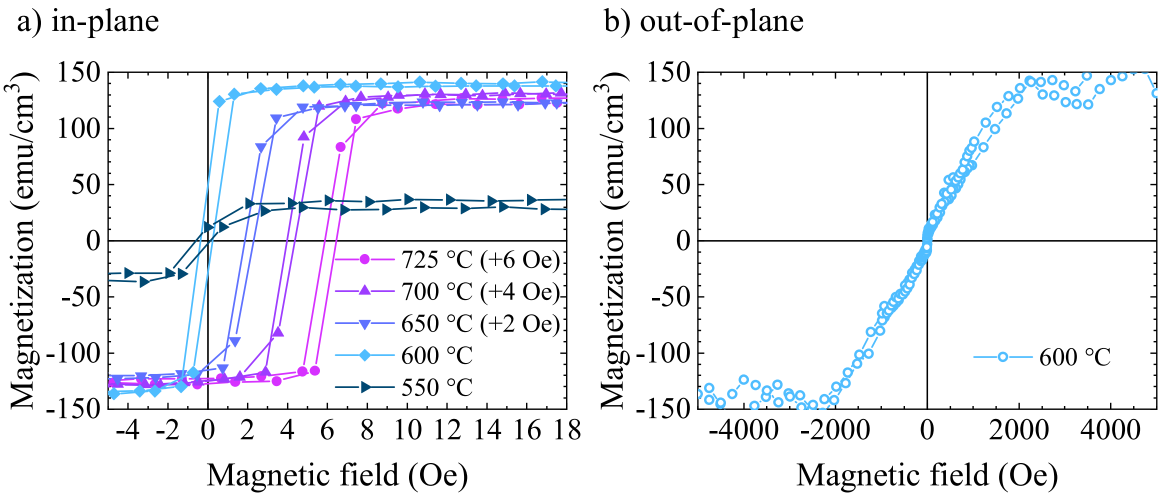

*Figure 34.* *a)* In-plane hysteresis loops of YIG films grown at room temperature and annealed in air for 30 minutes at various temperatures. For a better visibility, the measurements of the films annealed at 650 °C, 700 °C, and 725 °C were shifted on the field axis by 2 Oe, 4 Oe, and 6 Oe, respectively. b) Out-of-plane hysteresis curve of the film annealed at 600 °C.

The deviation of $M_S$ from the expected value is device- or material-related. The uncertainty of the measuring device is included in the value of the error bar given above. The material properties that affect $M_S$ are thickness and stoichiometry. The film thickness was evaluated by spectroscopic ellipsometry using the dielectric functions of YIG and GGG reported by Jakubisova-Liskova et al. [137,138]. Underestimating the film thickness by as low as 3 nm (which is a typical error size for this technique) results into an increase of $M_S$ by 20 emu/cm$^3$.

Manuilov et al. [140] simulated the dependence of $4\pi M_S$ on the number of $Fe^{oct}$ (denoted by $x$) and $Fe^{tet}$ (denoted by $y$) vacancies per formula unit. The effect of $Fe^{tet}$ and $Fe^{oct}$ vacancies on $M_S$ is different. Vacancies in the $Fe^{tet}$ site lead to a strong reduction of $M_S$, while increasing the number of vacancies in the $Fe^{oct}$ site results first in a slight increase of $M_S$ up to around 160 emu/cm$^3$ for $y = 0.5$ followed by a slow decrease. According to their simulations, a total of around 0.17 Fe vacancies/formula unit given by the uncertainty in the film stoichiometry could explain the reduced $M_S$ observed in *Figure 34* only when all Fe vacancies occupy the tetrahedral site. The Fe-deficient YIG films prepared by Manuilov et al. [140] show $M_S$ larger than the bulk value suggesting a preferential presence of Fe vacancies in the octahedral sites. Magnetic investigations of $Y_3[Fe_{2-x}Ga_x](Fe_{3-y}Ga_y)O_{12}$ single crystals revealed a decrease of $M_S$ with the total $(x + y)$ Ga content. Fittings of magnetization measurements with the Néel model revealed a preferential Ga occupation of the tetrahedral site [141]. Fe vacancies in the tetrahedral, or tetrahedral and octahedral sites lead to the reduction of the Curie temperature $T_C$ [141]. The decrease of $T_C$ corresponding to the possible amount of Fe vacancies in the YIG films falls within the uncertainty of the measurement (around 20 K) and, therefore, such investigations were not carried out. In order to assess the origin of the low $M_S$ observed in *Figure 34* further analysis of film thickness and stoichiometry are necessary.

Crystallographic studies of the film annealed at 650 °C were carried out using Cu K$\alpha_1$ radiation in collaboration with O. Caha from Masaryk University in Brno, Czech Republic. *Figure 35* shows the $\theta - 2\theta$ scans of the sample and a bare substrate measured after the alignment to the substrate GGG (444) reflection peak. The diffraction peak of the film (444) plane is hidden under the strong substrate signal. The heat treatment leads to epitaxial films with no lattice mismatch in the growth direction between the film and the substrate. Laue oscillations on the sides of the film peak are an indication of a smooth surface and an uniform crystal structure through the film thickness.

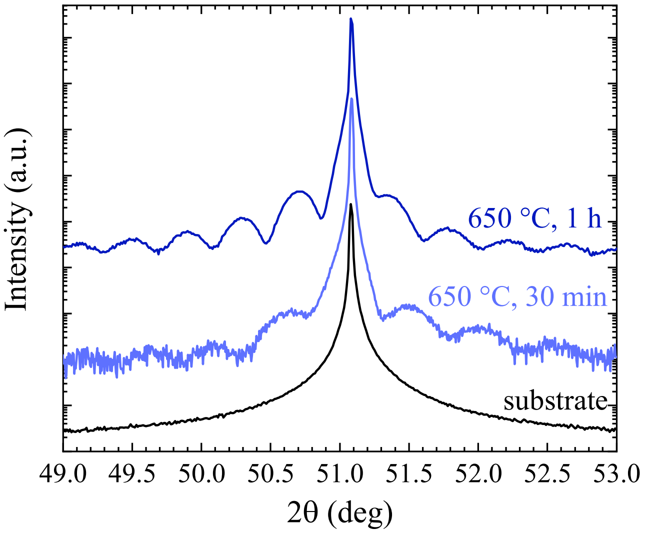

*Figure 35*. Diffraction patterns of YIG films annealed in ambient conditions at 650 °C for 30 minutes, and 1 hour. The scan of a GGG substrate is displayed for comparison. All patterns were acquired using Cu K$\alpha_1$ radiation.

A 40 nm thick YIG film grown at room temperature and annealed in ambient conditions for 1 hour at 650 °C is also displayed in *Figure 35*. Similar to the film annealed for 30 minutes, the interplanar spacing $d_{444}$ of the crystallized film matches the substrate structure. Before the film deposition, a heat treatment of the substrate at 1100 °C for 10 hours leads to a terrace-like surface. The films show the features of the substrate surface after annealing at 600 °C and 650 °C for 1 or 4 hours (*Figure 36*). However, cracks appear on the film surface for annealing times above 1 hour. The grooves become more prominent with annealing temperature and duration.

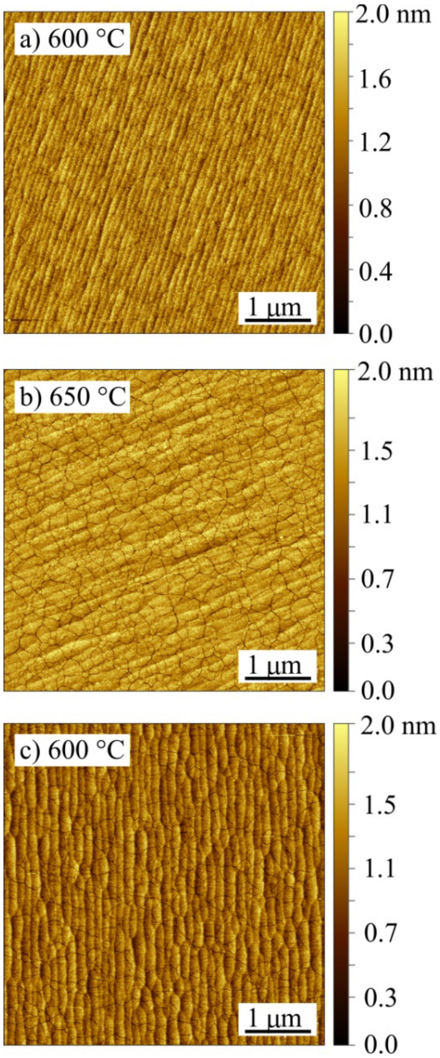

*Figure 36*. Topography images of 40 nm thick YIG films annealed in ambient atmosphere at *a)* 600 °C and *b)* 650 °C for 1 hour, and *c)* at 600 °C for 4 hours.

During growth at room temperature, more stress builds up in the 40 nm thick films investigated in *Figure 36* compared to the 30 nm thick layers of *Figure 33*. At elevated temperatures, structural rearranging takes place within the film which becomes stronger with increasing the annealing time and duration. Bulk YIG crystal is characterized by a thermal expansion coefficient ($25.6 \cdot 10^{-6}$ $K^{-1}$) larger than GGG ($7.1 \cdot 10^{-6}$ $K^{-1}$) [142]. Therefore, upon cooling, the film experiences tensile strain due to a larger thermal expansion coefficient. Cracks appear on the film surface as the stress built up during deposition and annealing relaxes. Studies on amorphous YIG films with various thicknesses annealed for durations above 1 hour are necessary to prove the origin of the stress.

### *Summary*

YIG films show high quality when grown on lattice-matching substrates. Films with a smooth surface can be prepared on heat-treated or patterned GGG substrates. Atomic sized terraces or 5 nm tall sinusoidal structures are still visible after the growth of 20 – 100 nm thick films. Heat treatments of amorphous structures in ambient conditions result in epitaxial films with properties comparable to films deposited at elevated temperatures: 100% remanence and coercivities below 1 Oe. While high quality layers are grown in a narrow range of substrate temperatures, post-deposition annealing revealed a broad temperature window (125 °C) in which crystalline YIG films show no deterioration of the magnetic properties. This flexibility in growing single crystal films at elevated temperatures or after annealing treatments makes possible the integration of YIG films in structures with materials that require diverse deposition conditions.

# 5 Thulium iron garnet thin films

Tensile-strained $Tm_3Fe_5O_{12}$ films can be grown on garnet substrates with a slightly larger unit cell, for example substituted-$Gd_3Ga_5O_{12}$ (sGGG) or $Gd_3Sc_2Ga_3O_{12}$ (GSGG). On one side, the lattice mismatch between bulk TmIG and substrate influences the level of in-plane tensile strain, the required condition for the presence of induced-magnetoelastic anisotropy (see chapter 1.5). On the other side, it dictates the thickness at which the films relax to the bulk TmIG structure. In this chapter, the influence of film thickness on the level of tensile strain was investigated for TmIG films grown on two substrate types.

## 5.1 $Tm_3Fe_5O_{12}$ films on substituted-$Gd_3Ga_5O_{12}$ substrates

TmIG films grown on sGGG substrates are reported to have an out-of-plane magnetic easy axis induced by in-plane tensile strain. However, the reports focus on extremely thin films (10 nm ref. [52] and < 5 nm ref. [53]) and no study has investigated the evolution of the in-plane tensile strain with film thickness. In the following, TmIG films with thicknesses (*t*) between 20 nm and 300 nm were epitaxially grown by PLD on sGGG(111) substrates at optimal growth conditions: 0.04 mbar oxygen pressure, 615 °C substrate temperature, and 0.03 nm/s deposition rate. The effect of film thickness on the structural and magnetic properties was investigated. FMR studies were carried out for the calculation of magnetic anisotropy and Gilbert damping, an important parameter for spintronics. These results have been recently published in ref. [127].

### 5.1.1 Crystallographic investigations

First, X-ray diffraction measurements were carried out to examine the evolution of the crystal structure with film thickness. *Figure 37* shows the XRD $\theta - 2\theta$ scans measured for all samples around the substrate (444) reflection. The diffraction pattern of a bare substrate is displayed for comparison. Bulk TmIG (444) diffraction peak is marked with a dashed vertical line.

From the XRD patterns, a strong influence of the TmIG film thickness on the crystalline structure is apparent. All films with thickness below 200 nm have the (444) diffraction peak at $2\theta$ angles larger than for bulk TmIG, which indicates a compressed lattice in the growth direction. This compression should result in an expanded lattice in the film plane inducing tensile strain, the required condition for obtaining an out-of-plane magnetoelastic anisotropy contribution. The largest distortion is observed for the thinnest films of 20 nm and 50 nm. With increasing film thickness, the (444) peak shifts towards smaller angles indicating a structural relaxation towards the bulk unit cell. A slight off-stoichiometry could explain the difference between the (444) peak positions of bulk and 300 nm thick film.

For a cubic system (like sGGG and TmIG), the <111> directions are equivalent and, according to Bragg's law, the corresponding crystal planes give rise to maxima at the same diffraction angle. Therefore, the distortion of the unit cell was investigated from the position of the (4-44) reflection. To access the (4-44) diffraction plane, each sample was tilted to $\chi = 70.53$ °. The corresponding scans are included in *Figure 37*. For the sGGG substrate, due to the cubic crystal structure, the (444) and (4-44) reflections overlap perfectly. On the other hand, pronounced differences are visible between the (444) and (4-44) reflections of the films clearly confirming the strong lattice distortion. For the 20 nm and 50 nm thick films, the (4-44) diffraction peak is hardly visible as a shoulder on the right side of the substrate peak. With increasing film thickness, the (4-44) diffraction peak shifts towards higher angles approaching the (444) reflection which indicates the relaxation towards the cubic structure.

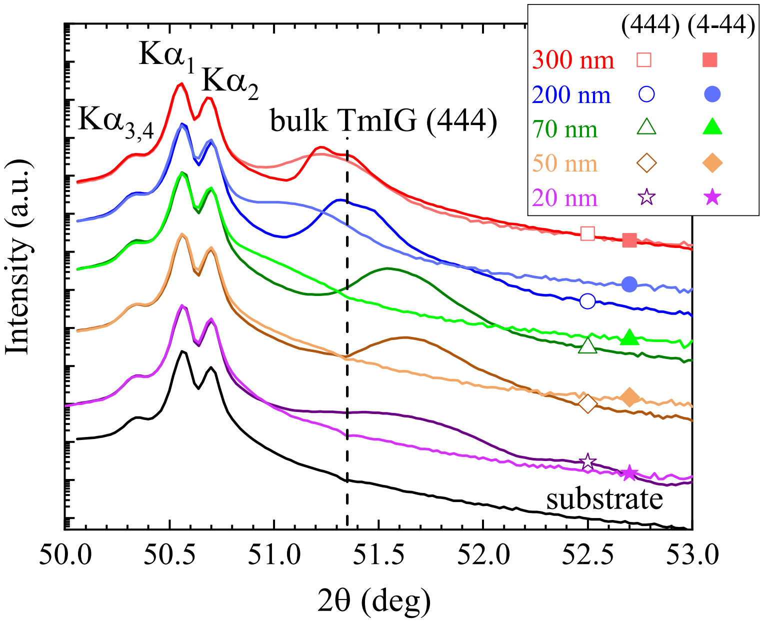

*Figure 37.* Diffraction patterns of the (444) and (4-44) planes of TmIG/sGGG(111) samples for various film thicknesses. The scan of a bare substrate is displayed for comparison. The patterns are shifted on the intensity axis for a better visibility. The position of bulk TmIG (444) reflection is marked with a dashed line.

The stress $\sigma^{\perp}$ in the [111] direction, given by eq. (1.3), was evaluated from the diffraction patterns. Young's modulus $Y$ and Poisson's ratio $\mu$ are not reported for TmIG, and, instead, the values of $Y = 2\cdot10^{9}$ kerg/cm$^3$ and $\mu = 0.29$ of YIG (ref. [143]) were used for the calculation of $\sigma^{\perp}$.

The film interplanar spacing $d_{\mathrm{film}}^{444}$ was evaluated from the diffraction angle using Bragg's law. The diffraction angles were identified by modeling each pattern with five Voigt functions: three describing the substrate interaction with the Cu K$\alpha_1$, K$\alpha_2$, and K$\alpha_{3,4}$ radiations and two for the film (K$\alpha_1$, K$\alpha_2$). A Voigt function represents a convolution of a Gaussian and a Lorentzian distribution and it is described by the offset $y_0$, center $x_c$, area $A$, Gaussian and Lorentzian full width at half maxima (FWHM) $w_G$ and $w_L$, respectively. *Figure 38 (a)* shows the XRD pattern of TmIG(200 nm)/sGGG together with the convolution of the Voigt functions. Since the ends of each diffractogram correspond to different counts, it is not possible to model simultaneously both sides with one offset value. Considering that the $2p_{3/2}\rightarrow 1s$ orbital transition that generates the K$\alpha_1$ radiation has double the probability of the $2p_{1/2}\rightarrow 1s$ transition that produces the K$\alpha_2$ radiation, the area of the peak corresponding to K$\alpha_1$ (denoted $A_{1\text{-s}}$ and $A_{1\text{-f}}$ for substrate and film, respectively) should be double the area of the peak generated by K$\alpha_2$ ($A_{2\text{-s}}$, $A_{2\text{-f}}$) for both substrate (s) and film (f). However, the measurements show lower values than expected for $A_{2\text{-s}}$ and $A_{2\text{-f}}$ caused, probably, by the Goebel mirror placed in the beam path. The FWHM of the peaks corresponding to K$\alpha_1$ and K$\alpha_2$ were set equal. The contributions to the peak FWHM are instrumental (finite size of X-ray beam, wavelength distribution of the X-ray source, monochromatization process) and sample-related broadening (crystallites size, concentration gradients, strain) [112]. While the instrumental broadening is described by a Gaussian profile, the sample contribution to the peak lineshape is Gaussian and/or Lorentzian [112]. Throughout the sample series, the substrate $w_{\text{L-s}}$ and $w_{\text{G-s}}$ were found to be 0.02 ° ± 0.002 ° and 0.051 ° ± 0.004 °, respectively. Thus, the film $w_{\text{L-f}}$ and $w_{\text{G-f}}$ were set to be larger than these values.

From models similar to the one shown in *Figure 38 (a)*, the film (444) and (4-44) diffraction angles were identified and they are summarized in *Figure 38 (b)*. The (4-44) diffraction angle of TmIG(20 nm)/sGGG, completely hindered by the substrate signal, could not be fitted. Similarly, the values for the 50 nm and 70 nm thick films were estimated with a higher uncertainty. The strongest distortion of the unit cell and the highest strain (*Table 3*) is observed for $t = 50$ nm. With increasing film thickness, the unit cell relaxes towards the expected cubic structure ($d^{444} = d^{4\text{-}44}$) leading to strain reduction. However, no complete relaxation is observed throughout the thickness series. Considering that the films converge towards a lattice constant larger than of stoichiometric bulk TmIG (*Figure 37*), the interplanar distance $d^{444}_{\text{bulk}}$ of the structure towards which the films converge was used for the calculation of $\sigma^{\perp}$. According to *Figure 37*, the (4-44) diffraction peak of TmIG(20 nm)/sGGG is at the lowest $2\theta$ angle of the thickness series. Therefore, the (444) diffraction peak would be expected at the highest diffraction angle resulting in the strongest distortion of the unit cell and highest stress of the series. However, rather low $2\theta$ and stress values were obtained for the 20 nm thick film which do not follow the evolution with film thickness.

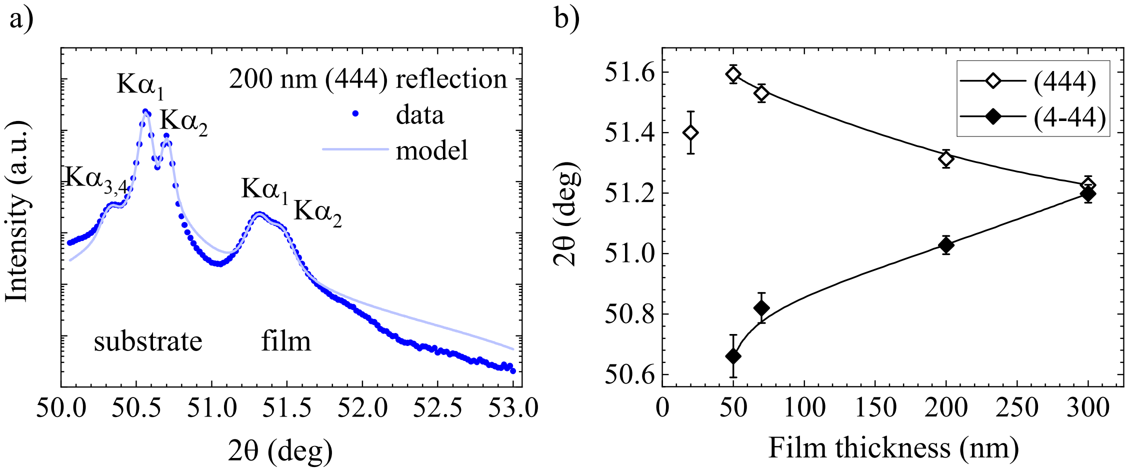

*Figure 38.* *a)* XRD pattern of TmIG(200 nm)/sGGG (dark symbols) together with the model (solid line) representing the convolution of five Voigt functions. *b)* Diffraction angles of the film (444) and (4-44) planes for various film thicknesses.

The stress was calculated for an uniform distribution through the film. However, according to *Figure 37*, the 50 nm, 70 nm, and 200 nm thick films show additional weak peaks at higher diffraction angles. They would correspond to a larger compression of the unit cell in the growth direction, and therefore, a higher in-plane tensile strain. The fraction of the film exhibiting a higher in-plane strain would be most probably at the film-substrate interface. Diffraction patterns measured with monochromatic radiation would be required to differentiate parts of the film with a change in strain.

*Table 3.* Level of stress in the growth direction for TmIG films on sGGG(111) substrates.

| Film thickness (nm) | $\sigma^{\perp}$ ($10^6$ kerg/cm$^3$) |
|---|---|
| 20 | 5.6 ± 1.4 |
| 50 | 11.0 ± 0.2 |
| 70 | 9.2 ± 0.1 |
| 200 | 3.2 ± 0.2 |
| 300 | 0.7 ± 0.1 |

### 5.1.2 Magnetic properties

The static and dynamic magnetic properties were investigated by SQUID-VSM magnetometry and ferromagnetic resonance (FMR), respectively. The FMR studies were conducted in collaboration with A. Semisalova and K. Lenz from Helmholtz-Zentrum Dresden-Rossendorf, Germany.

It is expected that the observed structural changes will strongly influence the magnetic properties. In order to possess an out-of-plane magnetic easy axis, the induced-magnetoelastic anisotropy has to overcome the magnetic shape anisotropy of the film (the magnetocrystalline contribution is discussed below). *Figure 39* displays the normalized $M-H$ hysteresis loops measured with the magnetic field applied in the out-of-plane (oop) and in-plane (ip) directions after subtracting the substrate paramagnetic contribution and correcting the magnetic field.

The 50 nm thick TmIG film exhibits a rather squared hysteresis loop in oop direction with a coercivity of about 230 Oe. For the ip direction, a small hysteresis with a lower coercivity of 60 Oe and a linearly increasing magnetization towards saturation is obtained. Thus, for this film thickness, the magnetoelastic anisotropy is dominant and the magnetic easy axis is along the surface normal. Based on the level of tensile strain, a similar behavior is expected for the 20 nm thick TmIG film. However, in case of weak magnetic film signals, the hysteresis loops become noisy, in particular at higher fields, after subtracting the substrate contribution. In this case, an additional polar magneto-optical Kerr effect (MOKE) hysteresis loop was measured using a blue laser source ($\lambda = 405$ nm) and it is displayed in the inset of *Figure 39 (a)*. The MOKE loop reveals a similar shape as observed by SQUID-VSM, and confirms the oop easy axis of magnetization with a rather low coercivity of about 37 Oe. With increasing film thickness, the magnetic easy axis rotates towards the sample plane due to the loss in magnetoelastic anisotropy and competing contribution of the magnetic shape anisotropy.

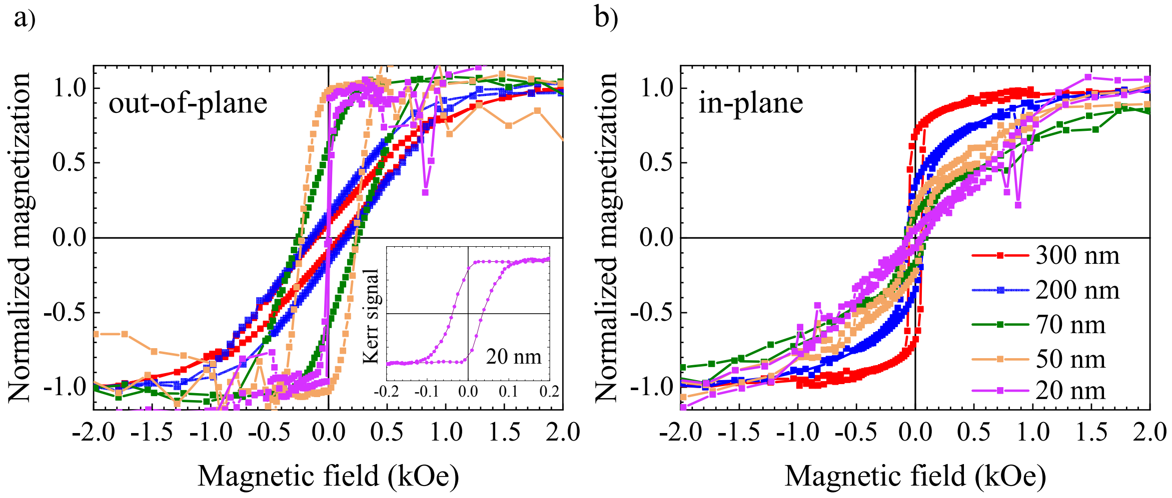

*Figure 39.* Normalized hysteresis loops of TmIG($t$)/sGGG measured in *a)* out-of-plane and *b)* in-plane geometry. The paramagnetic substrate contribution is subtracted from the experimental data. Inset shows the polar MOKE curve of the 20 nm thick film.

*Figure 40 (a)* shows the saturation magnetization $M_S$ in dependence on the TmIG film thickness. $M_S$ values of about 90 emu/cm$^3$ remain almost constant within the experimental error. The values are smaller than for bulk TmIG of 110 emu/cm$^3$ but in good agreement with values reported by other groups [54–56,144]. A slight off-stoichiometry or an underestimated film thickness could result in lower $M_S$ values.

The effective magnetic anisotropy $K_{eff}$ was estimated from the area enclosed between the oop and ip loops in one quadrant of the $M - H$ curves. It contains both perpendicular $K_u$ and shape $K_s$ anisotropies. The values of $K_{eff}$ are summarized in *Figure 40 (b)*. Based on the calculation method, positive $K_{eff}$ values indicate an oop magnetic easy axis. For most garnets, <111> directions are the magnetic easy axes. Therefore, the two contributions to the perpendicular magnetic anisotropy $K_u$ are the magnetocrystalline anisotropy $K_1$ and the magnetoelastic anisotropy $K_\sigma$ induced by tensile strain. For bulk TmIG, the first order cubic anisotropy constant $K_1$ is in the range of $-11$ kerg/cm$^3$ $< K_1 <$ $-5.8$ kerg/cm$^3$ and it is often neglected [18]. Therefore, the induced-magnetoelastic anisotropy competes with the magnetic shape anisotropy for the magnetic easy axis direction.

With the values of $K_{eff}$ and $M_S$, the perpendicular magnetic anisotropy energy density $K_u = K_{eff} - K_s$ (filled blue triangles in *Figure 40 (b)*) was calculated to be around 60 – 100 kerg/cm$^3$ for films with $t$ below 70 nm (for the definition of $K_s$ please see chapter 1.5). With increasing film thickness, the $K_u$ values get reduced and eventually the magnetization rotates towards the film plane as indicated by the sign change of $K_{eff}$.

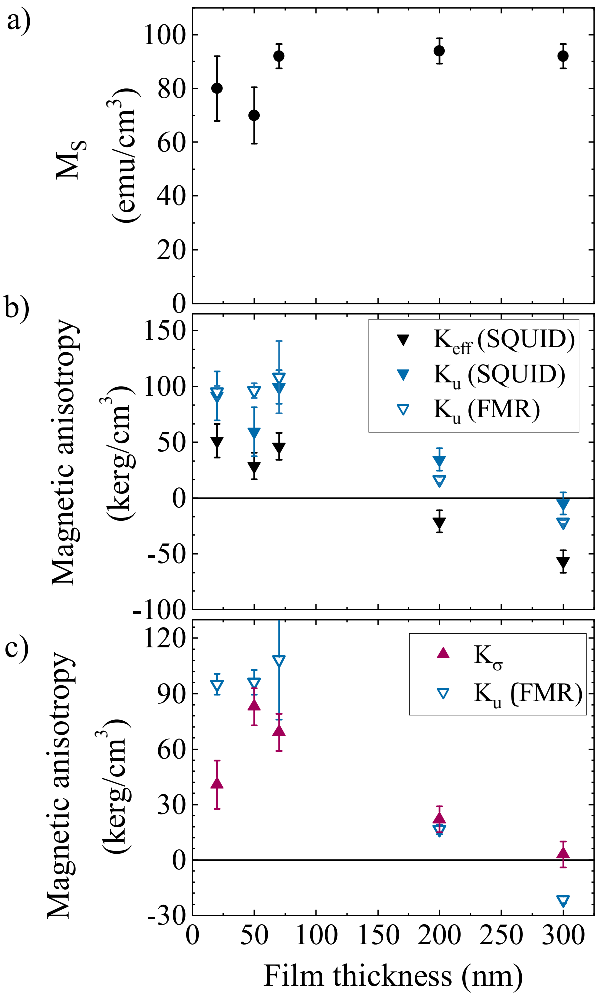

*Figure 40.* Dependence of *a)* saturation magnetization $M_S$ and *b),c)* magnetic anisotropy on TmIG film thickness.

Due to rather noisy loops for films thinner than 70 nm and the calculation method, $K_{eff}$, and by extension $K_u$, are subjected to errors. A more accurate method to determine $K_u$ is by conducting FMR studies. The FMR spectra ($S_{21}$ vs applied magnetic field) were recorded for each sample in the frequency range from 1 to 40 GHz for in-plane and out-of-plane direction of the applied magnetic field. The resonance field $H_{res}$ and the peak-to-peak linewidth $\Delta H_{pp}$ were determined by fitting the spectra with a complex Lorentzian function. Polar angular dependencies (with respect to the sample normal and denoted by $\theta$ with $\theta = 0°$ corresponding to the out-of-plane magnetic field direction) of $H_{res}$ were measured to extract the perpendicular anisotropy $K_u$. At $\theta_H = 0°$ and $\theta_H = 90°$, $K_u$ can be calculated using Kittel formulae (see chapter 2.6) and the $M_S$ values from SQUID-VSM measurements.

The FMR spectra of the 50 nm and 300 nm thick films measured at 10 GHz in oop and ip geometries are displayed by symbols in *Figure 41*. The solid curves represent fits to the experimental data. For $t = 50$ nm, $H_{res}$ is the lowest in the oop direction, implying that the magnetic easy axis is normal to the film plane. A similar behavior was observed for $t = 20$ nm and 70 nm. In contrast, for the 300 nm thick film, the lowest $H_{res}$ was measured for $\theta_H = 90°$.

Therefore, at this film thickness, the magnetic easy axis lies in the sample plane. Additionally, for $\theta_H = 0°$ spin waves up to the 4th mode can be observed on the left side from the main mode. An undergoing study of the observed spin waves will allow the extraction of the exchange stiffness. TmIG(200 nm)/sGGG shows a similar dependence.

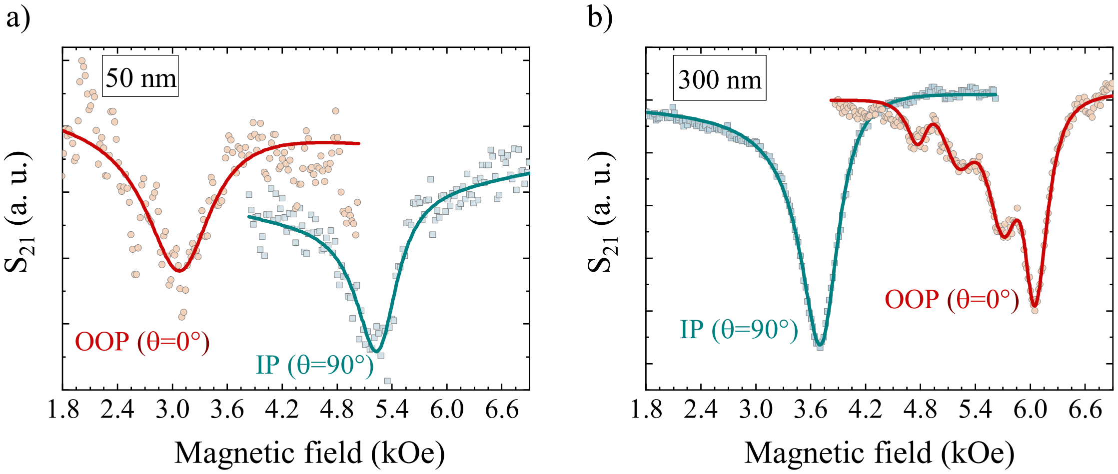

*Figure 41.* Experimental (symbols) and fitted (solid line) FMR spectra of *a)* 50 nm and *b)* 300 nm thick TmIG films, respectively, measured at 10 GHz in out-of-plane ($\theta_H = 0°$) and in-plane ($\theta_H = 90°$) applied magnetic field. The FMR signal was corrected for the substrate contribution.

The $K_u$ values evaluated from FMR measurements are displayed in *Figure 40 (b)* by empty symbols. The difference between the $K_u$ values extracted from FMR and SQUID-VSM data could be explained by the calculating method of $K_u$ from the hysteresis loops. As mentioned above, $K_u$ is given by the area enclosed between the oop and ip curves in one quadrant. The subtraction of a strong substrate signal might affect the value of the anisotropy field, making the calculation of $K_u$ from hysteresis loops error prone. Nevertheless, both techniques give similar values and show clearly the trend of $K_u$ with film thickness.

As mentioned above, the main contribution to $K_u$ is the magnetoelastic anisotropy. $K_\sigma$ was calculated using eq. (1.2) and the obtained values are displayed in *Figure 40 (c)*. $K_u$ obtained from the FMR measurements is also included. The highest $K_\sigma$ of $86 \pm 7$ kerg/cm$^3$ was found for the 50 nm thick film and it closely matches $K_u$. As expected from the structural relaxation, $K_\sigma$ strongly decreases with film thickness reaching the smallest value of $6 \pm 7$ kerg/cm$^3$ for $t = 300$ nm. For $t$ above 50 nm, $K_\sigma$ and $K_u$ show a similar decrease with increasing film thicknesses. For the thinnest film, a large discrepancy is observed between $K_\sigma$ and $K_u$. The reduced $K_\sigma$ value originates from the small stress calculated for this film thickness.

The dimensionless Gilbert damping parameter $\alpha$ was evaluated from the frequency dependence of the resonance linewidth $\Delta H_{pp}$ measured in the oop magnetic field geometry for the 70 nm, 200 nm, and 300 nm thick films, and ip magnetic field geometry for the two thinnest films (20 nm and 50 nm). The latter configuration was selected due to the overlap of the film signal with the substrate contribution when measured in the easy axis direction. The damping constant obtained by fitting the frequency-dependent linewidth with eq. (6.2) is plotted in *Figure 42 (a)*. $\alpha$ is in the 0.015 – 0.025 range, comparable to the lowest value of 0.0133 reported for 10 – 30 nm thick films on GGG substrates [56]. The Gilbert damping of TmIG films is two orders of magnitude larger than for YIG films, mainly due to a larger spin-orbit coupling [126]. Additionally, $\alpha$ shows no clear dependence on the layer thickness.

The inhomogeneous broadening $\Delta H_{\mathrm{inhom}}$ equivalent to the zero frequency offset was also obtained from the frequency dependence of $\Delta H_{\mathrm{pp}}$ and it is plotted in *Figure 42 (b)* for all film thicknesses. $\Delta H_{\mathrm{inhom}}$ was found to be below 100 Oe for $t = 20$ nm and 300 nm. Values as large as 260 ± 50 Oe were estimated for the rest of the series indicating pronounced inhomogeneities of the magnetic properties within these films.

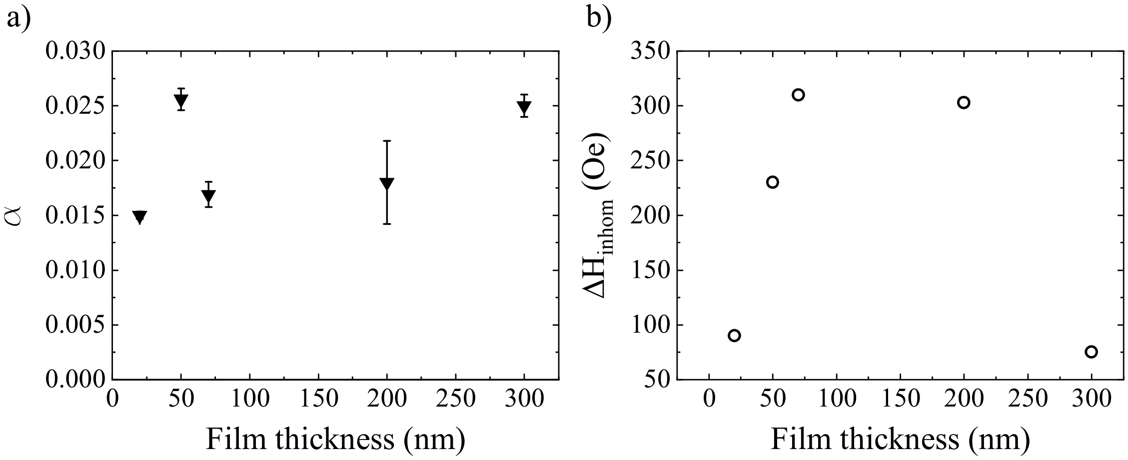

*Figure 42.* *a)* Gilbert damping $\alpha$ and *b)* inhomogeneous broadening $\Delta H_{\mathrm{inhom}}$ of the TmIG films.

The surface morphology of the 70 nm thick TmIG film investigated by AFM shows an rms roughness of about 0.8 ± 0.1 nm extracted from the topographic image presented in *Figure 43 (a)*. Throughout the series, all samples exhibit a rather low rms roughness of below 1 nm. Magnetic force microscopy (MFM) was used to image the domain structure of the same film after demagnetization revealing a typical domain pattern with up and down magnetized domains in the size range of about 300 nm (*Figure 43 (b)*), confirming as well the presence of an oop magnetic easy axis.

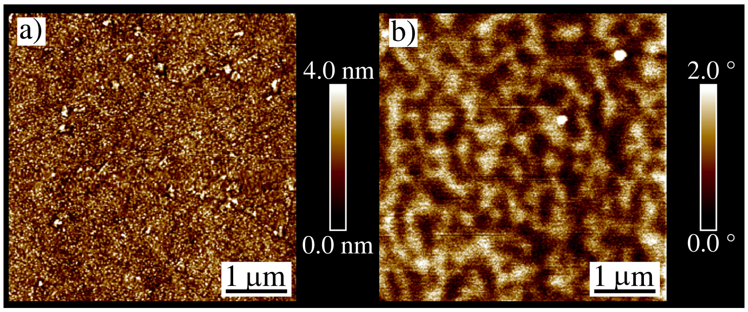

*Figure 43.* *a)* Surface topography and *b)* magnetic domain structure of the 70 nm thick film. The images were acquired at different positions.

## 5.2 $Tm_3Fe_5O_{12}$ films on $Gd_3Sc_2Ga_3O_{12}$ substrates

$Gd_3Sc_2Ga_3O_{12}$ (short GSGG, $a = 12.554$ Å) substrates are another candidate for the growth of tensile-strained $Tm_3Fe_5O_{12}$ films. Nevertheless, the large lattice mismatch between bulk TmIG and substrate ($\Delta = 100(a_{\text{sub}} - a_{\text{film}})/a_{\text{sub}} = 1.84$ %) is expected to lead to a faster strain relaxation with increasing film thickness as compared to substituted-GGG substrates. First, the quality of the substrate surface was improved by annealing in ambient atmosphere. The evolution of tensile strain with film thickness was investigated by means of XRD and SQUID-VSM. In the end, annealing of amorphous and crystalline TmIG films in ambient atmosphere was studied as a prospect of integrating TmIG films in garnet heterostructures.

### 5.2.1 Heat treatment of $Gd_3Sc_2Ga_3O_{12}$ substrates

Two aspects are important for the growth of high quality epitaxial thin films: the substrate, and the energy balance of incident particles and substrate temperature during deposition. The substrate influences the film properties through crystal structure and surface morphology. The side of the substrate used for the film growth is mechanically polished to a specified roughness, and, as a result, the crystal structure of the surface changes. One method to recover the bulk-like crystal structure is by undergoing a heat treatment.

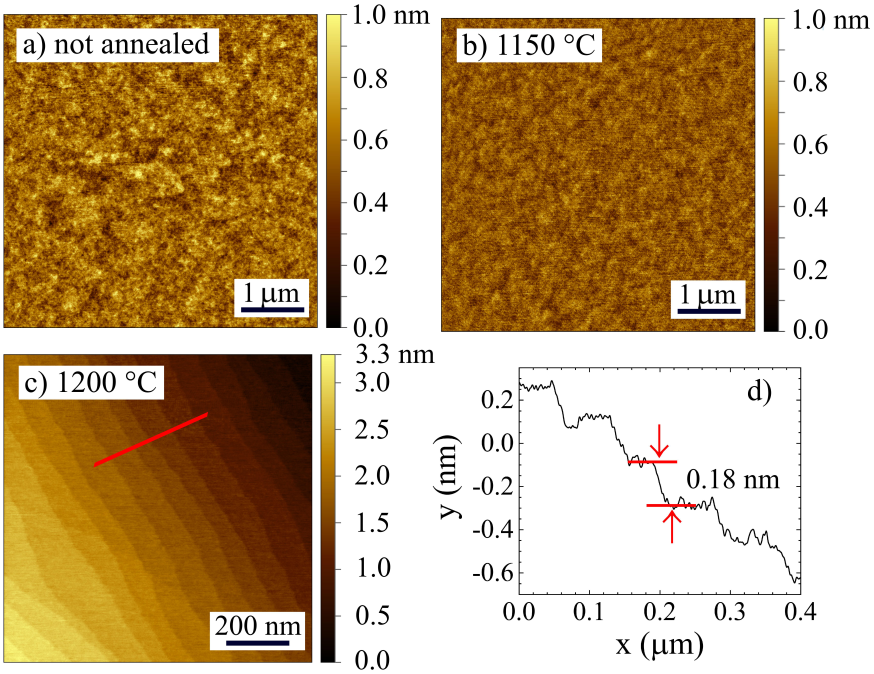

*Figure 44.* Surface morphology of GSGG(111) substrates *a)* before, and after heat treatments for 8 hours in ambient atmosphere at *b)* 1150 °C and *c)* 1200 °C. *d)* Profile of the segment marked in *c)*. Different scales are used in the AFM images for a better visibility of specific features.

For the identification of the re-crystallization temperature, GSGG(111) substrates were annealed for 8 hours in ambient atmosphere at temperatures between 1100 °C and 1200 °C. The surface morphology was monitored by AFM and the topography images are displayed in *Figure 44*. For comparison, an as-received GSGG substrate is shown in *Figure 44 (a)*. With an rms roughness of 0.2 ± 0.1 nm, the substrates show excellent surface quality for the growth of thin films. Heat treatments at 1100 °C and 1150 °C resulted in no morphological change while the surface roughness reduced slightly to 0.1 ± 0.1 nm. After annealing at 1200 °C smooth terraces are visible on the substrate surface indicating that atomic diffusion is promoted at this temperature. The profile over several terraces is displayed in *Figure 44 (d)*. Linear fits of the terraces reveal an average step height of 1.8 Å which is close to the (444) interplanar spacing of GSGG. Based on these results, GSGG substrates used in the following studies undergo a heat treatment at 1200 °C for 8 hours before film deposition.

### 5.2.2 Film thickness series

Based on the lattice mismatch between TmIG and GSGG, TmIG films grown on this substrate type are expected to show sufficient in-plane tensile strain leading to a dominant magnetoelastic anisotropy, similar to the previous results on sGGG substrates. Three TmIG films were epitaxially grown at the optimal conditions: $0.5\cdot10^{-3}$ mbar oxygen pressure, 0.01 nm/s deposition rate, and 600 °C growth temperature. After deposition, the samples were cooled in the same atmosphere with -5 °C/min down to 200 °C. At this temperature, the power supply of the heater was turned off. The film thicknesses were evaluated to be 14 ± 3 nm, 37 ± 5 nm, and 67 ± 5 nm from ellipsometry spectra, as described previously. The evolution of in-plane tensile strain with film thickness was investigated with a focus on the structural and magnetic properties.

First, the structural analysis was carried out to observe the evolution of the crystal structure with film thickness. The distortion of the unit cell was investigated from the diffraction angles corresponding to the (444) and (4-44) planes. The XRD $\theta - 2\theta$ scans of the samples, measured after the alignment to the substrate (444) and (4-44) diffraction planes, are displayed in *Figure 45*. The dashed line marks the position of bulk TmIG (444) reflection.

The film thickness influences strongly the crystal structure. The (444) diffraction peak of the thinnest layer is at a $2\theta$ angle larger than for bulk TmIG. This corresponds to a compressed unit cell in the growth direction. The presence of the (4-44) reflection close to the substrate peak and hardly visible in *Figure 45* indicates a strong distortion of the lattice. Increasing film thickness leads to the relaxation of the unit cell as the film (444) and (4-44) peaks shift towards the bulk value. For the 67 nm thick film, the (444) and (4-44) crystal planes give rise to diffraction maxima roughly at the same angle indicating an almost complete relaxation to the cubic structure. The difference between the diffraction angles of bulk and 67 nm thick film could result from a slight off-stoichiometry. The strain level of the 14 nm thick TmIG film on GSGG substrate corresponds to the strain level of the 50 nm thick film on sGGG substrate. Therefore, it is expected that TmIG(14 nm)/GSGG possesses an oop easy axis of magnetization.

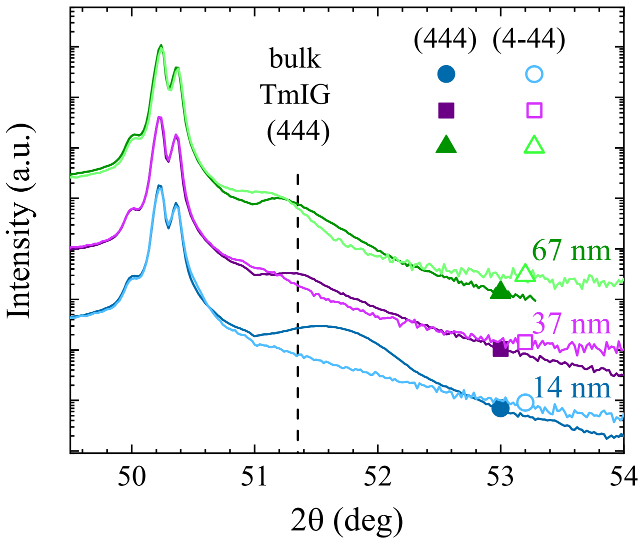

*Figure 45*. X-ray diffractograms of the (444) and (4-44) planes of TmIG(*t*)/GSGG. The position of bulk TmIG (444) diffraction peak is marked with a dashed line. The patterns are shifted on the intensity axis for a better visibility.

Magnetic investigations at room temperature were carried out by SQUID-VSM magnetometry. *Figure 46* displays the hysteresis loops of the films measured in oop and ip geometry. The saturation magnetization of around 90 ± 20 emu/cm$^3$, slightly smaller than the bulk value of 110 emu/cm$^3$, remains rather constant through the thickness series. As expected from the structural characterization, the film thickness influences the magnetic properties. In oop geometry, the 14 nm thick film shows a squared hysteresis loop with a coercivity of 25 ± 2 Oe and 100% remanence. For the ip direction, a very low magnetization is obtained after subtracting the substrate contribution. In this geometry, $M$ is expected to slowly increase with $H$ until reaching saturation. The low film signal might be affected by the evaluation method of the substrate paramagnetic contribution or it could originate from a faulty measurement. Nevertheless, the squared hysteresis loop measured in oop geometry clearly indicates that the magnetic easy axis lies along the sample normal direction. As a consequence of the faulty ip hysteresis loop, the effective anisotropy and uniaxial anisotropy could not be evaluated for TmIG(14 nm)/GSGG. The reduction of strain with increasing film thickness leads to the decrease of magnetoelastic anisotropy. Therefore, the shape anisotropy becomes dominant and the magnetic easy axis direction rotates towards the film plane as observed for the 67 nm thick film. The large lattice mismatch between bulk TmIG and GSGG results in a fast structural relaxation of strained films grown on this substrate type. The magnetoelastic anisotropy is dominant for TmIG films grown on GSGG substrates for thicknesses below 37 nm, while films on sGGG substrates show perpendicular magnetic anisotropy up to 70 nm film thickness.

The film morphology was investigated by AFM and the corresponding topography images are displayed in *Figure 47*. An increase of surface roughness is observed through the series. Rms roughness values of 0.8 ± 0.1 nm, 1.4 ± 0.3 nm, and 2.0 ± 0.5 nm were extracted from the scanned windows for $t$ = 14 nm, 37 nm, and 67 nm, respectively.

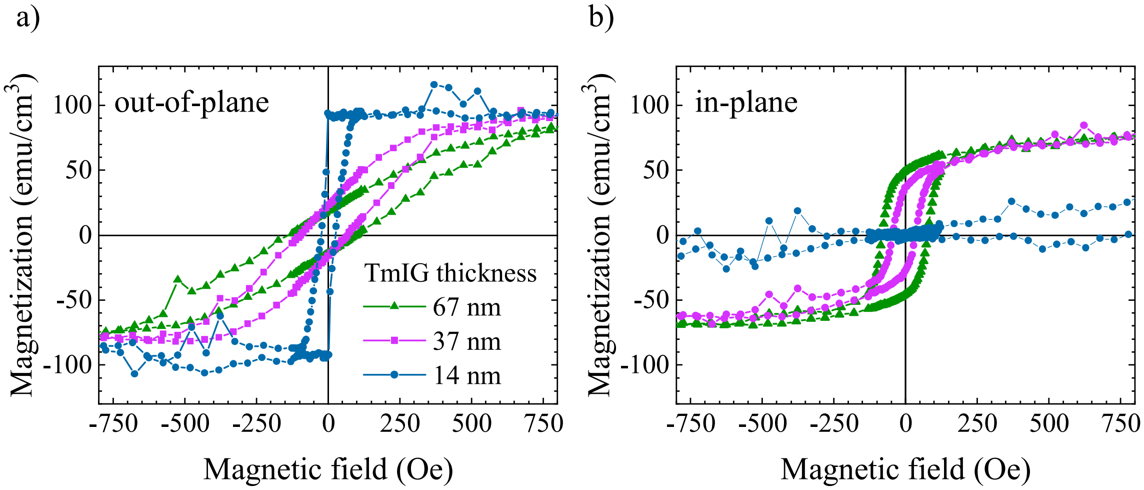

*Figure 46*. Hysteresis curves of TmIG(*t*)/GSGG(111) measured in *a)* out-of-plane and *b)* in-plane geometry after subtracting the substrate paramagnetic signal.

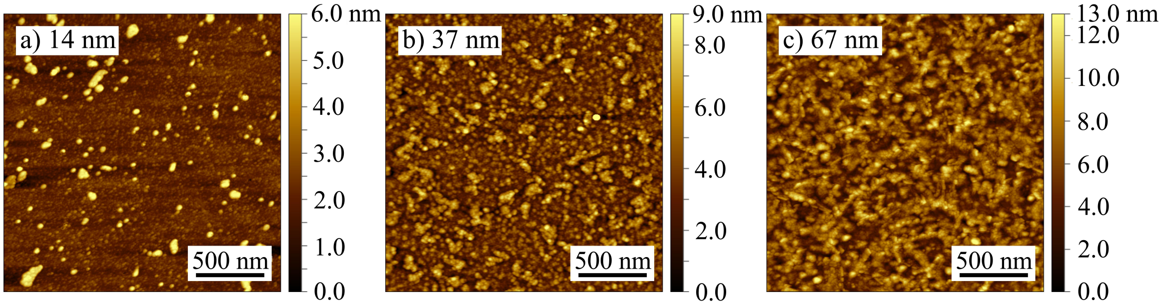

*Figure 47*. Surface morphology of *a)* 14 nm, *b)* 37 nm and *c)* 67 nm thick TmIG films. Different scales are used for a better visibility of specific features.

### 5.2.3 Annealing of crystalline layers

In the following, the impact of a post-deposition heat treatment on TmIG films is investigated. A 14 nm thick TmIG film grown on GSGG(111) substrate showing an oop magnetic easy axis was annealed in ambient atmosphere at 600 °C and 650 °C for 30 minutes. The temperature was increased at a rate of 2 °C/min to avoid temperature overshooting. After each heat treatment, the surface morphology, structural and magnetic properties were evaluated.

First, AFM investigations were carried out to monitor the impact of annealing on film morphology. *Figure 48* shows the topography images of the as-deposited and annealed films. After deposition, the film shows a rather rough surface with an rms roughness of 0.8 ± 0.1 nm due to the large defects covering the surface. Areas between droplets are as smooth as 0.3 ± 0.1 nm. After each heat treatment the surface roughness increases due to the growing size of the defects. The roughness values extracted from the scan window are 1.9 ± 0.3 nm and 2.7 ± 0.5 nm after annealing at 600 °C and 650 °C, respectively. Areas not covered by droplets show a much smaller deterioration. No morphological change is observed after the first heat treatment while the roughness increased slightly to 0.4 ± 0.1 nm. The annealing process at 650 °C leads to a further increase of the roughness to 0.5 ± 0.1 nm. However, in this case, cracks are visible on the film surface indicated by white arrows. Therefore, further heat treatments at higher temperatures were not considered.

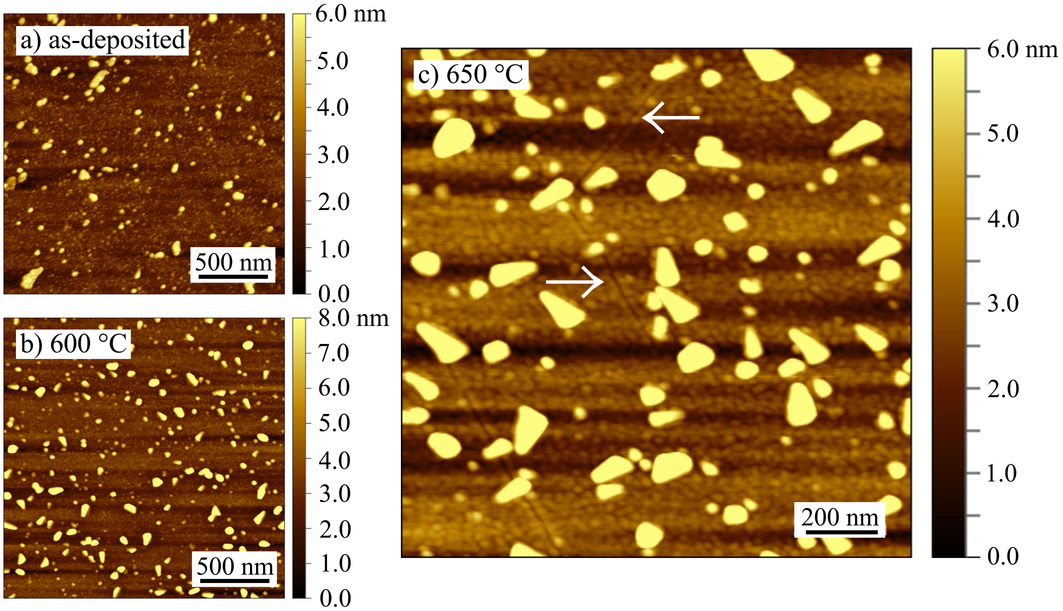

*Figure 48*. Surface morphology of a 14 nm thick TmIG film *a)* as-grown and after annealing for 30 minutes at *b)* 600 °C and *c)* 650 °C.

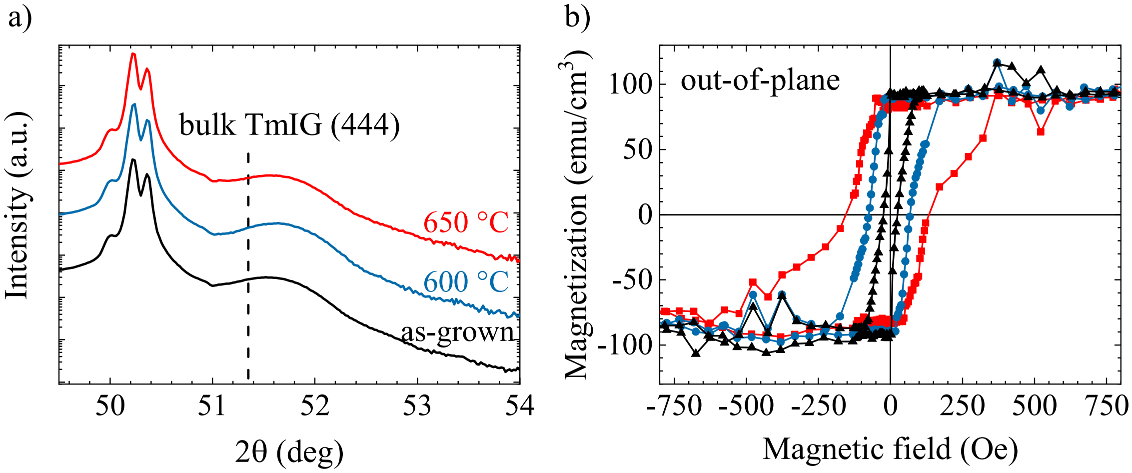

*Figure 49*. Effect of annealing at 600 °C and 650 °C on the *a)* structural and *b)* magnetic properties of TmIG(14 nm)/GSGG.

The effect of the heat treatment on the crystal structure was assessed by investigating the film (444) diffraction peak. XRD patterns of the as-grown film and after annealing are displayed in *Figure 49 (a)*. The as-grown film shows the (444) diffraction peak at a higher $2\theta$ angle than for bulk TmIG which indicates a compressed unit cell in the growth direction. After annealing at 600 °C and 650 °C, no structural changes are visible as the film diffraction peak remains at the same $2\theta$ angle. Considering a constant in-plane tensile strain, the annealed films are expected to maintain the easy axis of magnetization of the as-grown film.

Out-of-plane SQUID-VSM measurements carried out to monitor the effect of annealing on the magnetic properties are displayed in *Figure 49 (b)*. The magnetic easy axis of the as-grown film is along the normal direction implying that the magnetoelastic anisotropy overcomes the shape anisotropy. As expected from the structural characterization, after annealing at 600 °C and 650 °C, the films show perpendicular magnetic anisotropy. The saturation magnetization remains rather constant at around 90 ± 20 emu/cm$^3$. An increased defect density is observed as a function of annealing temperature. The coercive field increases from 25 ± 2 Oe for the as-grown film up to 145 ± 20 Oe for the film annealed at 650 °C in agreement with the changes in film morphology. For the as-grown film, the switching of magnetization when cycling the applied magnetic field takes place via nucleation and fast propagation of magnetic domains as indicated by the sharp transition from positive $M_S$ to negative $M_S$ and vice versa. A similar behavior is also observed for the film annealed at 600 °C. Increasing further the annealing temperature results in an opening of the hysteresis loop at fields larger than $H_c$. The cracks visible on the film surface (*Figure 48 (c)*) could prevent the propagation of magnetic domains leading to the slow change of $M$ with $H$.

Morphological, structural and magnetic investigations of crystalline TmIG films annealed in ambient conditions reveal rather small modifications after a heat treatment for 30 minutes at 600 °C, while considerable changes regarding morphology and magnetic properties are visible for higher annealing temperatures.

### 5.2.4 Annealing of amorphous films

Heat treatments in oxygen and argon atmosphere of amorphous YIG films were reported to lead to epitaxial crystalline layers with low coercivity and Gilbert damping parameter [35,139]. Additionally, YIG films annealed in ambient conditions in a 125 °C temperature range show similar morphology and magnetic properties (see chapter 4.2). In the following, the effect of annealing on amorphous TmIG films is investigated.

*Table 4.* Annealing conditions of amorphous TmIG films.

| Sample name | $T_A$ (°C) | Duration (min) | Heating rate (°C/min) | Comments |
|---|---|---|---|---|
| #1 | 550 | 15 | 2 | No MOKE signal |
| #2 | 600 | | 2 | No MOKE signal |
| #3 | 650 | | 2 | No MOKE signal |
| #4 | 670 | | 1 | |
| #5 | 670 | | 1 | Grown at 500 °C |

15 – 20 nm thick films were grown at room temperature with a 0.01 nm/s growth rate. After deposition, the silver paste used to fix the substrate on the sample holder was removed and the samples were annealed in ambient atmosphere at various temperatures $T_A$ between 550 °C and 670 °C. The annealing conditions are summarized in *Table 4*.

The effect of post-deposition annealing on the film morphology was observed by AFM. Topography images of as-grown and annealed films are summarized in *Figure 50*. After deposition, the films show the terrace-like surface of the substrate and an rms roughness of 0.1 ± 0.1 nm. Films grown at room temperature are amorphous and no magnetic signal was detected via the Kerr effect. Heat treatments at temperatures below 650 °C do not affect the film morphology. Increasing further $T_A$ leads to cracks uniformly distributed on the film surface without a clear crystallographic orientation (*Figure 50 (e)*). Their small lateral size limits the AFM tip in probing the real depth of the cracks which might extend through the entire film thickness. A TmIG film deposited at 500 °C shows no cracks after annealing at 670 °C for 15 minutes (*Figure 50 (f)*).

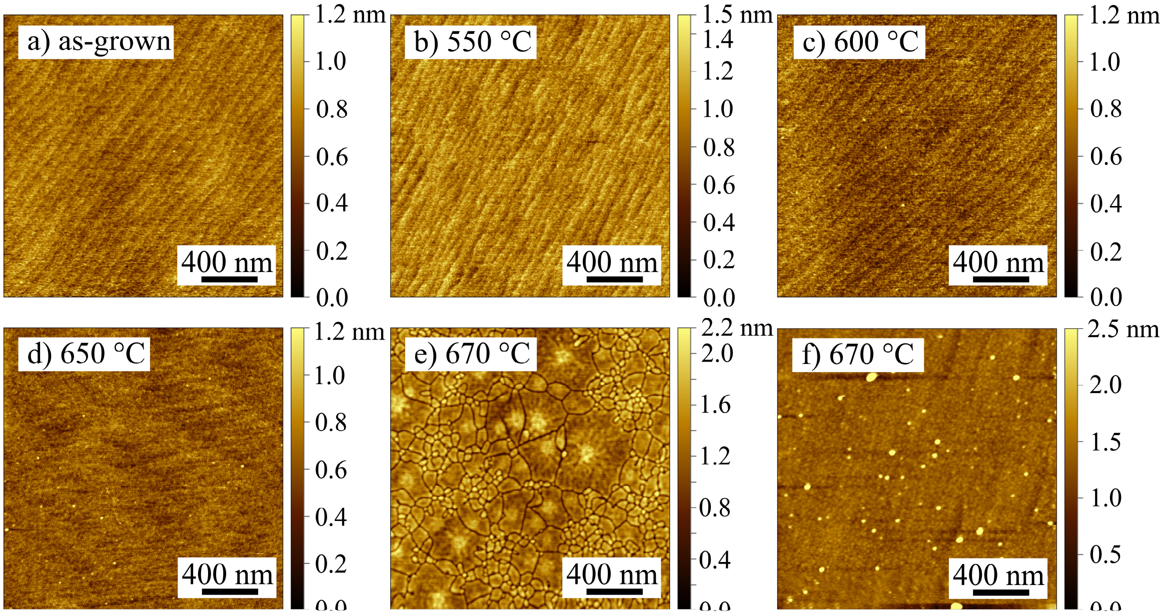

*Figure 50*. Topography images of *a)* as-grown amorphous TmIG films, and *b)–f)* after annealing at various temperatures in ambient conditions. Different scales are used for a better visibility of specific features.

During growth at elevated temperatures, the stress due to the lattice mismatch between bulk material and substrate, and different thermal expansion coefficients of TmIG and GSGG partially relaxes via defects (for example dislocations) as the film grows. On the contrary, there is no stress-relaxation mechanism for films prepared at room temperature. The presence of cracks after the heat treatment at 670 °C indicates a large amount of stress build up in the film during deposition.

Next, crystallographic investigations were carried out to assess the impact of annealing temperature on amorphous TmIG films. For this, an aligning procedure for the substrate (444) diffraction peak was performed. The diffraction patterns of the samples annealed at 650 °C and 670 °C are displayed in *Figure 51 (a)*. Both samples show no clear film diffraction peak. The possibility that the films crystallize in polycrystalline structures was investigated by conducting $\theta - 2\theta$ scans in a broad angle range (20 – 80°) without the alignment to any substrate peak. The patterns in the 44.5 – 55.5° angle range are displayed in *Figure 51 (b)*. The scans contain the substrate (444) reflection peak corresponding to various wavelengths of the incident beam. No diffraction peak is observed in this geometry for the film annealed at 650 °C. MOKE measurements of the samples annealed at $T_A$ below 650 °C showed no magnetic signal confirming that temperatures lower than 650 °C are below the crystallization point. Sample #4 shows the film (444) diffraction peak centered at around $2\theta = 51.41$ ° indicating that the crystallization of amorphous TmIG films starts around 670 °C. No additional film peaks are visible in the scanned angle range indicating a textured growth. The diffraction peak of a film epitaxial to the substrate decreases in intensity similar to the substrate reflection in a misaligned geometrical configuration. The rather intense film peak in *Figure 51 (b)* indicates, depending on the absence or presence of the same reflection in the aligned configuration of *Figure 51 (a)*, the tilt of the film crystal plane away from the normal direction or film mosaicity, respectively. The crystallization of amorphous films at $T_A = 670$ °C implies that the cracks observed in the topography image of film #4 (*Figure 50 (e)*) form when reaching the activation energy of atom movement.

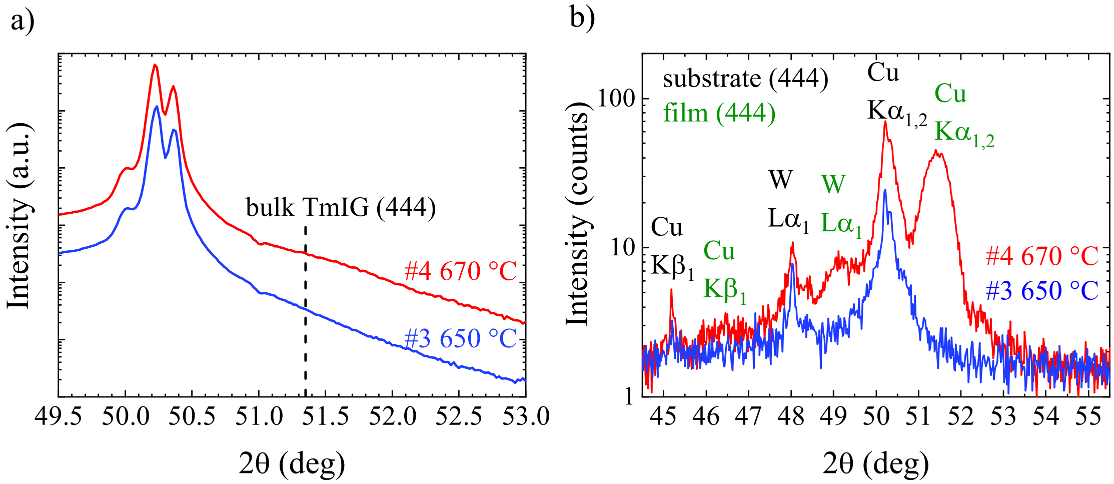

*Figure 51.* Diffraction patterns of the samples annealed at 650 °C and 670 °C measured *a)* aligned to the substrate (444) peak, and *b)* without a system alignment.

The magnetic properties of the films annealed at $T_A = 650$ °C and 670 °C were investigated by SQUID-VSM magnetometry. The oop and ip hysteresis curves of films #3 and #4 are displayed in *Figure 52*. Film #4 annealed at 670 °C shows rather isotropic properties with a similar line shape for the ip and oop hysteresis curves. The rather low magnetization of $50 \pm 20$ emu/cm$^3$ might originate from incomplete crystallization. No magnetic signal is visible for the film annealed at 650 °C after subtracting the substrate contribution (inset of *Figure 52*) implying that amorphous TmIG films are not magnetic.

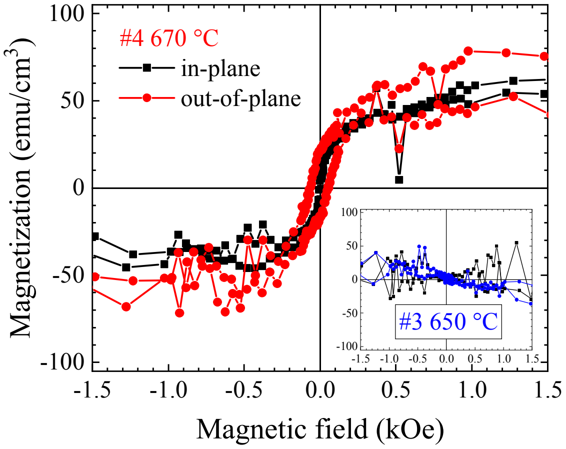

*Figure 52*. In-plane and out-of-plane hysteresis loops of TmIG film #4 annealed at 670 °C. Inset shows the loops of film #3 annealed at 650 °C.

The crystallization of amorphous TmIG films by annealing in ambient conditions is initiated at temperatures above 650 °C. However, due to a large lattice mismatch and different thermal expansion coefficients between the film and substrate, the films show cracks after annealing for periods as short as 15 minutes. Magnetic investigations suggest that higher annealing temperatures are required for complete crystallization. According to these findings, strained TmIG films with high quality surface and an oop easy axis of magnetization cannot be achieved by annealing from initially amorphous structures grown on GSGG(111) substrates.

*Summary*

Strained $Tm_3Fe_5O_{12}$ films with out-of-plane magnetic easy axis were successfully grown on sGGG(111) and GSGG(111) substrates. For thin films grown on both substrates, strain-induced magnetoelastic anisotropy overcomes shape anisotropy and dictates the magnetization direction. Increasing the film thickness leads to a reduction of the strain level and the rotation of the magnetic easy axis towards the film plane. The lattice mismatch between bulk TmIG and the two substrate types strongly affects the relaxation thickness. While 37 nm thick films grown on GSGG are characterized by an ip easy axis of magnetization, films on sGGG substrates show a high level of strain up to 70 nm. Post-deposition annealing of crystalline films was observed to lead to a rather fast deterioration of the magnetic properties. A minor impact was measured only after a 30 minutes heat treatment at a low temperature of 600 °C while cracks appear on the film surface for higher annealing temperatures. Amorphous TmIG films crystallize at higher temperatures (above 670 °C) compared to amorphous YIG layers (600 °C). Different expansion coefficients and a large lattice mismatch between bulk TmIG and the GSGG substrate result in cracks after annealing for 15 minutes at 670 °C. Additionally, magnetic investigations revealed isotropic properties and, possibly, incomplete crystallization at this temperature.

# 6 YIG films grown on strained TmIG layers

$Y_3Fe_5O_{12}$ films grown on GGG(111) substrates show an in-plane easy axis of magnetization due to a small magnetocrystalline anisotropy and dominant shape anisotropy. However, tailoring the magnetic easy axis direction was proven possible. Recently, tensile strain-induced magnetoelastic anisotropy was observed for YIG films grown on $(Gd_{0.63}Y_{2.37})(Sc_2Ga_3)O_{12}$ and $Gd_3Sc_2Ga_3O_{12}$ substrates leading to an oop magnetic easy axis for films thinner than 15 nm [46]. Stress-engineered 20 – 40 nm thick YIG films sandwiched between a buffer and a cover layer revealed a suppressed in-plane strain relaxation. In the following, the magnetic easy axis of YIG films grown on thin TmIG layers is studied.

YIG and TmIG films are optimally grown with different deposition parameters. Therefore, for this study, three 15 nm thick TmIG films were prepared at optimal conditions (0.01 nm/s deposition rate, $5 \cdot 10^{-4}$ mbar oxygen pressure, and 570 °C substrate temperature) on GSGG(111) substrates. The films were cooled down with a -5 °C/min rate and, without breaking the vacuum, 5 – 20 nm thick YIG films were deposited at room temperature. After deposition, the samples were annealed in ambient conditions at 600 °C for 30 minutes. This temperature ensures the crystallization of the YIG film (*Figure 34*) with a minimal impact on the TmIG layer (see *Figure 49*).

Topography images of the as-grown bilayers are displayed in *Figure 53 (a)*. After deposition, all bilayers show continuous, smooth surfaces. Terrace-like features are visible on the surface of YIG(5 nm)/TmIG/GSGG. In this case, a roughness of 0.2 ± 0.1 nm is extracted from the scanned window. Faint terraces are also visible for YIG(20 nm)/TmIG/GSGG with a slight increase of the roughness to 0.3 ± 0.1 nm. The surface of YIG(10 nm)/TmIG/GSGG is covered with small grains leading to the highest roughness of the series of 0.4 ± 0.1 nm.

The crystallinity of the TmIG films before the heat treatment was confirmed by XRD. *Figure 54 (a)* displays the $\theta - 2\theta$ scans of the samples measured around the substrate (444) reflection peak. The samples show film peaks at $2\theta$ angles that are larger than for bulk TmIG; therefore, all TmIG films are grown under in-plane tensile strain. The similarity in line shape of the diffraction patterns points to the amorphous nature of the YIG films with a contribution only from the crystalline TmIG underlayer. Additionally, the presence of the film peak at the same $2\theta$ angles indicates that all TmIG films exhibit similar level of in-plane tensile strain. According to previous investigations, TmIG films with this level of strain have an out-of-plane magnetic easy axis. Polar MOKE measurements displayed in *Figure 54 (b)* confirm the magnetic easy axis direction. After deposition, all TmIG films show rather square hysteresis loops with coercive fields below 150 Oe. A change of coercivity is visible through the series in agreement with the film morphology. YIG(5 nm)/TmIG/GSGG, with the best surface quality, is characterized by the smallest $H_c$ of 28 ± 5 Oe, while for YIG(10 nm)/TmIG/GSGG, with the highest roughness of the series, $H_c = 145 \pm 10$ Oe. Please note that the reverse direction of the hysteresis loops (negative magnetization at positive magnetic fields) originates from the negative Kerr rotation at the used laser wavelength (see *Figure 18*).

a) as-deposited

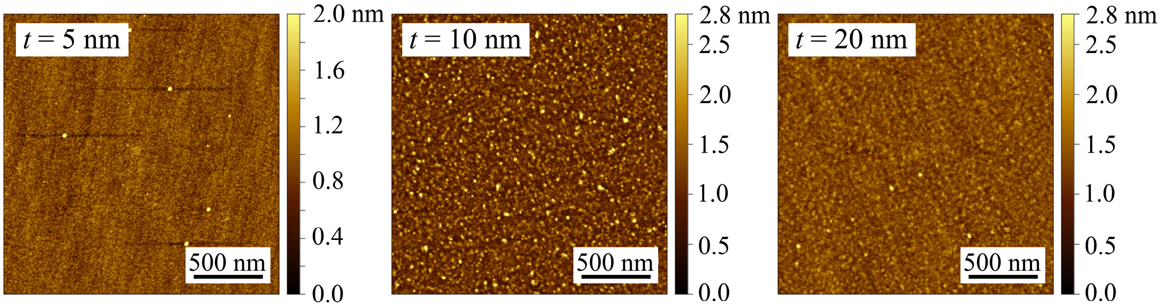

b) after annealing

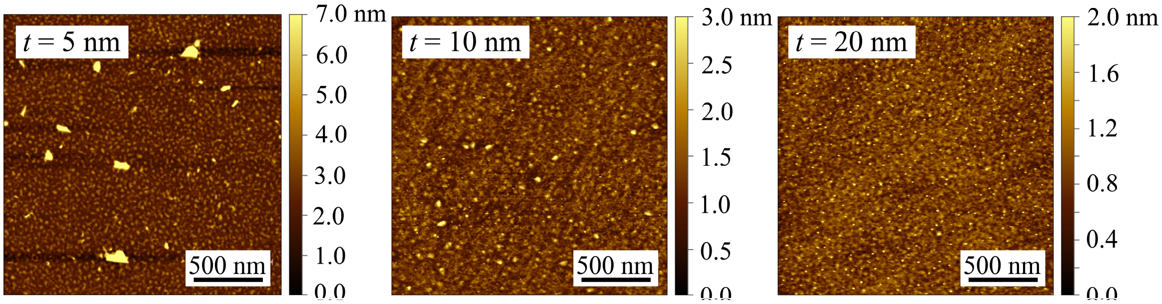

*Figure 53.* Surface morphology of YIG(*t*)/TmIG(15 nm)/GSGG *a)* before and *b*) after annealing at 600 °C for 30 minutes in ambient atmosphere. Different scales are used for a better visibility of specific features.

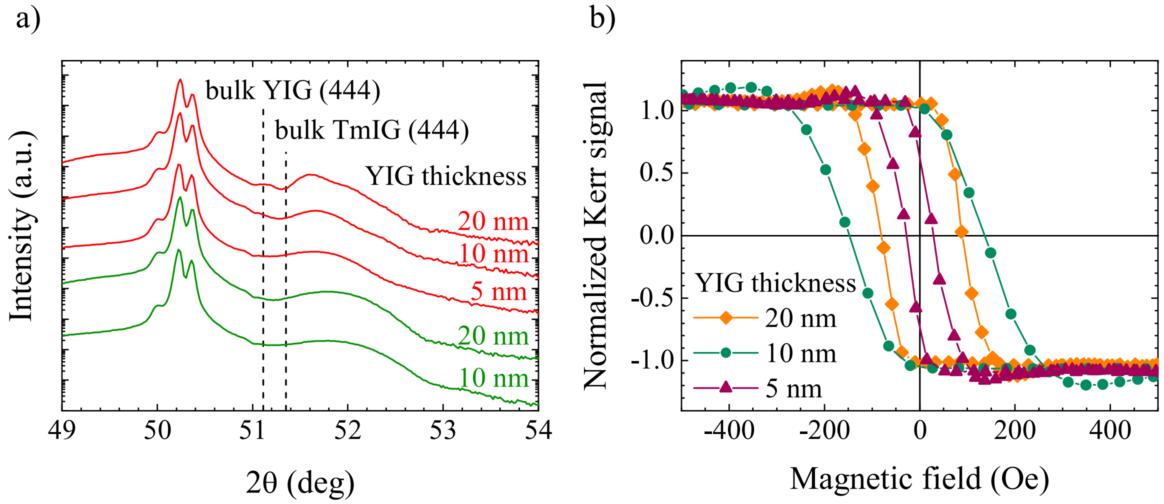

*Figure 54.* *a)* Diffraction patterns of YIG(*t*)/TmIG(15 nm)/GSGG before (green) and after (red) the heat treatment. The diffractograms are shifted on the *y* axis for a better visibility. *b)* Polar MOKE hysteresis curves of YIG(*t*)/TmIG(15 nm)/GSGG before annealing.

After the heat treatment, a decrease of surface quality is apparent for YIG(5 nm)/TmIG/GSGG (*Figure 53 (b)*). 15 nm high and 100 nm wide defects are visible on the film surface. After annealing, the film surface is covered with 1 – 2 nm tall grains that result in an rms roughness of 0.7 ± 0.1 nm (not considering the large defects). The effect of annealing for the other samples is rather minor. No morphologic changes are visible after the heat treatment and, in both cases, the rms roughness remains below 0.4 ± 0.1 nm.

Crystallographic investigations reveal structural changes after the heat treatment (*Figure 54 (a)*). YIG(5 nm)/TmIG/GSGG shows one reflection peak corresponding to the garnet films. Therefore, in the growth direction, a similar unit cell characterizes the two garnet films. The diffraction peak at a slightly lower $2\theta$ angle compared to the as-grown TmIG film indicates a slight relaxation of the in-plane tensile strain. The scans of the thicker samples show two diffraction peaks corresponding to different levels of in-plane tensile strain. The position of the reflection centered at larger $2\theta$ angle closely matches the TmIG film before annealing. The peak visible at lower $2\theta$ angle is expected to originate from the surface since its full width at half maximum decreases and it slightly shifts towards lower angles with increasing the YIG layer thickness. Thus, a strain gradient is observed through the overall film thickness.

A chemical analysis of the film surface after the heat treatment was conducted in collaboration with O. Selyshchev from TU Chemnitz, Germany. X-ray photoemission spectroscopy (XPS) studies carried out with a monochromatized Al X-ray source are displayed in *Figure 55*. The spectrum of a 300 nm thick TmIG film on sGGG substrate is shown for comparison. All bilayers systems show the Y 3d peak originating from the top YIG film. The absence of the Tm 4d peak for all bilayers, and especially for the sample with the thinnest YIG layer, indicates a very weak or no inter-layer diffusion.

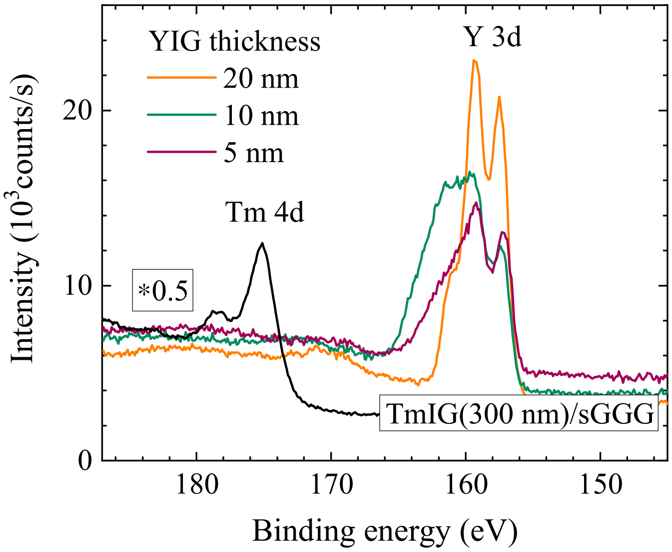

*Figure 55.* XPS spectra of YIG($t$)/TmIG(15 nm)/GSGG after the heat treatment, and of a 300 nm thick TmIG film deposited on sGGG(111) substrate. For a better visibility, the spectrum of TmIG(300 nm)/sGGG is multiplied by 0.5. The position of Tm 4d and Y 3d peaks are indicated.

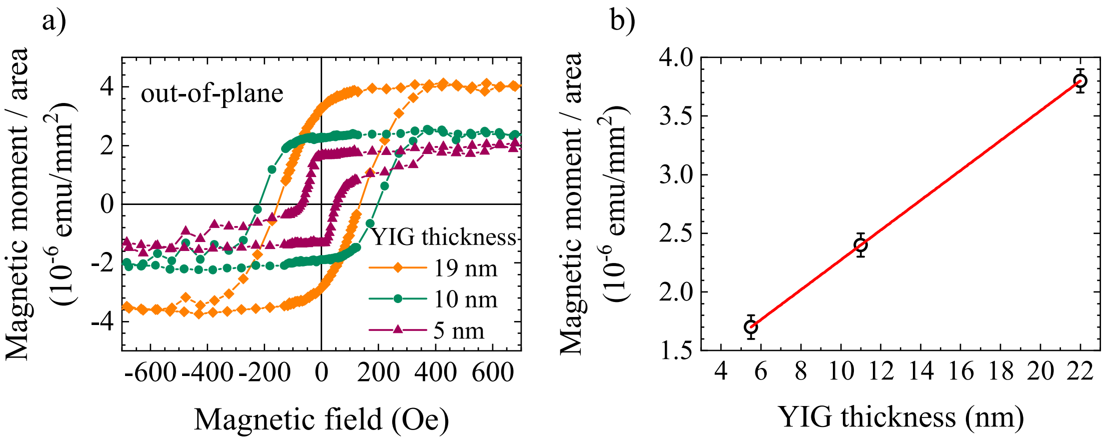

*Figure 56.* *a)* Hysteresis loops of YIG(*t*)/TmIG(15 nm)/GSGG measured in out-of-plane geometry and represented as magnetic moment per area. *b)* Dependence of the magnetic moment of the bilayers on YIG film thickness. Red curve represents the linear fit of the experimental data (symbols).

The film thicknesses after the heat treatment were estimated from ellipsometry measurements. Ellipsometry spectra of the bilayers measured at three incident angles were fitted using the dielectric functions of YIG and GGG, as described previously. Due to the similar optical properties of YIG and TmIG, the model was build considering one thin film with a total thickness given by the two garnet layers. Total film thicknesses of 16 nm (20 nm), 22 nm (25 nm), and 32 nm (35 nm) were extracted for the three bilayers systems. The values in the brackets indicate nominal thicknesses. Therefore, the thickness values of the YIG layers were estimated to be 5.5 nm, 11 nm, and 22 nm for the three bilayers systems.

The magnetic properties after the heat treatment were investigated from hysteresis loops measured with the magnetic field applied in out-of-plane and in-plane directions. The effect of the YIG film thickness on the magnetic moment of the bilayers is illustrated in *Figure 56*. Saturation values of the magnetic moment extracted from the oop hysteresis curves are summarized in *Figure 56 (b)*. A linear increase of the magnetic moment of the bilayers is observed with increasing the YIG film thickness. Please note that in *Figure 56 (b)* the YIG thickness values obtained from ellipsometry measurements were used. For a TmIG thickness of 11 nm estimated from ellipsometry measurements, a magnetization of around 90 ± 20 emu/cm$^3$ was obtained for the TmIG layer by extrapolating the linear fit of the experimental data (represented with a red curve in *Figure 56 (b)*).

*Figure 57* displays the oop and ip hysteresis loops of the bilayers after subtracting the substrate contribution. After the heat treatment, all films show squared oop hysteresis loops while in the ip direction a slow linear increase of the magnetization towards saturation is observed. For all bilayers, the magnetoelastic anisotropy overcomes the shape anisotropy and the films show an oop easy axis of magnetization. Throughout the series, the saturation magnetization remains constant at around 110 ± 10 emu/cm$^3$ corresponding to a magnetization of about 127 ± 10 emu/cm$^3$ for the YIG films. Despite the increased number of surface defects after the heat treatment, YIG(5 nm)/TmIG/GSGG shows the lowest coercivity of 60 ± 5 Oe. The variation of coercivity through the series follows the film quality after deposition with the highest $H_c$ of 210 ± 20 Oe measured for the 10 nm thick YIG film. Due to the heat treatment, $H_c$ increases on average by 45 Oe.

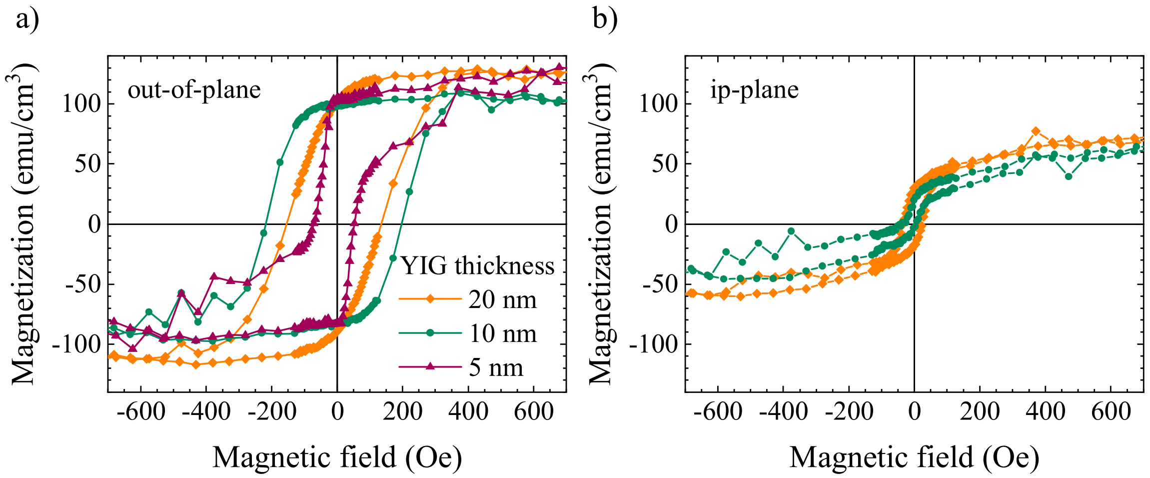

*Figure 57.* *a)* Out-of-plane and *b)* in-plane hysteresis loops of YIG(*t*)/TmIG(15 nm)/GSGG after the heat treatment. The experimental data was corrected for the substrate contribution.

In summary, YIG films grown at room temperature on TmIG(15 nm)/GSGG and annealed in ambient atmosphere at 600 °C for 30 minutes show in-plane tensile strain. Chemical analysis of the bilayers after the heat treatment reveals no apparent intermixing of the two garnet films. Magnetic investigations show that YIG films up to 20 nm thickness have an out-of-plane easy axis of magnetization.

# 7 Summary and outlook

In this thesis, properties of yttrium and thulium iron garnet thin films were investigated with the purpose of integrating garnet films in spin wave studies. The impact of growth conditions, substrate type, film thickness, and post-deposition annealing treatments was studied with a focus on the film morphology, crystal structure, and static and dynamic magnetic properties.

The thin films investigated in this work were grown by pulsed laser deposition on single crystal substrates. Smooth layers with the desired stoichiometry and structure require the optimization of numerous growth conditions. Therefore, as a first step, the identification of the optimal growth conditions for YIG and TmIG thin films was carried out. The oxygen pressure at which stoichiometric films are deposited was identified from chemical analysis carried out for films grown on silicon substrates. Stoichiometric films were grown at low oxygen pressure ($5\cdot10^{-4}$ mbar and 0.04 mbar for TmIG films, and $5\cdot10^{-4}$ mbar and 0.03 mbar for YIG films) while increasing the oxygen pressure resulted in rare-earth ions enrichment. On the example of TmIG films grown on GSGG(111) substrates, it was shown that epitaxial films with smooth surface and low coercivity can be achieved at low growth rates (< 0.04 nm/s) in combination with moderate substrate temperatures (below 700 °C). The following discussions focused on the individual properties of YIG and TmIG films with the purpose of integrating both films in garnet heterostructures.

YIG films deposited at optimal growth conditions on lattice-matching GGG(111) substrates show very good morphologic and magnetic properties. Terrace-like features or sinusoidal structures of the substrate surface are observed in the topography images of films as thick as 100 nm. As a consequence of the dominant magnetic shape anisotropy, YIG films on GGG substrates show an in-plane easy axis of magnetization. The high quality of the films is also indicated by the extremely low coercivity (below 1 Oe) measured for an 18 nm thick film.

The growth of films with the desired properties requires time consuming optimization steps, and the window of optimal deposition parameters is rather limited. Therefore, the crystallization of amorphous 30 nm thick YIG films via post-deposition annealing was investigated. For this, heat treatments for 30 minutes in ambient atmosphere were carried out in a broad temperature range (550 – 775 °C). YIG films grown at room temperature are amorphous and show no magnetic order. From the investigation of magnetic properties of annealed films, it was observed that the crystallization is initiated at temperatures as low as 550 °C, but the expected magnetic order is obtained for temperatures above 600 °C. Morphologic and magnetic studies revealed a broad temperature window of 125 °C for which the annealed films show similar properties. Smooth surfaces characterized by rms roughness values below 0.6 nm, very low coercivity of < 1 Oe, and 100% remanence were observed for all films annealed in this temperature window. Crystallographic studies conducted on the film annealed at 650 °C revealed a high crystal quality. In the growth direction, the film shows a unit cell similar to the GGG substrate. Increasing the annealing time and/or film thickness leads to film cracking. Nevertheless, the reported results prove the large flexibility of growing epitaxial YIG films on structured substrates at elevated temperatures or crystallized from amorphous state via annealing in ambient atmosphere.

While YIG films grown on lattice-matching substrates have an in-plane easy axis of magnetization due to the dominant shape anisotropy, sufficiently strong induced-magnetoelastic anisotropy can orient the film magnetization in the normal direction. Due to a rather large magnetostriction constant, $Tm_3Fe_5O_{12}$ films were grown on substrates with different levels of lattice mismatch (substituted-$Gd_3Ga_5O_{12}$ with $\Delta = 1.45$ % and $Gd_3Sc_2Ga_3O_{12}$ with $\Delta = 1.84$ %). Crystallographic studies of thin TmIG films reveal the compression of the unit cell in the growth direction and a strong distortion of the film lattice. At reduced thicknesses, the magnetoelastic anisotropy induced by in-plane tensile strain is dominant and the films have an out-of-plane magnetic easy axis. It was observed that with increasing the film thickness the crystal structure relaxes towards the bulk cubic lattice. As a consequence, the magnetic easy axis direction rotates towards the sample plane due to the dominant magnetic shape anisotropy. The structural relaxation dependents on the lattice mismatch between bulk TmIG and the substrate. 70 nm thick films on sGGG(111) substrates show a high level of tensile strain, however, an in-plane easy axis of magnetization was observed for TmIG(37 nm)/GSGG. Therefore, the magnetic properties of TmIG films can easily be tuned via the substrate type and film thickness. FMR studies revealed uniaxial anisotropy values $K_u$ in the $90 - 110$ kerg/cm$^3$ range, close to the values extracted from the $M - H$ hysteresis curves. A Gilbert damping of 0.02, which remains rather constant through the thickness series, was additionally extracted from the FMR measurements. The values obtained for TmIG films are around two orders of magnitude larger than for YIG layers due to a stronger spin-orbit coupling for the former case.

Based on the successful crystallization of amorphous YIG films, heat treatments were also carried out on amorphous TmIG films grown at room temperature. Structural investigations revealed that the crystallization starts at temperatures between 650 °C and 670 °C. The large lattice mismatch and the difference between the thermal expansion coefficients of the film and the substrate lead to cracks after annealing times as short as 15 minutes. Hysteresis curves measured in out-of-plane and in-plane geometries reveal isotropic magnetic properties and a reduced saturation magnetization pointing to an incomplete crystallization after annealing at 670 °C for 15 minutes. Therefore, TmIG films with perpendicular magnetic anisotropy are not obtained by crystallization from an initially amorphous state when deposited on GSGG(111) substrates.

The optimal growth conditions, especially the substrate temperature, differ for the two types of garnet films investigated in this work. The possibility of obtaining perpendicular magnetic anisotropy in YIG films was investigated for amorphous films grown on crystalline TmIG underlayers. YIG films of thicknesses between 5 nm and 20 nm were deposited at room temperature on 15 nm thick TmIG films. The crystallization of the top layer was achieved by carrying out a heat treatment in ambient atmosphere at 600 °C for 30 minutes. Studies of post-deposition annealing of crystalline TmIG films showed a rather small impact of annealing in these conditions on the film morphology, structural and magnetic properties. Crystallographic studies on YIG($t$)/TmIG(15 nm)/GSGG before and after the heat treatment showed structural modifications confirming the crystallization of the top YIG layer. Chemical analysis of the film surface carried out after the heat treatment revealed no or very weak layer intermixing. All bilayers systems show an out-of-plane easy axis of magnetization, a constant saturation magnetization of around $110 \pm 10$ emu/cm$^3$, and rather low coercivities below 200 Oe.

Therefore, 5 – 20 nm thick YIG films with perpendicular magnetic anisotropy can successfully be grown on strained TmIG layers.

The investigations carried out on YIG and TmIG films reveal a broad range of growth conditions and the possibility of tuning the morphologic, structural and magnetic properties for the desired application. In the following a discussion of future research directions is presented.

Periodical structures patterned on GGG substrates are still visible after the growth of 100 nm thick YIG films indicating a modulation of the garnet layer. The formation of spin wave band structures was already predicted theoretically and proven experimentally in magnonic crystals and homogeneous ferromagnetic films covered by metallic stripes [145]. Investigations of spin dynamics in wave-like structured garnets could also be of interest for magnonics. The material property influencing strongly the spin wave propagation length is the Gilbert damping $\alpha$. Therefore, the effect of the film modulation on the extremely low $\alpha$ value of YIG could also be investigated.

Epitaxial TmIG films with perpendicular magnetic anisotropy obtained by annealing from amorphous structures could be of practical interest as a more efficient fabrication method. For this, substrates with a smaller lattice mismatch (for example substituted-$Gd_3Ga_5O_{12}$ or $Y_3Sc_2Ga_3O_5$) should be considered.

Additionally to the observed effect of the substrate type and film thickness on the structure of strained TmIG films, the stoichiometry also impacts the lattice and, therefore, can represent an additional source of strain. Tuning of the strain relaxation thickness could be achieved via the oxygen pressure during deposition. Controlling the magnetic easy axis of garnet films via substrate type and film thickness is of fundamental interest. A few prospect investigation directions could be the study of magnetization switching via femtosecond long optical pulses, an effect widely observed in rare-earth-based ferrimagnets [146] but not investigated yet in ferrimagnetic insulators, or by the damping-like component of the spin-orbit torque [41].

The results of this work open new material and application oriented research which could be the aim of future works.

# 8 References

1. Baibich, M. N. *et al.* Giant magnetoresistance of (001)Fe/(001)Cr magnetic superlattices. *Phys. Rev. Lett.* **61**, 2472 (1988).
2. Binasch, G., Grünberg, P., Saurenbach, F. & Zinn, W. Enhanced magnetoresistance in layered magnetic structures with antiferromagnetic interlayer exchange. *Phys. Rev. B* **39**, 4828 (1989).
3. Julliere, M. Tunneling between ferromagnetic films. *Phys. Lett. A* **54**, 225 (1975).
4. Dieny, B. *et al.* Magnetotransport properties of magnetically soft spin-valve structures (invited). *J. Appl. Phys.* **69**, 4774 (1991).
5. Miyazaki, T., Yaoi, T. & Ishio, S. Large magnetoresistance effect in 82Ni-Fe/Al-Al2O3/Co magnetic tunneling junction. *J. Magn. Magn. Mater.* **98**, L7 (1991).
6. Parkin, S. S. P. *et al.* Giant tunnelling magnetoresistance at room temperature with MgO (100) tunnel barriers. *Nat. Mater.* **3**, 862 (2004).
7. Bhatti, S. *et al.* Spintronics based random access memory: a review. *Mater. Today* **20**, 530 (2017).
8. Prejbeanu, I. L. *et al.* Thermally assisted MRAM. *J. Phys. Condens. Matter* **19**, 165218 (2007).
9. Slonczewski, J. C. Current-driven excitation of magnetic multilayers. *J. Magn. Magn. Mater.* **159**, L1 (1996).
10. Kelly, D., Wegrowe, J. E., Truong, T. kha, Hoffer, X. & Ansermet, J. P. Spin-polarized current-induced magnetization reversal in single nanowires. *Phys. Rev. B* **68**, 134425 (2003).
11. Liu, C. *et al.* Long-distance propagation of short-wavelength spin waves. *Nat. Commun.* **9**, 738 (2018).
12. Seki, S. *et al.* Propagation dynamics of spin excitations along skyrmion strings. *Nat. Commun.* **11**, 256 (2020).
13. Khitun, A., Bao, M. & Wang, K. L. Magnonic logic circuits. *J. Phys. D. Appl. Phys.* **43**, 264005 (2010).
14. Pirro, P. *et al.* Spin-wave excitation and propagation in microstructured waveguides of yttrium iron garnet/Pt bilayers. *Appl. Phys. Lett.* **104**, 012402 (2014).
15. Demidov, V. E. *et al.* Transformation of propagating spin-wave modes in microscopic waveguides with variable width. *Phys. Rev. B - Condens. Matter Mater. Phys.* **79**, 054417 (2009).
16. Vogt, K. *et al.* Spin waves turning a corner. *Appl. Phys. Lett.* **101**, 042410 (2012).
17. Qin, H., Hämäläinen, S. J., Arjas, K., Witteveen, J. & Van Dijken, S. Propagating spin waves in nanometer-thick yttrium iron garnet films: Dependence on wave vector, magnetic field strength, and angle. *Phys. Rev. B* **98**, 224422 (2018).

18. Hansen, P. Magnetic anisotropy and magnetostriction in garnets. in *Physics of Magnetic Garnets* (ed. Paoletti, A.) pages 63-75 (North-Holland, 1978).

19. Momma, K. & Izumi, F. VESTA 3 for three-dimensional vizualization of crystal, volumetric and morphology data. *J. Appl. Crystallogr.* **44**, 1272 (2011).

20. Mueller, U. *International Tables for Crystallography Volume A: Space-group symmetry*. (Wiley, 2016).

21. Geller, S., Williams, H. J. & Sherwood, R. C. Magnetic and crystallographic study of neodymium-substituted yttrium and gadolinium iron garnets. *Phys. Rev.* **123**, 1692 (1961).

22. Espinosa, G. P. Crystal chemical study of the rare-earth iron garnets. *J. Chem. Phys.* **37**, 2344 (1962).

23. Geller, S. Crystal and static magnetic properties of garnets. in *Physics of Magnetic Garnets* (ed. Paoletti, A.) pages 2-23 (North-Holland, 1978).

24. Belov, K. P., Talalaeva, E. V & Yarkho, G. A. Magnetic properties of rare-earth iron garnets in the Curie-point region. *Sov. Phys. JETP* **25**, 989 (1967).

25. Spencer, G., Lecraw, R. C. & Clogston, A. M. Low-temperature line-width maximum in yttrium iron garnet. *Phys. Rev. Lett.* **3**, 32 (1959).

26. Spencer, E. G. & LeCraw, R. C. Ferromagnetic relaxation in yttrium-iron garnet and the relation to applications. *Proc. IEE - Part B Electron. Commun. Eng.* **109**, 66 (1962).

27. Henry, R. D., Besser, P. J., Heinz, D. M. & Mee, J. E. Ferromagnetic resonance properties of LPE YIG films. *IEEE Trans. Magn.* **MAG-9**, 535 (1973).

28. Sethares, J. C. Magnetostatic wave devices and applications (invited). *J. Appl. Phys.* **53**, 2646 (1982).

29. Ishak, W. S. Magnetostatic wave technology: a review. *Proc. IEEE* **76**, 171 (1988).

30. Tang, C. *et al.* Exquisite growth control and magnetic properties of yttrium iron garnet thin films. *Appl. Phys. Lett.* **108**, 102403 (2016).

31. Onbasli, M. C. *et al.* Pulsed laser deposition of epitaxial yttrium iron garnet films with low Gilbert damping and bulk-like magnetization. *APL. Mat.* **2**, 106102 (2014).

32. Stognij, A. I. *et al.* Growth of Y3Fe5O12 films on Si with AlOx and SiO2 buffer layers by ion beam sputtering. *Inorg. Mater.* **53**, 1069 (2017).

33. Krockenberger, Y. *et al.* Layer-by-layer growth and magnetic properties of Y3Fe5O12 thin films on Gd3Ga5O12. *J. Appl. Phys.* **106**, 123911 (2009).

34. Jungfleisch, M. B. *et al.* Thickness and power dependence of the spin-pumping effect in Y3Fe5O12/Pt heterostructures measured by the inverse spin Hall effect. *Phys. Rev. B* **91**, 134407 (2013).

35. Hauser, C. *et al.* Yttrium iron garnet thin films with very low damping obtained by recrystallization of amorphous material. *Sci. Rep.* **6**, 20827 (2016).

36. Kajiwara, Y. *et al.* Transmission of electrical signals by spin-wave interconversion in a

magnetic insulator. *Nat. Lett.* **464**, 262 (2010).

37. Kikkawa, T. *et al.* Longitudinal spin Seebeck effect free from the proximity Nernst effect. *Phys. Rev. Lett.* **110**, 067207 (2013).

38. Collet, M. *et al.* Generation of coherent spin-wave modes in yttrium iron garnet microdiscs by spin-orbit torque. *Nat. Commun.* **7**, 10377 (2016).

39. Förster, J. *et al.* Nanoscale X-ray imaging of spin dynamics in yttrium iron garnet. *J. Appl. Phys.* **126**, 173909 (2019).

40. Serga, A. A., Demokritov, S. O., Hillebrands, B. & Slavin, A. N. Self-generation of two-dimensional spin-wave bullets. *Phys. Rev. Lett.* **92**, 117203 (2004).

41. Li, P. *et al.* Spin-orbit torque-assisted switching in magnetic insulator thin films with perpendicular magnetic anisotropy. *Nat. Commun.* **7**, 12688 (2016).

42. Ding, S. *et al.* Interfacial Dzyaloshinskii-Moriya interaction and chiral magnetic textures in a ferrimagnetic insulator. *Phys. Rev. B* **100**, 100406(R) (2019).

43. Kubota, M. *et al.* Systematic control of stress-induced anisotropy in pseudomorphic iron garnet thin films. *J. Magn. Magn. Mater.* **339**, 63 (2013).

44. Popova, E. *et al.* Structure and magnetic properties of yttrium–iron–garnet thin films prepared by laser deposition. *J. Appl. Phys.* **90**, 1422 (2001).

45. Popova, E. *et al.* Perpendicular magnetic anisotropy in ultrathin yttrium iron garnet films prepared by pulsed laser deposition technique. *J. Vac. Sci. Technol.* **19**, 2567 (2001).

46. Li, G. *et al.* Tunable perpendicular magnetic anisotropy in epitaxial Y3Fe5O12 films. *APL Mater.* **7**, 041104 (2019).

47. Fu, J. *et al.* Epitaxial growth of Y3Fe5O12 thin films with perpendicular magnetic anisotropy. *Appl. Phys. Lett.* **110**, 202403 (2017).

48. Soumah, L. *et al.* Ultra-low damping insulating magnetic thin films get perpendicular. *Nat. Commun.* **9**, 3355 (2018).

49. Kubota, M. *et al.* Stress-induced perpendicular magnetization in epitaxial iron garnet thin films. *App. Phys. Exp.* **5**, 103002 (2012).

50. Kumar, N. *et al.* Epitaxial growth of terbium iron garnet thin films with out-of-plane axis of magnetization. *Thin Solid Films* **516**, 7753 (2008).

51. Shao, Q. *et al.* Exploring interfacial exchange coupling and sublattice effect in heavy metal/ferrimagnetic insulator heterostructures using Hall measurements, x-ray magnetic circular dichroism, and neutron reflectometry. *Phys. Rev. B* **99**, 104401 (2019).

52. Tang, C. *et al.* Anomalous Hall hysteresis in Tm3Fe5O12/Pt with strain-induced perpendicular magnetic anisotropy. *Phys. Rev. B* **94**, 140403(R) (2016).

53. Ahmed, A. S. *et al.* Spin-Hall topological Hall effect in highly tunable Pt/ferrimagnetic-insulator bilayers. *Nano Lett.* **19**, 5683 (2019).

54. Avci, C. O. *et al.* Current-induced switching in a magnetic insulator. *Nat. Mater.* **16**, 309 (2016).

55. Quindeau, A. *et al.* Tm3Fe5O12/Pt heterostructures with perpendicular magnetic anisotropy for spintronic applications. *Adv. Electron. Mater.* **3**, 1600376 (2017).

56. Wu, C. N. *et al.* High-quality thulium iron garnet films with tunable perpendicular magnetic anisotropy by off-axis sputtering – correlation between magnetic properties and film strain. *Sci. Rep.* **8**, 11087 (2018).

57. Chumak, A. V., Vasyuchka, V. I., Serga, A. A. & Hillebrands, B. Magnon spintronics. *Nat. Phys.* **11**, 453 (2015).

58. Stancil, D. D. & Prabhakar, A. *Spin Waves: Theory and Applications*. (Spinger, 2009).

59. Madami, M. *et al.* Direct observation of a propagating spin wave induced by spin-transfer torque. *Nat. Nanotechnol.* **6**, 635 (2011).

60. van Kampen, M. *et al.* All-optical probe of coherent spin waves. *Phys. Rev. Lett.* **88**, 227201 (2002).

61. Demidov, V. E. *et al.* Excitation of microwaveguide modes by a stripe antenna. *Appl. Phys. Lett.* **95**, 112509 (2009).

62. Haldar, A., Kumar, D. & Adeyeye, A. O. A reconfigurable waveguide for energy-efficient transmission and local manipulation of information in a nanomagnetic device. *Nat. Nanotechnol.* **11**, 437 (2016).

63. Sebastian, T., Schultheiss, K., Obry, B., Hillebrands, B. & Schultheiss, H. Micro-focused Brillouin light scattering: imaging spin waves at the nanoscale. *Front. Phys.* **3**, 35 (2015).

64. Liensberger, L. *et al.* Spin-wave propagation in metallic Co25Fe75 films determined by microfocused frequency-resolved magneto-optic Kerr effect. *IEEE Magn. Lett.* **10**, 5503905 (2019).

65. Chumak, A. V. Magnon Spintronics: Fundamentals of Magnon-based Computing. in *Spintronics Handbook, Second Edition: Spin Transport and Magnetism* (eds. Tsymbal, E. Y. & Žutić, I.) (CRC Press, 2019).

66. Wagner, K. *et al.* Magnetic domain walls as reconfigurable spin-wave nanochannels. *Nat. Nanotechnol.* **11**, 432 (2016).

67. Schneider, T. *et al.* Realization of spin-wave logic gates. *Appl. Phys. Lett.* **92**, 022505 (2008).

68. Zhao, Y. *et al.* Experimental investigation of temperature-dependent Gilbert Damping in permalloy thin films. *Sci. Rep.* **6**, 22890 (2016).

69. Conca, A. *et al.* Low spin-wave damping in amorphous Co40Fe40B20 thin films. *J. Appl. Phys.* **113**, 213909 (2013).

70. Kubota, T. *et al.* Half-metallicity and Gilbert damping constant in Co2FexMn1-xSi Heusler alloys depending on the film composition. *Appl. Phys. Lett.* **94**, 122504 (2009).

71. Martín-García, L. *et al.* Memory effect and magnetocrystalline anisotropy impact on the surface magnetic domains of magnetite(001). *Sci. Rep.* **8**, 5991 (2018).

72. Stöhr, J. & Siegmann, H. C. *Magnetism: From Fundamentals to Nanoscale Dynamics*.

(Spinger, 2006).

73. Mee, J. E., Pulliam, G. R., Archer, J. L. & Besser, P. J. Magnetic oxide films. *IEEE Trans. Magn.* **MAG-5**, 717 (1969).

74. Heinz, D. M., Besser, P. J., Owens, J. M., Mee, J. E. & Pulliam, G. R. Mobile cylindrical magnetic domains in epitaxial garnet films. *J. Appl. Phys.* **42**, 1243 (1971).

75. Dijkkamp, D. *et al.* Preparation of Y-Ba-Cu oxide superconductor thin films using pulsed laser evaporation from high Tc bulk material. *Appl. Phys. Lett.* **51**, 619 (1987).

76. Willmott, P. R. *et al.* In situ diffraction studies of the initial growth processes of textured icosahedral quasicrystalline thin films. *Phys. Rev. B* **71**, 094203 (2005).

77. Li, Z. F., Yang, Z. Y. & Xiao, R. F. Pulsed laser deposition of hydrogenated amorphous diamond-like carbon films from a polymer target. *J. Appl. Phys.* **80**, 5398 (1996).

78. Rong, F. X. Liquid target pulsed laser deposition. *Appl. Phys. Lett.* **67**, 1022 (1995).

79. Kushner, M. J. *Nonequilibrium Processes in Partially Ionized Gases*. (Springer US, 1990).

80. Eichler, H. J., Eichler, J. & Lux, O. *Laser: Basics, Advances and Applications*. (Spinger Nature Switzerland AG, 2018).

81. Gamaly, E. G., Rode, A. V. & Luther-Davies, B. *Pulsed Laser Deposition of Thin Films*. *Wiley* (2001).

82. Ono, S. Thermalization in simple metals: Role of electron-phonon and phonon-phonon scattering. *Phys. Rev. B* **97**, 054310 (2018).

83. Singh, R. K. & Narayan, J. A novel method for simulating laser-solid interactions in semiconductors and layered structures. *Mater. Sci. Eng. B* **3**, 217 (1989).

84. Gamaly, E. G., Rode, A. V., Luther-Davies, B. & Tikhonchuk, V. T. Ablation of solids by femtosecond lasers: Ablation mechanism and ablation thresholds for metals and dielectrics. *Phys. Plasmas* **9**, 949 (2002).

85. Singh, R. K. & Narayan, J. Pulsed-laser evaporation technique for deposition of thin films: Physics and theoretical model. *Phys. Rev. B* **41**, 8843 (1990).

86. Geohegan, D. B. & Puretzky, A. A. Dynamics of laser ablation plume penetration through low pressure background gases. *Appl. Phys. Lett.* **67**, 197 (1995).

87. Gordillo-Vázquez, F. J., Perea, A., McKiernan, A. P. & Afonso, C. N. Electronic temperature and density of the plasma produced by nanosecond ultraviolet laser ablation of LiF. *Appl. Phys. Lett.* **86**, 181501 (2005).

88. Fähler, S., Störmer, M. & Krebs, H. U. Origin and avoidance of droplets during laser ablation of metals. *Appl. Surf. Sci.* **109/110**, 433 (1997).

89. Jenniches, H. *et al.* Structure and magnetism of pulsed-laser-deposited ultrathin films of Fe on Cu(100). *Phys. Rev. B - Condens. Matter Mater. Phys.* **59**, 1196 (1999).

90. Gorbunov, A. A. *et al.* Ultrathin film deposition by pulsed laser ablation using crossed beams. *Appl. Surf. Sci.* **96–98**, 649 (1996).

91. Riet, E. V. D., Nillesen, C. J. C. M. & Dieleman, J. Reduction of droplet emission and target roughening in laser ablation and deposition of metals. *J. Appl. Phys.* **74**, 2008 (1993).

92. Haverkamp, J. *et al.* Plasma plume characteristics and properties of pulsed laser deposited diamond-like carbon films. *J. Appl. Phys.* **93**, 3627 (2003).

93. Geohegan, D. B. *Pulsed Laser Deposition of Thin Films*. (Wiley Interscience, 1994).

94. Harilal, S. S., Bindhu, C. V., Tillack, M. S., Najmabadi, F. & Gaeris, A. C. Internal structure and expansion dynamics of laser ablation plumes into ambient gases. *J. Appl. Phys.* **93**, 2380 (2003).

95. Chang, J. J. & Warner, B. E. Laser-plasma interaction during visible-laser ablation of methods. *Appl. Phys. Lett.* **69**, 473 (1996).

96. Krebs, H. *et al.* Pulsed Laser Deposition (PLD) - a versatile thin film technique. in *Advances in Solid State Physics* (ed. Kramer, B.) pages 505-518 (Spinger, Berlin, Heidelberg, 2003).

97. Barnesa, J. P., Petford-Long, A. K., Suárez-García, A. & Serna, R. Evidence for shallow implantation during the growth of bismuth nanocrystals by pulsed laser deposition. *J. Appl. Phys.* **93**, 6396 (2003).

98. Fähler, S., Sturm, K. & Krebs, H. U. Resputtering during the growth of pulsed-laser-deposited metallic films in vacuum and in an ambient gas. *Appl. Phys. Lett.* **75**, 3766 (1999).

99. Amoruso, S. Plume characterization in pulsed laser deposition of metal oxide thin films. in *Metal Oxide-Based Thin Film Structures* (eds. Pryds, N. & Esposito, V.) pages 133-160 (Elsevier, 2018).

100. Muller, D. A., Nakagawa, N. & Ohtomo, A. Atomic-scale imaging of nanoengineered oxygen vacancy profiles in SrTiO3. *Nature* **430**, 657 (2004).

101. Wang, L. *et al.* Oxygen vacancy induced room-temperature metal-insulator transition in nickelate films and its potential application in photovoltaics. *Appl. Mater. Interfaces* **8**, 9769 (2016).

102. Davila, Y., Petitmangin, A., Hebert, C., Perrire, J. & Seiler, W. Oxygen deficiency in oxide films grown by PLD. *Appl. Surf. Sci.* **257**, 5354 (2011).

103. Saenger, K. L. *Pulsed Laser Deposition of Thin Films*. (Wiley, 1994).

104. Foote, M. C. *et al.* Composition variations in pulsed-laser-deposited Y-Ba-Cu-O thin films as a function of deposition parameters. *Phys. C* **201**, 176 (1992).

105. Kan, D. & Shimakawa, Y. Controlled cation stoichiometry in pulsed laser deposition-grown BaTiO3 epitaxial thin films with laser fluence. *Appl. Phys. Lett.* **99**, 081907 (2011).

106. Oyabu, N., Custance, Ó., Yi, I., Sugawara, Y. & Morita, S. Mechanical vertical manipulation of selected single atoms by soft nanoindentation using near contact atomic force microscopy. *Phys. Rev. Lett.* **90**, 176102 (2003).

107. Meyer, E., Hug, H. J. & Bennewitz, R. *Scanning Probe Microscopy: The Lab on a Tip*. (Spinger, 2004).

108. Grob, J. J. & Siffert, P. Rutherford Backscattering Spectroscopy (RBS). *Prog. Cryst. Growth Charact.* **8**, 59 (1984).

109. Lukasch, B. Correction of the limited energy resolution in RBS spectra. *Phys. Status Solidi* **64**, 533 (1981).

110. Chu, W.-K., Mayer, J. W. & Nicolet, M.-A. *Backscattering Spectrometry*. (Academic Press, INC. (London) LTD., 1978).

111. Beckhoff, B., Kanngießer, B., Langhoff, N., Wedell, R. & Wolff, H. *Handbook of Practical X-ray Fluorescence Analysis*. (Springer-Verlag Berlin Heidelberg, 2006).

112. Pecharsky, V. K. & Zavalij, P. Y. *Fundamentals of Powder Diffraction and Structural Characterization of Materials*. (Springer, 2003).

113. Fagaly, R. L. Superconducting quantum interference device instruments and applications. *Rev. Sci. Instrum.* **77**, 101101 (2006).

114. Clarke, J. & Braginski, A. I. *The SQUID Handbook. Vol I Fundamentals and Technology of SQUIDs and SQUID Systems*. (Wiley-VCH, 2004).

115. Hamilton, W. O. Superconducting shielding. *Rev. Phys. Appl.* **5**, 41 (1970).

116. Freiser, M. J. A survey of magnetooptic effects. *IEEE Trans. Magn.* **MAG-4**, 152 (1968).

117. Zak, J., Moog, E. R., Liu, C. & Bader, S. D. Magneto-optics of multilayers with arbitrary magnetization directions. *Phys. Rev. B* **43**, 6423 (1991).

118. Sepúlveda, B., Huttel, Y., Martínez Boubeta, C., Cebollada, A. & Armelles, G. Linear and quadratic magneto-optical Kerr effects in continuous and granular ultrathin monocrystalline Fe films. *Phys. Rev. B* **68**, 064401 (2003).

119. Kahn, F. J., Pershan, P. S. & Remeika, J. P. Ultraviolet magneto-optical properties of single-crystal orthoferrites, garnets, and other ferric oxide compounds. *Phys. Rev.* **186**, 891 (1969).

120. Wittekoek, S., Popma, T. J. A., Robertson, J. M. & Bongers, P. F. Magneto-optic spectra and the dielectric tensor elements of bismuth-substituted iron garnets at photon energies between 2.2-5.2 eV. *Phys. Rev. B* **12**, 2777 (1975).

121. Larsen, P. K. & Metselaar, R. Defects and the electronic properties of Y3Fe5O12. *J. Solid State Chem.* **12**, 253 (1975).

122. Moskvin, A. S., Zenkov, A. V., Yuryeva, E. I. & Gubanov, V. A. Origin of the magneto-optical properties of iron garnets. *Phys. B* **168**, 187 (1991).

123. Scott, G. B. The Optical Absorption and Magneto-Optic spectra of Y3Fe5O12. in *Physics of Magnetic Garnets* (ed. Paoletti, A.) pages 445-459 (North-Holland Publishing Company, 1978).

124. Polder, D. VIII. On the theory of ferromagnetic resonance. *London, Edinburgh, Dublin Philos. Mag. J. Sci.* **40**, 99 (1949).

125. Kalarickal, S. S. *et al.* Ferromagnetic resonance linewidth in metallic thin films: Comparison of measurement methods. *J. Appl. Phys.* **99**, 093909 (2006).

126. Hickey, M. C. & Moodera, J. S. Origin of intrinsic Gilbert damping. *Phys. Rev. Lett.* **102**, 137601 (2009).

127. Ciubotariu, O., Semisalova, A., Lenz, K. & Albrecht, M. Strain-induced perpendicular magnetic anisotropy and Gilbert damping of Tm3Fe5O12 thin films. *Sci. Rep.* **9**, 17474 (2019).

128. Gomez-San Roman, R., Perez Casero, R., Marechal, C., Enard, J. P. & Perriere, J. 18O isotopic tracer studies of the laser ablation of Bi2Sr2Ca1Cu2O8. *J. Appl. Phys.* **80**, 1787 (1996).

129. Mayer, M. No Title. *SIMNRA User's Guid.* Report IPP 9/113 (1997).

130. Lutsev, L. V. *et al.* Low-relaxation spin waves in laser-molecular-beam epitaxy grown nanosized yttrium iron garnet films. *Appl. Phys. Lett.* **108**, (2016).

131. Khartsev, S. I. & Grishin, A. M. High performance [Bi3Fe5O12/Sm3Ga5O12]m magneto-optical photonic crystals. *J. Appl. Phys.* **101**, 3906 (2007).

132. Manuilov, S. A., Fors, R., Khartsev, S. I. & Grishin, A. M. Submicron Y3Fe5O12 film magnetostatic wave band pass filters. *J. Appl. Phys.* **105**, 033917 (2009).

133. Hoefer, C. S., Kirby, K. W. & DeShazer, L. G. Thermo-optic properties of gadolinium garnet laser crystals. *J. Opt. Soc. Am. B* **5**, 2327 (1988).

134. Diamant, R. *et al.* The evolution of inner-shell multielectronic X-ray spectra from threshold to saturation for low- to high-Z atoms. *Radiat. Phys. Chem.* **75**, 1434 (2006).

135. Illig, A. J., Chantler, C. T. & Payne, A. T. Voigt profile characterization of copper Kα. *J. Phys. B At. Mol. Opt. Phys.* **46**, 235001 (2013).

136. Chang, H. *et al.* Nanometer-thick yttrium iron garnet films with extremely low damping. *IEEE Magn. Lett.* **5**, 6700104 (2014).

137. Jakubisova, E. L., Visnovsky, S., Chang, H. & Wu, M. Interface effects in nanometer-thick yttrium iron garnet films studied by magneto-optical spectroscopy. *Appl. Phys. Lett.* **108**, 082403 (2016).

138. Jakubisova-Liskova, E., Visnovsky, S., Chang, H. & Wu, M. Optical spectroscopy of sputtered nanometer-thick yttrium iron garnet films. *J. Appl. Phys.* **117**, 17B702 (2015).

139. Hauser, C. *et al.* Annealing of amorphous yttrium iron garnet thin films in argon atmosphere. *J. Appl. Phys.* **122**, 083908 (2017).

140. Manuilov, S. A. & Grishin, A. M. Pulsed laser deposited Y$_{3}$Fe$_{5}$O$_{12}$ films: Nature of magnetic anisotropy I. *J. Appl. Phys.* **106**, 123917 (2010).

141. Hansen, P., Röschmann, P. & Tolksdorf, W. Saturation magnetization of gallium-substituted yttrium iron garnet. *J. Appl. Phys.* **45**, 2728 (1974).

142. Geller, S., Espinosa, G. P. & Crandall, P. B. Thermal expansion of yttrium and gadolinium iron, gallium and aluminum garnets. *J. Appl. Crystallogr.* **2**, 86 (1969).

143. Sokolov, N. S. *et al.* Thin yttrium iron garnet films grown by pulsed laser deposition: Crystal structure, static, and dynamic magnetic properties. *J. Appl. Phys.* **119**, 023903 (2016).

144. Wu, C. N. *et al.* High-quality single-crystal thulium iron garnet films with perpendicular magnetic anisotropy by off-axis sputtering. *AIP Adv.* **8**, 055904 (2018).

145. Mruczkiewicz, M. *et al.* Spin-wave nonreciprocity and magnonic band structure in a thin permalloy film induced by dynamical coupling with an array of Ni stripes. *Phys. Rev. B* **96**, 104411 (2017).

146. Stanciu, C. D. *et al.* All-optical magnetic recording with circularly polarized light. *Phys. Rev. Lett.* **99**, 047601 (2007).

## Acknowledgements

Over the last years several people contributed through scientific or moral support to the progress of this work. I am grateful to

*my family*. Vã mulţumesc Mamã şi Tatã pentru grija pe care mereu mi-aţi purtat-o, fie cã am fost acasã sau la sute de kilometri distanţã. Vã mulţumesc cã aţi sacrificat bucuria de a avea copilul în preajmã şi cã m-aţi îndrumat spre ce aţi considerat voi cã m-ar ajuta sã am o viaţã fericitã.

*Professor Albrecht*. Thank you very much that after a skype interview five years ago you welcomed me in your group. My practical experience, objective analysis, and personal development, they all flourished in your group.

*Experimental Physics IV*. I thank all my colleagues for the help with the bureaucratic work, introductions to all devices, technical support often needed in the labs, kindness and fun.

*our collaborators*. I am thankful for the access to the equipment, the discussions and the measurements sometimes needed in short times.

*Manu*. You have shown me the greatest support, patience and care I could have asked for. I thank you for the scientific discussions, but most for your presence along my way.

I am also thankful to the Bavarian Research Foundation for financially supporting this work (grant nr. DOK-177-15).